Helium Ion Beam Irradiation of MoS_2: Fabrication of 2D Memristors

A thesis presented to the University of Dublin, Trinity College

for the degree of

Doctor of Philosophy in Chemistry

by

Darragh Keane B. A. (Hons.)

Under the supervision of Prof. John J. Boland and Prof. Hongzhou Zhang

2020

Trinity College Dublin

Declaration

I, the undersigned, declare that this work has not previously been submitted as an exercise for a degree at this, or any other University, and that unless otherwise stated is my own work. Elements of this work that have been carried out jointly with others or by collaborators have been duly acknowledged in the text. I agree to deposit this thesis in the University's open access institutional repository or allow the library to do so on my behalf, subject to Irish Copyright Legislation and Trinity College Library conditions of use and acknowledgement.

Darragh Keane

Date

Summary

A memristor is an electronic device which exhibits a non-volatile and reversible resistance change in response to an applied electric field. These properties make the memristor a potential prime component in the field of non-volatile resistive memory (RRAM) as well as in bioinspired neuromorphic computing systems. 2D layered materials such as molybdenum disulfide (MoS_2) offer some distinct advantages over traditional metal oxide-based RRAM components such as enhanced electrostatic control of the 2D channel, mechanical flexibility and optical transparency. Memristive phenomena have recently been observed in monolayer MoS_2 devices. Using CVD grown polycrystalline MoS_2 flakes, these devices showed resistive switching mediated by the presence of grain boundaries which formed naturally during the growth process. This device design, however, is limited by the density, location and orientation of these grain boundaries which cannot be reliable controlled, limiting their down-scaling and compatibility with CMOS fabrication techniques.

Chapter 5 demonstrates a novel method of fabricating memristors from single crystal, monolayer MoS_2 by irradiation with a finely focused helium ion probe (< 3 nm). It is known that a He^+ beam can modify the electrical characteristics of MoS_2 through the introduction of defects and tune the stoichiometry due to the preferential sputtering of sulfur, with unprecedented spatial resolution. Site-specific irradiation in the helium ion microscope (HIM) creates a population of sulfur vacancies in the MoS_2 lattice which act as mobile dopants and migrate under an applied electric field, modulating the resistance. The irradiated region is characterised using transmission electron microscopy (TEM) and atomic force microscopy (AFM). Electrical characterisation of the devices show stable, repeatable bipolar switching between high and low resistance states for hundreds of cycles and with retention time of > 12 h. Raman and PL spectroscopic mapping is used to track the distribution of these defects as the device is switched between resistance states. Furthermore, owing to the 2D nature of these devices, the current levels, set voltage and on/off ratio can be further tuned by the application of a back-gate which is not

possible for higher dimensional memristive systems. Neuromorphic functionalities of the devices such as pulsed potentiation and depression and heterosynaptic plasticity are also demonstrated.

A further goal of this research is to understand the evolution of conductivity of MoS_2 under accumulating localised helium ion irradiation. Chapter 6 describes the results of electrical characterisation of MoS_2 devices performed in-situ in the HIM chamber. A single pixel wide line irradiation (probe size < 5 nm) delivers an ion dose of $0.1\ \mathrm{pC\ \mu m^{-1}}$ to $4\ \mathrm{pC\ \mu m^{-1}}$ in 14 discrete steps with two drain-source voltage sweeps performed after each step. The ion irradiation introduces defects to the material which act as charge traps. The density of traps increases approximately linearly with delivered dose before saturating above $2.5\ \mathrm{pC\ \mu m^{-1}}$. At low ion doses the output curve exhibits a 'transient' hysteresis, that is only present in the positive region of the first I-V sweep after irradiation and is not present in the second sweep.

Acknowledgements

I would like to first and foremost thank my co-supervisors Professor John Boland and Professor Hongzhou Zhang. Thank you both for your patience and guidance over these past years and for giving me the opportunity to pursue my PhD.

I would also like to thank the members of the Boland and Zhang groups, both past and present, Hugh, Shaun, Fabio, Chiara, Michelle, Jessamyn, Allen, Abbas, Yangbo, Reagan, Danny, and Pierce. Your help and input to my project is much appreciated. I would especially like to show my appreciation to Jakub. Many late evenings were spent in the lab concocting hair-brained experiments, or just pulling our hair out at the failed ones. Your friendship and support have been invaluable to me and I know your destined for a great research career. I would also like to thank Clive Dowling, Eoin McCarthy, Dermot Daly and the rest of the staff at the AML for your help with equipment and your tireless troubleshooting. Thanks to Mel for your proofing and advice. And a thanks too to Mary and Rachel for your guidance with all things administrative, you made it a breeze.

To the office lads, Owen, Lorcan, Will, Emmet and Felim. Where would I be without the camaraderie, the pints, the laughs, the moans, the rants. You allowed me not to take it all so seriously, and to blow off steam when the time needed. I couldn't think of a better group to have gone through this with.

To Isy. I don't know how you put up with me over the last few years, but your patience and understanding and love I will never forget and will always be thankful for. You are truly wonderful.

Finally, I would like to thank my parents, John and Jane, for their unending support over the last few years and indeed my entire life. Without you I would have never gotten to where I am today, and your constant encouragement has meant so much to me.

Table of Contents

List of Figures

List of Tables

List of Abbreviations

2D	Two-dimensional
AC	Alternating contact
AFM	Atomic force microscope
ALD	Atomic layer deposition
BID	Beam induced deposition
BSE	Backscattered electron
CAD	Computer aided design
CC	Current compliance
CCD	Charge-coupled device
CF	Conductive filament
CVD	Chemical vapour deposition
DRAM	Dynamic random-access memory
EBL	Electron beam lithography
ECM	Electrochemical metallisation
EDX	Energy dispersive X-ray diffraction
ET	Everhart-Thornley
FEG	Field emission gun
FeRAM	Ferroelectric random-access memory
FET	Field effect transistor
FFT	Fast Fourier transform
FIB	Focussed ion beam
FOM	Figure of merit
FWHM	Full width at half maximum
GFIS	Gas field ion source
GO	Graphene Oxide
h-BN	Hexagonal boron nitride
HAADF	High angular annular dark field

HIM	Helium Ion Microscope
HRS	High resistance state
HSQ	Hydrogen silsesquioxane
IC	Integrated circuit
IPA	Isopropyl alcohol
IR	Infrared
LMIS	Liquid metal ion source
LRS	Low resistance state
LTD	Long-term depression
LTP	Long-term potentiation
MIBK	Methyl isobutyl ketone
MIM	Metal-insulator-metal
NVM	Non-volatile memory
OM	Optical microscope
PCM	Phase change memories
PD	Photodetector
PL	Photoluminescence
PMMA	Polymethyl-methacrylate
PMT	Photomultiplier tube
RRAM	Resistive random-access memory
RS	Resistive switching
SAD	Select area diffraction
SCLC	Space charge limited current
SE	Secondary electron
SEM	Scanning electron microscope
SFIM	Scanning field ion microscopy
SMU	Source-measurement unit
SPM	Scanning probe microscope
SRAM	Static random-access memory
SS	Subthreshold swing

STEM	Scanning transmission electron microscope
STM	Scanning tunnelling microscope
TEM	Transmission electron microscope
TFL	Trap-filled limit
TMDC	Transition metal dichalcogenide
TTL	Through the lens
VCM	Valence change memory
VRH	Variable range hopping

Publications

MoS_2 Memtransistors Fabricated by Localized Helium Ion Beam Irradiation

Jakub Jadwiszczak*, **Darragh Keane***, Pierce Maguire, Conor P. Cullen, Yangbo Zhou, Hua-Ding Song, Clive Downing, Daniel S. Fox, Niall McEvoy, Rui Zhu, Jun Xu, Georg S. Duesberg, Zhi-Min Liao, John J. Boland, and Hongzhou Zhang

ACS Nano 13.12, **2019**, 14262-14273

Defect-Moderated Oxidative Etching of MoS_2

Pierce Maguire, Jakub Jadwiszczak, Maria O'Brien, **Darragh Keane**, Georg S. Duesberg, Niall McEvoy, and Hongzhou Zhang

Journal of Applied Physics 126.16, **2019**, 164301

Suppression of the shear Raman mode in defective bilayer MoS_2

Pierce Maguire, Clive Downing, Jakub Jadwiszczak, Maria O'Brien, **Darragh Keane**, John B. McManus, Georg S. Duesberg, Valeria Nicolosi, Niall McEvoy, and Hongzhou Zhang.

Journal of Applied Physics, 125 (6), **2019**, 064305

Oxide-mediated recovery of field-effect mobility in plasma-treated MoS_2

Jakub Jadwiszczak, Colin O'Callaghan, Yangbo Zhou, Daniel S. Fox, Eamonn Weitz, **Darragh Keane**, Conor P. Cullen, Ian O'Reilly, Clive Downing, Aleksey Shmeliov, Pierce Maguire, John J Gough, Cormac McGuinness, Mauro S Ferreira, A Louise Bradley, John J Boland, Georg S Duesberg, Valeria Nicolosi, and Hongzhou Zhang

Science Advances, 4 (3), **2018**, eaao5031

Programmable graphene doping via electron beam irradiation

Yangbo Zhou, Jakub Jadwiszczak, **Darragh Keane**, Ying Chen, Dapeng Yu, and Hongzhou Zhang.

Nanoscale, 9 (25), **2017**, 8657-8664

Presentations

Oral Presentations

HeFIB 2018

Dresden, Germany

Jun 11th – Jun 13th 2018

Helium Ion Beam: Fabrication of Gate-Tunable Memristor

PicoFIB: Advances in Gas-Ion Microscopy

Dresden, Germany

Jan 31st – Feb 1st 2018

Helium Ion Beam: Fabrication of Gate-Tunable Memristor

Poster Presentations

Nanoweek

University of Limerick

Oct 21st – Oct 22nd 2015

Site-specific modification of MoS_2: Towards memristive defect networks

We are living in a material world
and I am a material girl

-Madonna

Chapter 1

Introduction

The materials we use have shaped our civilisation since the dawn of mankind. We regard materials as so important that entire periods of human history are defined by the predominant material of the day, such as the Stone Age, Bronze Age, and Iron Age. More recently, the explosive advances in digital electronics and the transformational impact computers have had on our society means that the last half century could well be defined as the Silicon Age. One of the most recent breakthroughs in material science has been in the field of nanoscience.

Nanoscience broadly encompasses materials, and their related technologies, with at least one dimension below 100 nm. Although nanomaterials are associated with modern science, they have a history of use by artisans as far back as the 4th century. One example is the *Lycurgus Cup*, a piece of Roman glassware which incorporates colloidal gold and silver nanoparticle impurities, giving it unique fluorescent properties when lit from the inside.[1] The modern idea of exploiting materials on the very small scale was popularised by Richard Feynman in a 1959 lecture he gave titled 'There's plenty of room at the bottom'.[2] In this talk he envisioned manipulating materials by 'manoeuvring things atom by atom' and put forward the plausibility of writing all 24 volumes of *Encyclopaedia Britannica* on the head of a pin. In the following decades the field of nanoscience grew with the synthesis and utilisation of nanomaterials such as fullerenes[3], quantum dots[4], nanowires[5], and carbon nanotubes[6]. The isolation of graphene from graphite by Andre Geim and Konstantin Novoselov in 2004 propelled two dimensional (2D) materials to the forefront of material science research, and resulted in them winning the Nobel Prize in Physics in 2010.[7]

Graphene is a one-atom-thick, crystalline carbon film and represents the ultimate limit in scaling for material thickness. The strong in-plane covalent bonds and atomic thickness enable excellent mechanical strength, flexibility and transparency. The confinement of

electrons in two dimensions facilitates compelling electronic properties such as graphene's ultrahigh room-temperature conductivity.[8] This discovery was soon followed by an entire class of layered crystals which could be isolated to monolayers comprising of a diverse array of crystal structures, stoichiometries and resultant properties.[9] The Transition metal dichalcogenide (TMDC) molybdenum disulfide (MoS_2) is one such material. Unlike graphene, MoS_2 is a semiconductor, possessing an electronic bandgap, making it ideal for use as the channel material of high-performance electronic/optoelectronic devices.[8] The ability to control the channel thickness at the atomic level translates into reduced short-channel effects, which are one of the main issues in ultra-scaled silicon based devices.[10] One of the most intriguing applications of 2D materials is their use in memristors.

A memristor is a device with a simple structure; two electrodes contacting a 'storage' layer which can be dynamically reconfigured when stimulated by electrical inputs. The reconfiguration in a memristor is typically driven by internal defect redistribution under the electric field. Much like the *Lycurgus Cup,* a small number of nanoscale defects results in behaviour unachievable in the 'pristine' form. The material reconfiguration of the storage layer results in a change in the device resistance which can be used to store data and also directly process data, hence the term memristor (memory + resistor). The simple structure of a memristor allows for high density integration and low cost fabrication[11] with fundamental studies showing device scaling to sub-10 nm feature sizes[12] and memory retention for years.[13] In particular, 2D materials have excellent electrical properties, perfect interface states, and atomic-scale thickness, making them a promising candidate for memristor materials. Furthermore, 2D materials exhibit high flexibility and transparency, which offers great potential in the field of wearable electronics.

Memristors have come to the attention of the semiconductor industry as a potential technology for the 'post-Silicon Age'. Conventional computing systems are based on architecture proposed by John von Neumann which use physically separated units for processing and storing data.[14] Data and algorithms are stored in memory and must be transferred to the processing unit to be executed, after which they are pushed back to memory. Moore's law of scaling have exponentially increased the speed, and decrease

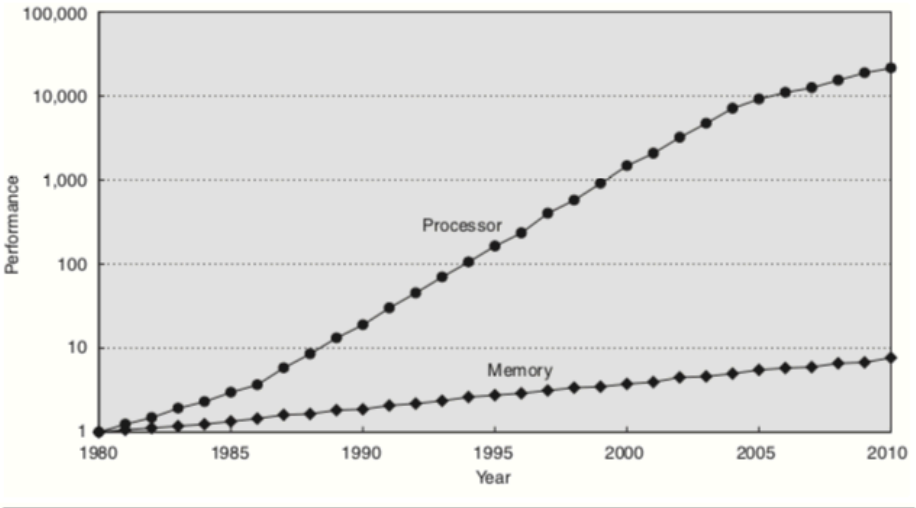

Figure 1.1 | Gap in performance between processor speeds and memory access speeds over time. Normalised to 1980 baseline.[15]

the cost and dimension of transistors which make up the processors. However, memory technology has not kept pace (see Figure 1.1).[15] The latency (and energy cost) introduced by shuttling data between the memory units limits the throughput of computational operations and is known as the von Neumann bottleneck. This has resulted in a regime where further transistor scaling projected by Moore's law may no longer result in proportionate increases in overall computational efficiency.[16] These limitations become particularly acute for data centric task, such as the real-time image processing for self-driving cars. In the most straightforward approach, memristors offer a solution as an ultrahigh-density memory layer that can be directly integrated on the processor chip, thus significantly reducing the bottleneck and improving the speed and energy efficiency of the system. Another approach is to increase the density of information available for storage and processing without increasing the amount of materials and chip area being utilised, referred to as 'scaling-in'. Controlling the gradual resistance change of a memristor means binary states (ON and OFF) give way to a range of intermediate resistance states that can encode more than 1 bit.[11]

Memristors may play a larger role in computer systems beyond memory and storage. An alternative computer architecture was proposed by one of von Neumann's contemporaries, Alan Turing. In a paper written in 1948, but which remained unpublished until well after his death, titled 'Intelligent Machinery', Turing envisioned a machine

consisting of artificial neurons (i.e. simple processing units) that are connected together by modifiers.[17] These neuromorphic systems take inspiration from the biological brain to perform computation and learning. The human brain is capable of solving complex problems in real time while occupying a compact volume and only consuming power on the order of 20 W.[18] Around the same time Turing wrote Intelligent Machinery, Donald Hebb proposed synaptic plasticity as a mechanism for memory and learning.[19] Hebbian learning can be summed up in the phrase 'neurons that fire together, wire together'. Artificial neural networks have shown superior performance in processing cognitive and data-intensive tasks in recent years, even surpassing human abilities in specific complex tasks such as playing the game Go.[20] Up until now, neural network implementations have been mainly based on conventional computing hardware and thus their performance is still fundamentally limited by the von Neumann bottleneck. In contrast, a memristor based implementation could simultaneously store the synaptic weight (as its resistance) and modulate the transmitted signal in a single device. The natural co-location of memory and compute in the same memristor device eliminates the constant data movement and can thus significantly improve the system efficiency.[11]

Hand in hand with new materials, new tools are required to forge, shape, cut and modify them. Nanomaterials require a distinct set of apparatus to fully exploit their potential. The recently commercially available helium ion microscope (HIM) is one such tool. The use of a focused beam of ions to modify materials on the nanoscale was actually also proposed by Feynman in his *Plenty of Room* talk.[2] He says 'A source of ions, sent through the microscope lenses in reverse, could be focused to a very small spot. We could write with that spot like we write in a TV cathode ray oscilloscope'. The probe of the HIM can be confined to a sub-nanometre size[21], a very small spot indeed. Given the superlative confinement of 2D materials in the out-of-plane direction, it is possible to restrict the beam-sample interaction to an exceptionally small region. By 'writing' with this probe onto a 2D material, defects can be introduced to the crystal structure with unprecedented control and precision.

The goal of this thesis is to utilise a focussed helium ion beam to modify 2D materials on the nanoscale. Specifically, the research questions are; is it possible to engineer defects into an otherwise pristine material system (MoS_2) to induce memristive behaviour? By

taking control of an otherwise stochastic process (grain boundaries emerging from growth process), can scaling and manufacturing roadblocks be overcome? Can we analyse the behaviour of those defects under an applied electric field and understand how it relates to the modulation of the device resistance? Can we quantify the performance of these devices as memory elements? Can neuromorphic functionalities of these beam-enabled devices be demonstrated? Further understanding of how the electronic behaviour changes under localised helium ion irradiation is also needed. By using space charge limited conduction theory can the introduction of trap states explain electronic behaviour as irradiation induced defects accumulate?

1.1 Thesis Outline

This chapter has served as a motivation for this work and introduces the concepts which will be explored in more depth in subsequent chapters. **Chapter 2** will describe the background and theory of resistive switching and memristor devices as well as the material properties of MoS_2. It will then cover the synthesis of these two areas with a review of the current literature on MoS_2-based memristors, highlighting the current challenges faced. **Chapter 3** will describe the operation of the helium ion microscope, the key enabling technology of this work. Particular attention is paid to modification and defect engineering of MoS_2. **Chapter 4** will describe the working principles behind the other types of equipment and methods used for fabrication and analysis throughout this work. **Chapter 5** will demonstrate the fabrication of a single crystal, monolayer, MoS_2 memristor device enabled by local irradiation of the channel with a focussed helium ion beam. Electrical characterisation of the modified device reveals stable bipolar resistive switching, in which the current levels, on/off ratio and set voltage are gate-tuneable. Spectroscopic evidence that the field-driven drift of sulfur vacancies, sourced from the irradiated region, serves to realise the different resistance states. **Chapter 6** investigates the evolution of the conductivity of MoS_2 devices in-situ as an accumulating dose of helium ions is delivered to the centre of the channel. Defects introduced by the beam act as charge traps and the emergence of I-V hysteresis is tracked as the damage accumulates. Finally, in **chapter 7** the main conclusions and outlook of this work will be summarised.

1.2 References

1. https://www.nano.gov/timeline. Accessed: 12/05/19
2. Feynman, R. P. Plenty of Room at the Bottom. in *APS annual meeting* (1959).
3. Kroto, H. W., Heath, J. R., O'Brien, S. C., Curl, R. F. & Smalley, R. E. C60: Buckminsterfullerene. *Nature* **318**, 162 (1985).
4. Reed, M. A. *et al.* Spatial quantization in GaAs–AlGaAs multiple quantum dots. *Journal of Vacuum Science & Technology B: Microelectronics Processing and Phenomena* **4**, 358–360 (1986).
5. Kuno, M. An overview of solution-based semiconductor nanowires: synthesis and optical studies. *Physical Chemistry Chemical Physics* **10**, 620–639 (2008).
6. Liu, J. *et al.* Fullerene pipes. *Science* **280**, 1253–1256 (1998).
7. Novoselov, K.S., Geim, A.K., Morozov, S.V., Jiang, D.A., Zhang, Y., Dubonos, S.V., Grigorieva, I.V. and Firsov, A. A. Electric field effect in atomically thin carbon films. *Science* **306**, 666–669 (2004).
8. Tan, C. *et al.* Recent Advances in Ultrathin Two-Dimensional Nanomaterials. *Chemical Reviews* acs.chemrev.6b00558 (2017) . doi:10.1021/acs.chemrev.6b00558
9. Novoselov, K. S. *et al.* Two-dimensional atomic crystals. *Proceedings of the National Academy of Sciences* **102**, 10451–10453 (2005).
10. Fiori, G. *et al.* Electronics based on two-dimensional materials. *Nature Nanotechnology* **9**, (2014).
11. Zidan, M. A., Strachan, J. P. & Lu, W. D. The future of electronics based on memristive systems. *Nature Electronics* **1**, 22–29 (2018).
12. Govoreanu, B. *et al.* 10× 10nm 2 Hf/HfO x crossbar resistive RAM with excellent performance, reliability and low-energy operation. in *2011 International Electron Devices Meeting* 31–36 (IEEE, 2011).
13. Yang, J. J., Strukov, D. B. & Stewart, D. R. Memristive devices for computing. *Nature Nanotechnology* **8**, 13–24 (2013).
14. Von Neumann, J. First Draft of a Report on the EDVAC. *IEEE Annals of the History of Computing* 27–75 (1993).
15. Hennessy, J. L. & Patterson, D. A. *Computer architecture: a quantitative*

approach. (Elsevier, 2011).

16. Rajendran, B. & Alibart, F. Neuromorphic Computing Based on Emerging Memory Technologies. *IEEE Journal on Emerging and Selected Topics in Circuits and Systems* **6**, 198–211 (2016).
17. Copeland, B. J. & Proudfoot, D. Alan Turing's forgotten ideas in computer science. *Scientific American* **280**, 98–103 (1999).
18. Kim, S. G., Han, J. S., Kim, H., Kim, S. Y. & Jang, H. W. Recent Advances in Memristive Materials for Artificial Synapses. *Advanced Materials Technologies* **1800457**, 1800457 (2018).
19. Cooper, S. J. Donald O. Hebb's synapse and learning rule: a history and commentary. *Neuroscience & Biobehavioral Reviews* **28**, 851–874 (2005).
20. Silver, D. *et al.* Mastering the game of Go with deep neural networks and tree search. *Nature* **529**, 484 (2016).
21. Ward, B. W., Notte, J. A. & Economou, N. P. Helium ion microscope: A new tool for nanoscale microscopy and metrology. *Journal of Vacuum Science & Technology B: Microelectronics and Nanometer Structures* **24**, 2871 (2006).

Chapter 2

Background Theory

This chapter will serve as an introduction to memristors, with a particular focus on the material systems and mechanisms of 2D memristors. Methods of evaluating the performance these devices are outlined. A synopsis of the current state of the art of 2D MoS_2 memristors is given. MoS_2 as a material is discussed more generally.

2.1 Resistive Switching Memory

Non-volatile memory (NVM) refers to a type of memory device that has the capability to hold saved data even if the power is turned off. The ultimate NVM should display characteristics such as high-density and low cost, fast write and read access, low energy operation and high endurance and retention.[1] The current state of the art is realised in Si-based Flash memory which can achieve high density with low fabrication costs as a result of decades of research in the semiconductor industry.[2] However, Flash suffers from low endurance, low write speeds and high voltages required for write operations. This makes Flash suitable for storage-memory, which is accessed infrequently, but not for working memory. Mainstream working memory implementations utilise static random access memory (SRAM) for the CPU cache and dynamic random access memory (DRAM) for the computer's main memory. These demonstrate much shorter read and write times and much larger endurance, but are volatile memories, i.e. data is not retained when the power is switched off. For a comparison of these technologies see table 2.1. In any case, these Si based implementations may soon reach the end of their scaling with further increases in density expected to run in to physical limits in the near future.[1] Alternatives to Si-based memory have been explored such as Ferroelectric random access memory (FeRAM)[3] and spin-transfer-torque magnetic RAM[4]. One of the 'most promising' class of emerging memory devices as deemed by the International Roadmap for Devices and Systems (IRDS)[5] are based on resistive switching (RS) and are generally referred to as resistive

random access memory (RRAM). RS-based NVMs have already been brought to market by companies such as Panasonic, with applications in controlling sensors.[6] Other RS applications, such as the use of RS cells as electronic synapses in artificial neural networks and neuromorphic computing remain at an earlier stage, but their potential is greater, as they represent a completely new computing architecture with multiple applications (not only information storage).[7]

RRAM elements change their resistance value in response to an applied electrical stimulus. Typically, they operate by switching between a high resistance state (HRS) and low resistance state (LRS). The structure of a resistive switching memory cell is generally built as a metal-insulator-metal (MIM) configuration, which comprises of a highly resistive insulating material 'I' with two, possible different, highly conductive metal electrodes 'M', in a sandwich or planar structure.

Starting with reports by *Hickmott* in 1962, a huge variety of MIM structures have been reported to exhibit resistive switching.[8,9] Typically the 'I' material can be a wide variety of binary oxides or chalcogenides which show some ion conductivity. The 'M' material can similarly be a wide variety of active or inert metals including electron conducting non-metals.[9]

Table 2.1 | Comparison of memory and storage technologies.[10]

	RRAM	SRAM	DRAM	FLASH
Reciprocal density (F^2)	< 4	140	6-12	1 - 4
Energy per bit	10^{-13} J	5×10^{-16} J	5×10^{-16} J	2×10^{-17} J
Read time	< 10 ns	0.1 - 0.3 ns	10 ns	10 ms
Write time	~ 10 ns	0.1 - 0.3 ns	10 ns	10 ms
Retention	years	<< second	<< second	years
Endurance	10^{12} cycles	10^{16} cycles	10^{16} cycles	10^{4} cycles

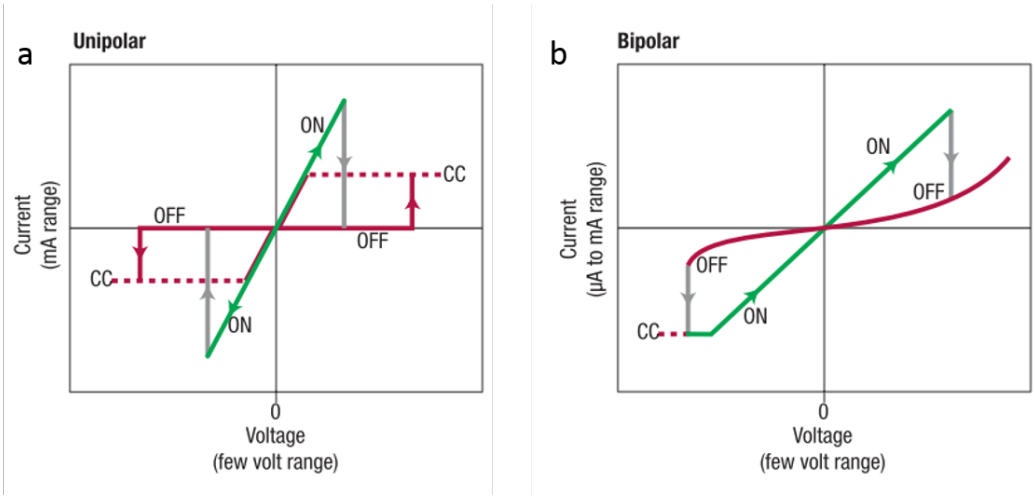

Figure 2.1 | (a) Unipolar resistive switching. The device is set in either positive or negative polarity and reset when the current in the same polarity is sufficient to trigger a break of the conductive filament. (b) Bipolar resistive switching. The device is set into the LRS in one polarity and reset when a voltage of the opposite polarity is applied. CC indicates a compliance current.[9]

First, it is useful to distinguish the two basic operating schemes for resistive switching, namely, unipolar and bipolar switching. Switching is unipolar when the switching procedure does not depend on the polarity of the applied voltage signal. A system in its high-resistance state (OFF) is switched ('set') by a threshold voltage into the low resistance state (ON), as shown in Figure 2.1a. The current is limited by a compliance current of a control circuit. The 'reset' into the OFF state takes place at a higher current and a voltage below the set voltage. In contrast, bipolar switching occurs when the set to the ON state occurs at one voltage polarity and reset to the OFF state on the reverse voltage polarity (shown in Figure 2.1b). The structure of the system must have some asymmetry in order to exhibit bipolar switching.[9]

Resistive switching memories can also be described as so called memristors. This framework, first outlined by Leon Chua[11], is particularly useful when multi-level resistance values or even analogue values are to be stored or processed. There is some inconsistency in the literature regarding naming convention, as the link between the decades-long body of work on resistive switching memories and memristors was not made until 2008 when pointed out by Stanley Williams and collegues.[12] Often 'resistive switching' was reserved for switching between binary states while 'memristor' was used for multi-level or analogue systems. However, 'memristor' has become the term du jour

even in the case where only binary switching is demonstrated. It is almost ubiquitous when describing resistive switching of 2D materials. In this sense binary resistive switching memories can be thought of as a sub-category of memristors. Indeed in later work Chua would classify any two-terminal device which exhibits an electrical 'pinched hysteresis loop', regardless of material system or physical operating mechanism as a memristor.[13,14] Thus, the term 'memristor' is used throughout this thesis.

2.2 Theoretical description of memristors.

Memristors or 'memory resistors' are two terminal devices which have an internal state of resistance that is dependent on the history of applied voltage or current. Crucially, this resistance state is retained once the power is switched off. Memristors were first proposed by Leon Chua in 1971 as the fourth fundamental passive circuit element, joining the resistor, capacitor and inductor.[11] Each of these elements can be described by a relationship between two of the four fundamental circuit quantities: current (i), voltage (v), charge (q), and flux (φ) (see Figure 2.2a). Current and voltage are the time derivatives of charge and flux respectively, thus those quantities are fundamentally linked. Resistance (voltage to current), capacitance (charge to voltage) and inductance (flux to current) link three of the remaining four pairs of quantities.

Chua's argument was based on symmetry, that there should exist a device which provides a functional relation between the remaining pair of quantities (flux to charge), namely the memristor with memristance (M), given by:

$$M(q) = \frac{d\varphi}{dq} \qquad \textbf{2 - 1}$$

Using the definition of voltage as the time (t) derivative of flux we can recover a form of Ohm's law, except now the resistance is replaced by the variable memristance which depends on the entire past history of applied current (the time derivative of charge).[15]

$$v = \frac{d\varphi}{dt} = \frac{d\varphi(q)}{dq}\frac{dq}{dt} = M(q(t))i \qquad \textbf{2 - 2}$$

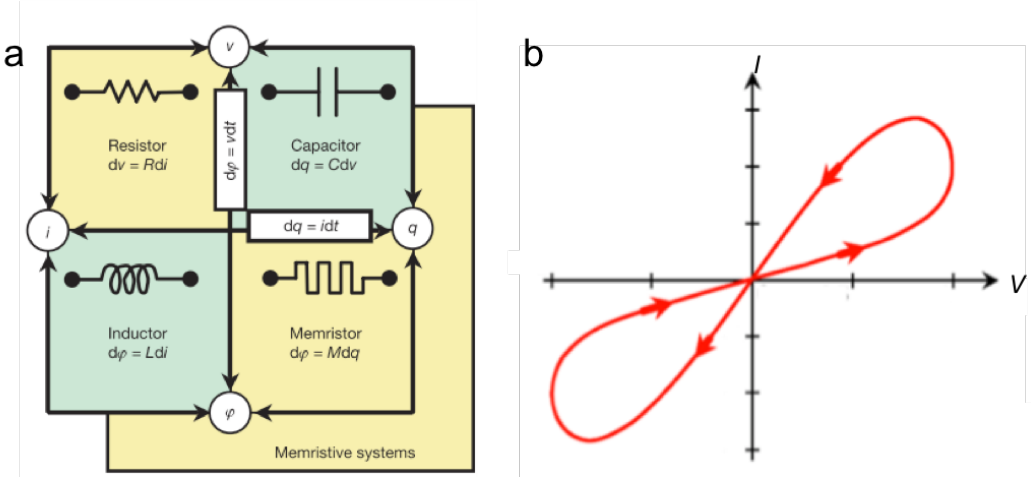

Figure 2.2 | (a) The 4 fundamental, two-terminal, circuit elements and the relationships between them.[12] (b) Current-Voltage hysteresis loop which is pinched at the origin.[13]

These memristor devices exhibit a distinctive 'fingerprint' characterised by a hysteresis loop confined to the first and third quadrant of the I-V domain pinched at $0\,V$, shown schematically in Figure 2.2b. This hysteretic current-voltage response cannot be replicated by any combination of the other passive circuit elements. Unlike the capacitor and inductor it does not store any charge and no current flows through the device if the voltage drop across it is zero. The resistance is modulated as voltage is applied, however when the bias is turned off the resistance should remain fixed. Thus, the memristor exhibits non-volatile memory, storing information as its resistance state. In the idealised memristor these resistance levels fall on a continuum so an arbitrary number of memory levels can be achieved in a single device.[16]

2.3 Memristive materials and switching mechanisms.

The memristor concept was not explicitly link to experimental evidence until 2008 when Stanley Williams and colleagues demonstrated that a stacked metal/oxide/metal device exhibited the characteristic hysteretic behaviour.[12] The critical 3 nm oxide film contained one layer of insulating TiO_2 and one layer of a lower resistance oxygen deficient TiO_{2-x} sandwiched between two Pt electrodes (see Figure 2.3). The oxygen vacancies act as mobile +2 charged dopants ($V_O^{\bullet\bullet}$ in Kröger-Vink notation[17]) which drift under an applied voltage bias. This shifts the boundary between the stochiometric and non-stochiometric

sub-layers, causing a change in the device resistance. Using a simple linear ionic drift model, they showed that the memristive response of the device was inversely proportional to the square of the film thickness (D):

$$M(q) \propto \frac{1}{D^2} \qquad \textbf{2 - 3}$$

This term is 1,000,000 times larger in absolute value on the nanometre scale than it is on the micrometre scale. Thus memristance is functionally a nanoscale phenomenon.

The TiO_2 thin film system described above is part of a broader class of devices which are known as *valence change memory* (VCM) devices. These VCM devices are based on the drift of anions or their vacancies under an applied electric field. VCM is observed in other transition metal oxides (such as AlO_x, Ta_2O_x, ZnO_x, HfO_x), nitrides (AlN), and chalcogenides (ZnTe, ZnSe).[10] A general feature of these VCM materials is that they are highly resistive in the native state and that the anion, or equivalently its positively charged vacancy ($V_O^{\bullet\bullet}$ in the case of TiO_2) is much more mobile than the cation. As in the above case, a reservoir of vacancies can be intentionally introduced during the fabrication process. Alternatively, a population of these vacancies can be generated by an electrochemical self-doping process, where an oxidation reaction can occur at the anode interface, according to

$$O_O \leftrightarrow V_O^{\bullet\bullet} + 2e^- + \frac{1}{2}O_2 \qquad \textbf{2 - 4}$$

where O_O represents an oxygen ion on a regular site.[9]

During an electroforming step the oxygen vacancies drift towards the cathode and accumulate forming a 'virtual cathode' which grows back towards the anode and can eventually form a conductive filament (CF). Bipolar switching takes place through local redox reactions between the virtual cathode and the anode by forming and breaking the conductive contact. These vacancy rich CFs have been directly observed by TEM and are shown in Figure 2.4a. This straightforward switching model is complicated by lateral diffusion of $V_O^{\bullet\bullet}$ into the non-CF region. As the non-CF region constitutes a parallel resistance to the CF this typically results in adverse effects, such as increased leakage

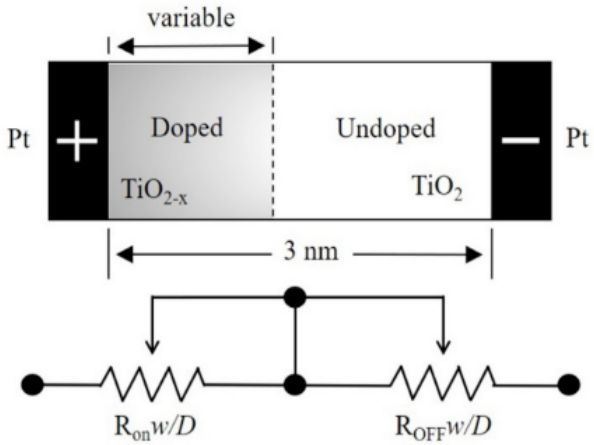

Figure 2.3 | The $Pt/TiO_{2-x}/TiO_2/Pt$ memristor (top) and its equivalent circuit (bottom). The device resistance can be modulated by applying a voltage bias which shifts the boundary between the two layers.[78]

current and eventual failure of the device. An appropriate electrode can alternatively act as a sink of vacancies. Park et. al.[18] demonstrated a Ta_2O_5 based VCM RRAM cell with Ta (source) and RuO_x (sink) electrodes. By carefully balancing the $V_O^{\bullet\bullet}$ supplying and $V_O^{\bullet\bullet}$ sinking capabilities of

the respective electrodes great improvements in endurance and stability could be achieved. In addition to altering the conductivity of the channel, charge injection at the contact is affected by the dopant concentration at the interface. Metal/semiconductor contacts are Schottky-like in the case of low doping and ohmic in the highly doped case. Thus, vacancy accumulation at the interface can cause dynamic Schottky barrier lowering which contributes to the observed resistive switching.[19]

Several of these metal oxide systems exhibit atypical co-existence of bipolar and unipolar resistive switching. Examples include TiO_x, ZrO_x, MoO_x, AlO_x and HfO_2.[20] The current range is the crucial factor which determines the switching regime. At low current, bipolar switching is observed, mediated by the mechanisms described above. At high current, Joule heating may cause the rupturing of the CF, which can be reformed by the application of a voltage of the same polarity, resulting in unipolar switching. A compliance current (CC) is typically used to control which switching regime is accessed.

Another class of memristors rely on an *electrochemical metallisation* (ECM) mechanism. These devices are comprised of a solid electrolyte (which can be a large number of oxides,

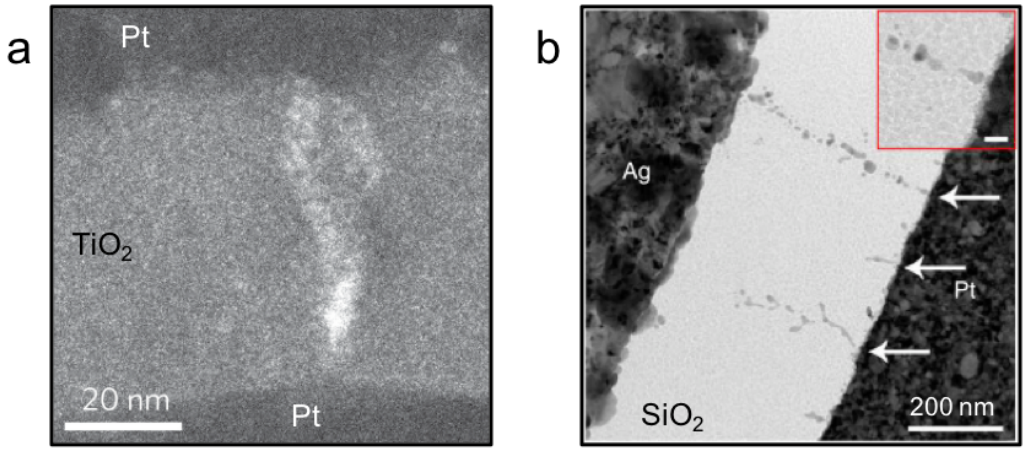

Figure 2.4 | (a) Dark-field TEM image of an oxygen deficient Magnéli filament in a TiO_2 based VCM memristor.[79] (b) Bright-field TEM image of Ag filaments in an Ag/SiO_2/Pt ECM memristor. Inset: magnified image of filament (indicated by upper arrow) near the inert electrode Scale bar, 20 nm. [80]

chalcogenides or halides) contacted with two metal electrodes. One electrode is comprised of an electrochemically active metal (such as Ag or Cu) while the other by an inert metal (such as Au, Pt). In these systems, metal atoms of the active anode are oxidised and dissolved into the solid electrolyte layer. These metal cations migrate in the ionic conductor towards the inert cathode and are reduced there. The reduced metal atoms form a highly conductive metal filament which grows towards the anode to turn on the switch (see Figure 2.4b). Changing the polarity of the bias voltage causes metal atoms at the edge of the metal filament to dissolve, rupturing the filament, and thus bipolar switching is achieved.[9] Yet another class of memristors as known as *phase change memories* (PCM), in which thermal processes control a phase transition in the switching material from the amorphous to crystalline state.[9] These typically exhibit unipolar switching.

These previous sections have outlined the basic operating modes and switching mechanisms and brief history of memristors. The following section will describe methods of evaluating the performance and the key challenges faced by memristors.

2.4 Evaluating the performance of memristor devices.

In order to evaluate the usefulness of a memristive devices for functional non-volatile memory (NVM), logic or neuromorphic applications a number of figures of merit (FOMs) such as endurance, retention time, switching time, power consumption, variability and scalability must be determined.[6]

Endurance is defined as the number of times a device can be switched between its resistance states while keeping its current on/off ratio high enough so the states can be distinguished. An endurance test requires cycling the device through a large number of set/reset cycles and the common FOM is a plot of resistance in HRS and LRS vs. cycle number. As the failure of the device may not occur in one cycle but rather be progressive, a threshold on/off ratio may need to be chosen below which the device is considered to have failed. Current commercial SRAM and DRAM must have an endurance of $>10^{16}$ cycles while Flash or magnetic hard disk storage must have $\sim10^{4}$ cycles.[10] Tantalum oxide based memristors have the best reported endurances up to 10^{12} cycles.

Retention time is a measure of the stability of the LRS and HRS over time after the set and reset transitions respectively. For each state after the device is switched a low read voltage can be applied. The FOM is a plot of current vs. time, also indicating the read voltage used. The desired data retention time for NVM technologies is 10 years.[21] Obviously testing retention time over 10 years is not easily achievable (this PhD. has felt long enough already), generally much shorter times hours or days are reported. There have been some reports which measured retention for a few hours and projected the trend for 10 years.[22] One potential method to overcome this limitation is to increase the temperature of the device while attaining the current time curve.

Switching time is measure of the time taken to transition between the resistance states. A series of set/reset pulses with increasing frequency can be applied to the device. As the on/off ratio may be dependent on the pulse width, a threshold on/off ratio below which the device is no longer deemed sufficiently switched may need to be chosen. A FOM is a plot of current of HRS and LRS vs. pulse width, and the shortest pulse width in which the states are distinguishable can be considered the switching time. Commercial DRAM has a switching time on the order of 10 ns while Flash based memory is on the order of 1 ms.[10] An all 2D graphene/MoS_{2-x} O_x/graphene stacked memristor device has achieved

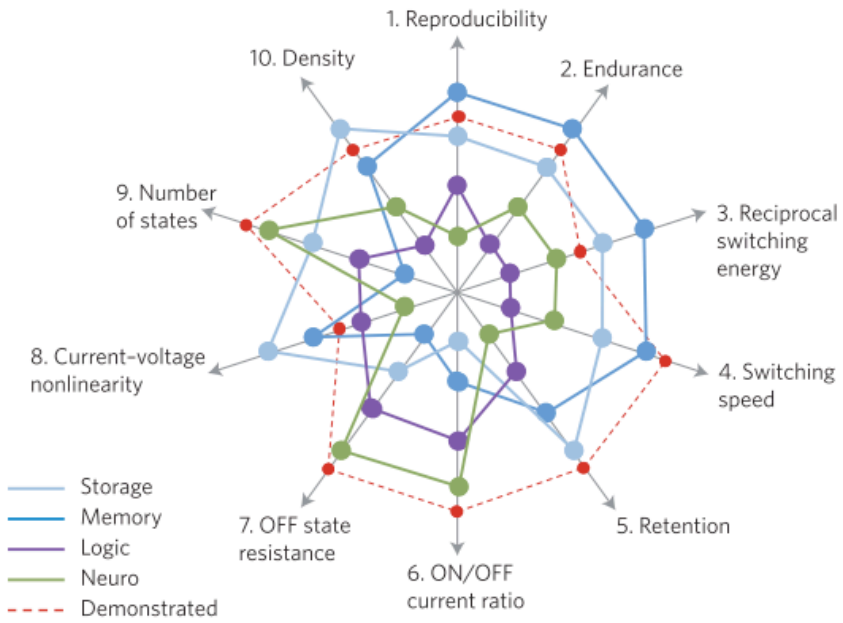

Figure 2.5 | Device performance requirements for different applications ranked. Position on axis further from the centre indicates a higher required value for that metric. The dashed red line indicates the best reported memristor experimental data (as of 2013) however are not necessarily from the same device.[10]

switching times ~100 ns.[23] The energy of the switching event may be calculated by integrating the current and voltage traces of the pulse over time.

Device variability includes both spacial (cell-to-cell) and temporal (cycle-to-cycle) variation in the electrical characteristics (i.e. V_{set}, V_{reset}, I_{HRS}, I_{LRS}). Cell-to-cell variability usually arises due to the fabrication process while cycle-to-cycle variability may be intrinsic to the physics of the device. The switching process of a memristor (filament formation and rupture, say) is a stochastic process and is thus difficult to predict with precision. In the case of cycle-to-cycle variability the endurance plot also acts as FOM for understanding how the current in the HRS and LRS changes from one cycle to the next. To characterise the V_{set} and V_{reset} variability multiple I-V sweeps must be performed and can be presented on one graph. A histogram of the extracted values can then be produced. To characterise cell-to-cell variability a good method is to measure a number of devices and highlight the median characteristic. Again a histogram is useful in conveying the distribution of these parameters.

The plasticity of conductance of memristors make them well suited for physical implementation of synaptic functions in neuromorphic circuits. Biologically, the weight of a synapse is determined by the firing patterns of the pre-synaptic and post-synaptic neurons connected to it. The synapse can be either potentiated and depressed, i.e. have their connections strengthened or weakened depending on the neuron spike patterns.[24] To demonstrate this learning behaviour with a memristor, a series of voltage pulses, called training pulses, can be inputted into the device with the output current being measured. If the memristor can be habituated into a stable conductance state, without showing decay, this is known as long-term potentiation (LTP). This is the basis of long-term memory and learning in the neuronal circuit. The counterpart of this is long-term depression (LTD), where a different pattern of training pulses is applied to habituate the device out of this conductance state, to make the device 'forget' what it has previously learned.

Another synaptic function which can be emulated by memristors is 'heterosynaptic plasticity'.[25] In this case, the activity of a particular neuron leads to changes in the strength of synaptic connection between other unactivated neurons, and this is thought to contribute to associative learning.[26] By fabricating multiple electrical connections to a single memristor, heterosynaptic plasticity can be demonstrated by driving a voltage across one pair of electrodes, and measuring a change in conductivity across a second pair of electrodes.

Optimising these performance parameters has been a goal in memristor research, however a material system which excels at all the above parameters remains elusive. Fortunately, all these parameters are not equally important for all functions. The requirements for four different applications were quantitatively ranked by Yang *et. al.*[10] and are shown in Figure 2.5 along with the best demonstrated memristor performance.

Key challenges that are faced by memristor devices are scaling and CMOS fabrication compatibility. Scaling down to sub-10 nm feature size is required to achieve storage density comparable with current Flash memory technologies. Secondly, the vast efficiency gains made by the semiconductor industry in fabrication over the last number of decades has seen the price per cell fall exponentially in line with Moore's law. In order to exploit these gains, any new memristor technology should be compatible with current

on-chip fabrication techniques. Exploiting the advantages of 2D materials is one avenue being pursued in memristor research.

2.5 MoS_2 Memristors

Recent research efforts have explored the potential of 2D materials as active memristive elements. 2D materials show advantages of excellent electrical properties, high mechanical strength, high transparency, perfect interface states, and atomic-scale thickness, making them a promising candidate for RRAM applications, which require high speed, low power, high density and diversification.[27] The physical properties of 2D materials such as grain boundaries[28], and phase states[29] enable resistive switching phenomena mediated by entirely different mechanisms compared to traditional RRAM. Furthermore, 2D material-based RRAM devices exhibit high flexibility[23,30,31] allowing these devices to be integrated into human-wearable electronics. Resistive switching has been explored in diverse types of 2D materials including hexagonal boron nitride (h-BN)[32,33] and graphene oxide (GO).[31,34] This work is focussed on MoS_2 as a memristive material. The following section outlines the material properties of MoS_2. As planar MoS_2 memristors retain some of the characteristics of field effect transistors (FETs), the next section details MoS_2 FETs. Finally a review of the current literature on MoS_2 memristors and the challenges faced by the field are discussed.

2.5.1 Molybdenum Disulfide

MoS_2 belongs to a family of materials known as transition metal dichalcogenides (TMDCs). They have a general chemical formula MX_2 where M is a transition metal atom and X is a chalcogen atom (other examples include $MoSe_2$, $MoTe_2$, WS_2, WSe_2). Like graphene it is comprised of vertically stacked molecular layers with strong covalent bonds within layers and weak van der Waal interactions between layers. This allows it to form single or multi-layered nano-structures.[35]

Each crystal layer in MoS_2 is comprised of a hexagonally coordinated plane of molybdenum atoms sandwiched between two planes of sulphur atoms forming a 'trilayer' (TL) which is ~6.5 nm thick (see Figure 2.6a). The coordination of the sulphur atoms around the molybdenum atom determines the crystal's polymorph. Trigonal prismatic

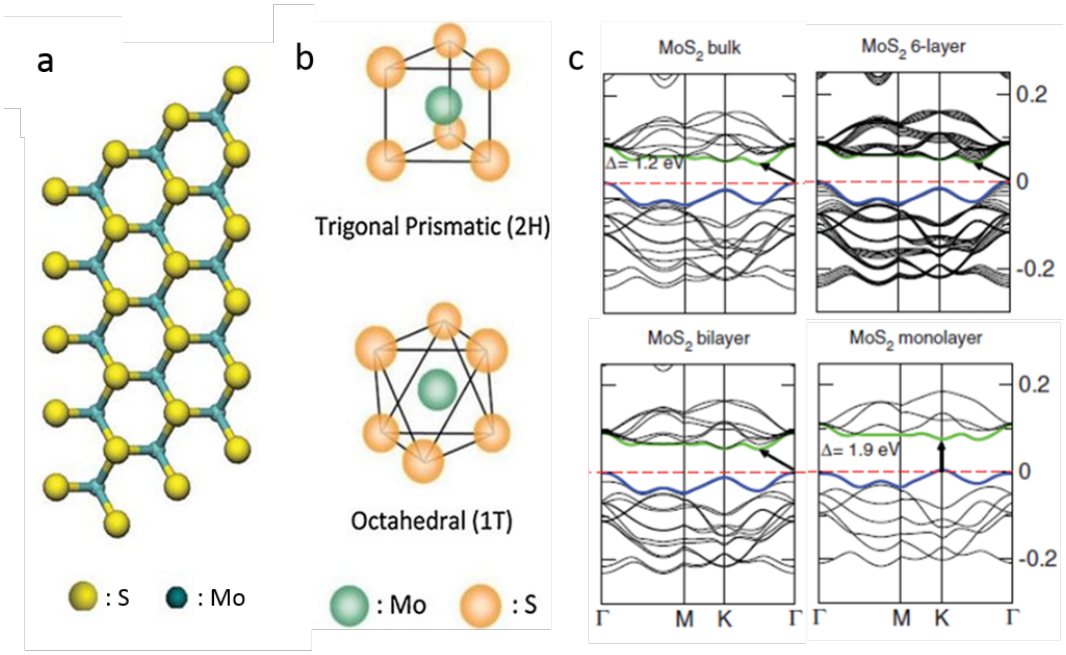

Figure 2.6 | (a) Top view of MoS_2 hexagonal lattice. (b) Trigonal prismatic (2H) and octahedral (1T) unit cells.[35] (c) Band structure of different layers of MoS_2. MoS_2 transitions from an indirect to direct gap semiconductor at the monolayer limit.[47]

coordination is called 1H-MoS2 and octahedral coordination is called 1T-MoS2 (see Figure 2.6b). The stacking of 1H layers results in two polytypes. AB stacking results in hexagonal 2H-type. ABC stacking results in rhombohedral 3R-type. 2H has a lower formation energy and thus predominates naturally occurring MoS2 crystals. Both 2H and 3R polytypes are semiconducting and show almost identical physical properties. 1T-type is metallic and has single layer stacking and can be converted from 2H by lithium ion intercalation.[36,37]

Monolayer and few layer MoS_2 can be prepared by 'top down' methods, thinning of the bulk material by micromechanical cleavage[38] or liquid exfoliation[39], or by 'bottom up' methods, chemical vapour deposition[40] (CVD) or atomic layer deposition[41] (ALD). This work utilises both mechanically exfoliated and CVD grown MoS_2.

Mechanically exfoliated MoS_2 is produced by successive thinning of the bulk material with adhesive tape and then rubbing onto a surface (such as a SiO_2 substrate). Flakes of a variety of thicknesses are then left deposited with a small fraction (<1%) of them being mono or few-layer. These can be positively identified on SiO_2 owing to their layer

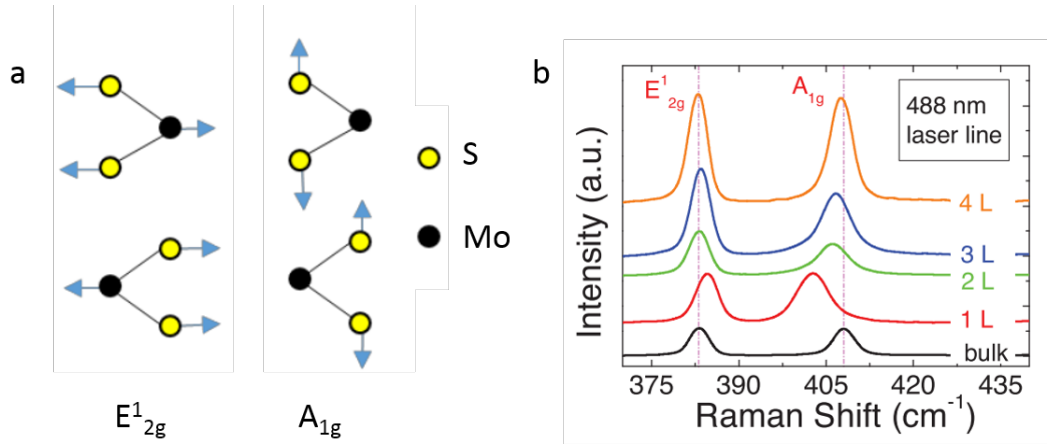

Figure 2.7 | (a) Vibrational modes associated with Raman peaks of MoS_2.[47] (b) Raman spectra for different numbers of MoS_2 layers.[49]

dependent optical contrast.[42] This relatively quick and simple method generally produces the highest quality crystals containing fewer defects. However owing to the small lateral dimension of the crystals produced, no larger than a few tens of micrometres, it is not suitable for producing material at scale. [36] A more recent method utilising a gold layer to mediated the exfoliation has produced crystals with a lateral dimension ~500 µm.[43]

CVD growth can proceed by a variety of methods such as the reaction of Mo and S precursors in the gaseous phase[44], MoO_3 precursor with gaseous S[40], and close proximity MoO_3 seed films with S gas onto a target substrate.[45] This process allows films of MoS_2 with lateral dimensions on the centimetre scale.[46]

Raman spectroscopy has been used extensively to characterise MoS_2.[47–49] For monolayer MoS_2 the Raman active optical modes are: the $E^{'}$ peak at ~385 cm^{-1} which arises from the in-plane motion of the Mo and S atoms with respect to one another and the $A^{'}_1$ peak at ~405 cm^{-1} which arises from the out of plane motion of the S atoms. Owing to a reduction in symmetry, for bulk and few layer MoS_2 these peaks or relabelled as the E^1_{2g} and A_{1g} peaks respectively. These vibrational modes are shown schematically in Figure 2.7a. There do exist other vibrational modes at lower energies which are Raman active, however these are less commonly used for characterisation. Peak separation is used for distinguishing layer number, as can be seen in Figure 2.7b. As the layer number is increased from monolayer there is red shifting of the $E^{'}/E^1_{2g}$ peak (385 cm^{-1} to 382 cm^{-1}) and blue shifting of the $A^{'}_1/A_{1g}$ peak (404 cm^{-1} to 407 cm^{-1}).

Unlike graphene, which is a zero bandgap semimetal, MoS_2 is a semiconductor. Bulk MoS_2 has an indirect bandgap of 1.2 eV while single layer MoS_2 possesses a direct bandgap of ~1.9 eV (see Figure 2.6c).[50] This leads to the emergence of strong photoluminescence (PL) in the monolayer case.[51] PL spectroscopy is useful in characterising the structure of MoS_2, as the spectrum shows the emergence of defect associated exciton peaks.[52] The presence of a bandgap means that MoS_2 can be used as the channel material in field effect transistors (FETs). FETs are the fundamental building blocks of electronic circuits, and so, paired with MoS_2 memristors, this means there is great potential for future all-2D circuit architectures. Indeed, as previously mentioned, Sangwan *et. al.*[25] demonstrated that the FET and memristor functionality can be combined into a *single* MoS_2 circuit element, termed *memtransistors*, further expanding the space of possible circuit architectures and capabilities. More concretely, the FET behaviour of the device can be used to probe physical properties (such as carrier concentration and mobility) allowing us to better understand the physics of the memristive states and switching mechanism.

2.5.2 MoS_2 Field Effect Transistors

FETs are three terminal devices comprising of a source, drain, and gate electrode, shown schematically in Figure 2.8a. The source and drain are electrically coupled to the semiconducting channel material and current can flow between them through the channel. The gate electrode is coupled via a dielectric material which allows no current flow but a field to be applied perpendicular to the channel. The operation of the device is determined by two voltages, one between the gate and source V_g, and the other between the source and drain, V_{ds}. These act as the inputs to the device, and the current flow from the drain electrode I_d acts as the output. The FET output must be able to be switched between an OFF state to an ON state, over an I_d range of several orders of magnitude, in order to represent the binary 1 and 0 from which logic operations are built.

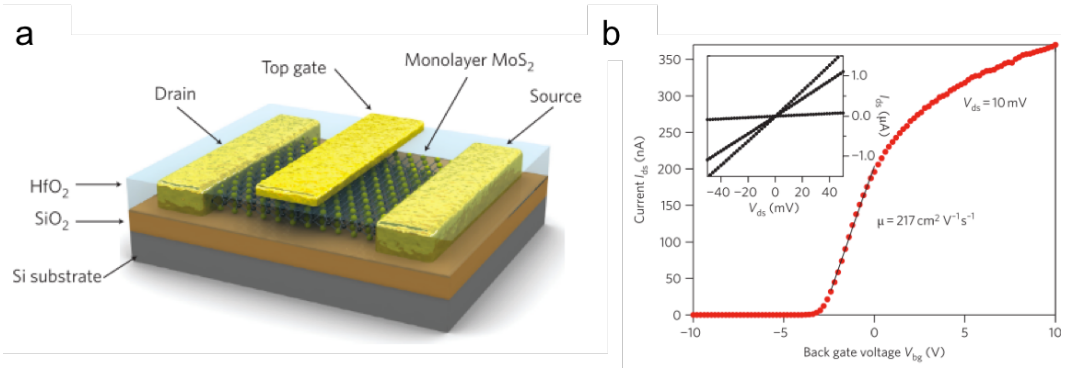

Figure 2.8 | (a) Schematic of top-gated MoS_2 FET device. (b) Transfer curve for device. Back-gate voltage V_{bg} is applied through the substrate. Inset: $I_{ds} - V_{ds}$ curves for V_{bg} values of 0, 1 and 5 V.[81]

The conductivity of the channel (σ) and thus I_d depends on the carrier concentration in the channel (n_{2D}) and the mobility of those carriers (μ):

$$\sigma = \mu\, e\, n_{2D} \qquad \textbf{2 - 5}$$

where e is the electron charge. Ideal coupling of the gate to the channel through the dielectric allows the carrier concentration (electrons in the case of MoS_2) to be controlled by the applied gate voltage V_g.

The charge in the 2D channel is given by the gate capacitance $C_b = \varepsilon/t$, where ε is the gate dielectric constant and t the thickness, multiplied by the 'excess' voltage:

$$qn_{2D} = C(V_g - V_T) \qquad \textbf{2 - 6}$$

where q is the charge and V_T is the threshold voltage. This holds true when the FET is in the ON state, $(V_g - V_T) \gg V_{th}$ (the thermal voltage $V_{th} = kT/q$). The transfer curve of an FET plots I_d vs. V_g (see Figure 2.7b). Below the threshold voltage I_d increases exponentially with V_g. One important metric is the subthreshold swing (SS), which is the gate voltage required to increase the drain current by a factor of ten. The SS is given by:

$$SS = \left(1 + \frac{C_s}{C_b}\right)\frac{kT}{q} ln10 \qquad \textbf{2 - 7}$$

where C_s is the semiconductor capacitance.

The SS indicates the switching speed of the FET. The minimum SS of a conventional device can be found by letting $C_s \rightarrow 0$, and at 300K this yields 60 mV dec^{-1}. As V_g increases further it becomes energetically difficult to inject carriers into the channel and

the drain current scales linearly with gate voltage (the ON state).[53] The on/off ratio is the ratio of the drain current in the saturation region to the drain current in the off state. A high on/off ratio is important for energy efficient, low power switching.

The mobility can also be extracted from the transfer curve of an FET (known as the field effect mobility) and is valid under two assumptions that (a) the transverse gate field is much greater than the source drain field ($V_g >> V_{ds}$) and (b) that mobility is carrier density independent.

Mobility is given by the Shockley equation:

$$\mu = \frac{L}{WC_bV_{sd}}\left(\frac{\partial I_d}{\partial V_g}\right) \qquad \textbf{2 - 8}$$

where L and W are the length and width of the channel respectively. Thus plotting I_d vs. V_g and extracting the slope from the linear region (ON state) allows one to calculate the mobility, as can be seen in Figure 2.7b. The mobility limits the achievable saturation current (output) of the device ultimately limiting its efficiency.[54]

Traditionally channel materials used for FETs have been bulk Si or III-V semiconductors, GaAs and GaN, in planar geometry. In order to improve performance channel widths have been scaled down to nanoscale dimensions, following Moore's law which predicts that the density of transistors in a chip will double every two years.[53,55] However, as channels shrink devices exhibit non-negligible off-state currents which increases power consumption as well producing heat which must be dissipated, ultimately limiting the channel length. These short channel effects have been somewhat mitigated by using high dielectric constant (high k) materials to allow more efficient electrostatic coupling of the gate electrode to the channel.[56] 3D gate geometries have also been explored, however they lead to much higher fabrication costs.[57] 2D semiconductors represent the ultimate scaling limit for channel thickness. The carriers are naturally confined to an atomically thin channels thus leading to excellent coupling with the gate electrode and thus better immunity from short channel effects. 2D materials are also compatible with current on chip fabrication processes of the semiconductor industry, making them ideal candidates for use in future high performance electronics.[58]

Deviation from the described ideal behaviour may occur due to the presence of contact resistance which limits I_d. Ideally a metal-semiconductor barrier height is the difference

between the metal work function and the semiconductor electron affinity and is described by the Schottky-Mott rule, and so the barrier height can be reduced by choosing an appropriate contact material. However due to the presence of interface states, the semiconductor bands are bent at the contact causing Fermi level pinning.[59] This Fermi level pinning means the effective barrier height at the contact is only weakly dependent on the metal work function. The pinning effect is larger in atomically thin channels due to the greater density of interface states.[60] This deviation from the Schottky-Mott rule is accounted for by a pinning factor, which ranges from 1 (ideal) to 0 (high level of pinning). The theoretical and measured values of the monolayer MoS_2 pinning factor are 0.3 and 0.11 respectively.[59] Much research has gone into engineering the contacts of MoS_2 FETs in order to improve performance. Approaches such as Fermi level depinning by introducing a interlayer between the metal and semiconductor[61], hybridisation of the metal and semiconductor orbitals using annealed Mo contacts[62], phase engineering by converting semiconducting 2H MoS2 polytype to the metallic 1T polytype at the contacts[63] or utilising edge contacts, rather than top, which allow more efficient in-plane carrier injection.[64]

2.5.3 MoS_2 Memristors

Layered transition metal dichalcogenides (TMDCs) such as MoS_2 have emerged as attractive 2D materials for high-performance nanoelectronics devices. In comparison with insulating h-BN and semi-metallic graphene, TMDCs are semiconducting with tuneable bandgap. Along with a bandgap, TMDCs display advantages such as high mobility and air stability.[65] Recently memristive switching has been observed in a series of electronic devices derived from TMDCs. For example Bessonov *et al.* demonstrated memristive devices made from solution processed MoO_x/MoS_2 heterostructures vertically sandwiched between Ag electrodes.[66] These memristors exhibited low set voltages in the range 0.1 V – 0.2 V with abrupt switching. Additionally, these solution processed devices are compatible with inkjet printing fabrication and displayed mechanical stability over 10^4 bending cycles. Cheng *et al.* demonstrated memristors based on 1T phase MoS_2 nanosheets, again in a vertically stacked $Ag/MoS_2/Ag$ structure.[29,67] When two of these devices were connected serially the IV hysteresis the

exhibited odd-symmetric pinched loop which is the 'fingerprint' of an ideal memristor. Vu *et al.* demonstrated memristive switching in a floating gate device.[68] They used CVD grown MoS_2 and graphene as a channel and trap layers respectively, separated by an Al_2O_3 tunnelling barrier. These devices exhibited stable 6-level memory. In addition they could withstand straining up to 1% when fabricated on a flexible PET substrate. M. Wang *et al.* demonstrated fully 2D memristors comprised of a graphene/$MoS_{2-x}O_x$/graphene vertical stack.[23] These memristors also exhibited good endurance against mechanically bending as well as high thermal stability up to 340ºC. Shin *et al.* demonstrated memristors from stacked layers of GO/MoS_2/GO fabricated by the spin-coating of chemically exfoliated 2D materials.[22] These devices exhibited multilevel memory as well as charge storage capabilities. W. Wang *et. al.* demonstrated photo-resistive switching in MoS_2 nanosphere thin films, which exhibited multiple sets resistance states accessible by electrically stressing either in darkness or under white light.[69]

Memristive switching of a vertical stack device with a monolayer TMDC active layer (MoS_2, $MoSe_2$, WS_2, or WSe_2) between two inert Au electrodes has been demonstrated by Ge *et al.*[70,71] These devices represent the extreme in the reduction of interelectrode distance. However, the devices show both unipolar and bipolar switching with no control over switching polarity. The authors make use of a polymer-free transfer technique to exclude any contribution of contaminates to the switching and conclude that a VCM mechanism where sulfur vacancies move to form conductive channels is likely responsible for the switching. The devices can act as zero-static power radio-frequency switch up to frequencies of 50 GHz.

Xu *et. al.* reported a similar vertical memristor but with an active Cu top electrode and inert Au bottom electrode.[72] Cu ions diffuse through the MoS_2 layer to form conductive filaments. This ECM mechanism and low interelectrode distance results in low switching voltages (~0.1 V). They found bilayer MoS_2 enabled repeated switching while monolayer devices were easily shorted, most likely through grain boundaries or defects. However, even for the bilayer devices they only demonstrated switching for ~25 cycles. The ease of diffusion of the Cu ions (which has a lower migration barrier and diffusion activation energy in MoS_2 than sulfur vacancies[73–75]), may cause degradation of the device over longer timescales.

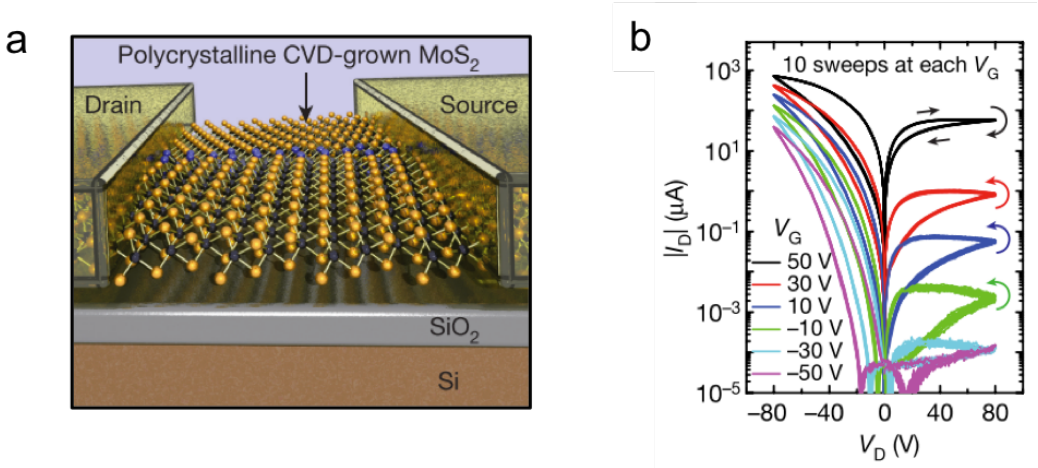

Figure 2.9 | (a) Schematic of memtransistor fabricated from polycrystalline monolayer MoS_2. The grain boundaries in the channel act as a source of mobile defects. (b) Gate tuneable IV hysteresis loops of the memtransistor devices. The resistive switching is modulated by the application of a back-gate.[25]

Lateral 2D memristor devices were first reported by Sangwan *et al.*[76] These devices are structured as back-gated field effect transistors (FETs) with CVD grown monolayer MoS_2 channels which, importantly, contained a grain boundary. The structure is shown schematically in Figure 2.9a. A novel feature of these devices is that they are gate-tunable. This allows the carrier density to be controlled by an independent third electrode, as can be seen in Figure 2.9b. In follow-up work these polycrystalline MoS_2 devices have been termed 'memtransistors', as they combine the functionality of memristors and transistors in a single device.[25] Switching of resistance states in these memtransistor devices is modulated by the field-driven drift of defects from the grain boundary regions. The lateral structure allows the devices to act as a window to study the motion of ions, such as sulfur vacancies, as the mechanism underlying the memristive effect. By using PL and Raman mapping, direct evidence for the migration of these vacancies can be obtained.

These defect rich grain boundaries arise during the CVD growth which is conducted in a sulfur deficient environment. However, the density, location, and orientation of these grain boundaries is random and not controllable, thus compatibility with silicon based fabrication processes is limited. The downscaling of these devices is ultimately limited by the distribution of these grain boundary regions. This is a key challenge which is addressed by this thesis in chapter 5.

Such planar memtransistor devices can act as a platform to realise multi-terminal neuromorphic circuits. Sangwan *et al.* demonstrated that their devices could emulate heterosynaptic plasticity, where the resistance between one pair of electrodes was modulated by the biasing of another pair of electrodes. Li *et al.* fabricated planar memristor devices utilising a mechanical printing method to deposit a 15 nm thick MoS_2 channel.[77] They identified two types of switching modes attributed to the modulation of the contact Schottky barriers and redistribution of ionic vacancies in the channel respectively. They demonstrated that two of these devices could be ionically coupled together emulating the ionic interactions between neurons.

In summary, memristors are a prime component for next-generation non-volatile resistive memory (RRAM) as well as bioinspired neuromorphic computing systems. 2D materials such as MoS_2 show advantages of excellent electrical properties, high mechanical strength, high transparency, perfect interface states, and atomic-scale thickness, making them a promising candidate as active memristive elements. Challenges remain such as the reliance on randomly arising grain boundaries to enable planar MoS_2 memristors which limits the potential for scaling and compatibility with CMOS fabrication techniques. The next chapter describes the helium ion microscope as tool which can be used to precisely and controllable modify the crystal structure of MoS_2.

2.6 References

1. Waser, R., Dittmann, R., Staikov, C. & Szot, K. Redox-based resistive switching memories nanoionic mechanisms, prospects, and challenges. *Advanced Materials* **21**, 2632–2663 (2009).
2. Hennessy, J. L. & Patterson, D. A. *Computer architecture: a quantitative approach*. (Elsevier, 2011).
3. Ghoneim, M. & Hussain, M. Review on Physically Flexible Nonvolatile Memory for Internet of Everything Electronics. *Electronics* **4**, 424–479 (2015).
4. Yu, S. & Chen, P.-Y. Emerging memory technologies: Recent trends and prospects. *IEEE Solid-State Circuits Magazine* **8**, 43–56 (2016).
5. International Roadmap for Devices and Systems: 2017 Beyond CMOS. *IEEE* (2017).
6. Lanza, M. *et al.* Recommended Methods to Study Resistive Switching Devices. *Advanced Electronic Materials* **1800143**, 1800143 (2018).
7. Kuzum, D., Yu, S. & Philip Wong, H. S. Synaptic electronics: Materials, devices and applications. *Nanotechnology* **24**, (2013).
8. Hickmott, T. W. Low-frequency negative resistance in thin anodic oxide films. *Journal of Applied Physics* **33**, 2669–2682 (1962).
9. Waser, R. & Aono, M. Nanoionics-based resistive switching memories. *Nature Materials* **6**, 833–840 (2007).
10. Yang, J. J., Strukov, D. B. & Stewart, D. R. Memristive devices for computing. *Nature Nanotechnology* **8**, 13–24 (2013).
11. Chua, L. O. Memristor—The Missing Circuit Element. *IEEE Transactions on Circuit Theory* **18**, 507–519 (1971).
12. Strukov, D. B., Snider, G. S., Stewart, D. R. & Williams, R. S. The missing memristor found. *Nature* **453**, 80–3 (2008).
13. Chua, L. Resistance switching memories are memristors. *Applied Physics A: Materials Science and Processing* **102**, 765–783 (2011).
14. Chua, L. If it's pinched it's a memristor. *Memristors and Memristive Systems* **9781461490**, 17–90 (2014).
15. Joglekar, Y. N. & Wolf, S. J. The elusive memristor: properties of basic electrical

circuits. *European Journal of Physics* **30**, 661 (2009).

16. The memristor revisited. *Nature Electronics* **1**, 261 (2018).
17. Kröger, F. A. & Vink, H. J. Relations between the concentrations of imperfections in crystalline solids. in *Solid State Physics* **3**, 307–435 (Elsevier, 1956).
18. Park, T. H. *et al.* Balancing the Source and Sink of Oxygen Vacancies for the Resistive Switching Memory. *ACS Applied Materials and Interfaces* **10**, 21445–21450 (2018).
19. Marchewka, A., Waser, R. & Menzel, S. Physical simulation of dynamic resistive switching in metal oxides using a Schottky contact barrier model. in *2015 International Conference on Simulation of Semiconductor Processes and Devices (SISPAD)* 297–300 (IEEE, 2015).
20. Mohammad, B. *et al.* State of the art of metal oxide memristor devices. *Nanotechnology Reviews* **5**, 311–329 (2016).
21. Hui, F. *et al.* Graphene and Related Materials for Resistive Random Access Memories. *Advanced Electronic Materials* **3**, 1–32 (2017).
22. Shin, G. H. *et al.* Multilevel resistive switching nonvolatile memory based on MoS_2 nanosheet-embedded graphene oxide. *2D Materials* **3**, 034002 (2016).
23. Wang, M. *et al.* Robust memristors based on layered two- dimensional materials. *Nature Electronics* **1**, (2018).
24. Chang, T., Yang, Y. & Lu, W. Building neuromorphic circuits with memristive devices. *IEEE Circuits and Systems Magazine* **13**, 56–73 (2013).
25. Sangwan, V. K. *et al.* Multi-terminal memtransistors from polycrystalline monolayer molybdenum disulfide. *Nature* **554**, 500–504 (2018).
26. Bailey, C. H., Giustetto, M., Huang, Y. Y., Hawkins, R. D. & Kandel, E. R. Is Heterosynaptic modulation essential for stabilizing hebbian plasiticity and memory. *Nature Reviews Neuroscience* **1**, 11–20 (2000).
27. Hou, X., Chen, H., Zhang, Z., Wang, S. & Zhou, P. 2D Atomic Crystals: A Promising Solution for Next-Generation Data Storage. *Advanced Electronic Materials* **1800944**, 1800944 (2019).
28. Sangwan, V. K., Lee, H. S. & Hersam, M. C. Gate-tunable memristors from monolayer MoS_2. *Technical Digest - International Electron Devices Meeting,*

IEDM 5.1.1-5.1.4 (2018). doi:10.1109/IEDM.2017.8268330

29. Cheng, P., Sun, K. & Hu, Y. H. Memristive Behavior and Ideal Memristor of 1T Phase MoS_2 Nanosheets. *Nano Letters* **16**, 572–576 (2016).
30. Son, D. *et al.* Colloidal synthesis of uniform-sized molybdenum disulfide nanosheets for wafer-scale flexible nonvolatile memory. *Advanced Materials* **28**, 9326–9332 (2016).
31. Jeong, H. Y. *et al.* Graphene oxide thin films for flexible nonvolatile memory applications. *Nano letters* **10**, 4381–4386 (2010).
32. Pan, C. *et al.* Coexistence of Grain-Boundaries-Assisted Bipolar and Threshold Resistive Switching in Multilayer Hexagonal Boron Nitride. *Advanced Functional Materials* **1604811**, 1604811 (2017).
33. Qian, K. *et al.* Hexagonal boron nitride thin film for flexible resistive memory applications. *Advanced Functional Materials* **26**, 2176–2184 (2016).
34. Wang, L.-H. *et al.* The mechanism of the asymmetric SET and RESET speed of graphene oxide based flexible resistive switching memories. *Applied Physics Letters* **100**, 63509 (2012).
35. Ganatra, R. & Zhang, Q. Few-layer MoS_2: A promising layered semiconductor. *ACS Nano* **8**, 4074–4099 (2014).
36. Song, I., Park, C. & Choi, H. C. Synthesis and properties of molybdenum disulphide: From bulk to atomic layers. *RSC Advances* **5**, 7495–7514 (2015).
37. Xia, J. *et al.* Phase evolution of lithium intercalation dynamics in 2H-MoS_2. *Nanoscale* **9**, 7533–7540 (2017).
38. Novoselov, K. S. *et al.* Two-dimensional atomic crystals. *Proceedings of the National Academy of Sciences* **102**, 10451–10453 (2005).
39. Nicolosi, V., Chhowalla, M., Kanatzidis, M. G., Strano, M. S. & Coleman, J. N. Liquid exfoliation of layered materials. *Science* **340**, 72–75 (2013).
40. Najmaei, S. *et al.* Vapour phase growth and grain boundary structure of molybdenum disulphide atomic layers. *Nature Mater.* **12**, 754–759 (2013).
41. Tan, L. K. *et al.* Atomic layer deposition of a MoS_2 film. *Nanoscale* **6**, 10584–10588 (2014).
42. Li, H. *et al.* Optical identification of single- and few-layer MoS_2 sheets. *Small* **8**,

682–686 (2012).

43. Desai, S. B. *et al.* Gold-Mediated Exfoliation of Ultralarge Optoelectronically-Perfect Monolayers. *Advanced Materials* **28**, 4053–4058 (2016).
44. Zhan, Y., Liu, Z., Najmaei, S., Ajayan, P. M. & Lou, J. Large-area vapor-phase growth and characterization of MoS_2 atomic layers on a SiO2 substrate. *Small* **8**, 966–971 (2012).
45. O'Brien, M. *et al.* Transition Metal Dichalcogenide Growth via Close Proximity Precursor Supply. *Scientific Reports* **4**, 7374 (2014).
46. Jeon, J. *et al.* Layer-controlled CVD growth of large-area two-dimensional MoS_2 films. *Nanoscale* **7**, 1688–1695 (2015).
47. Ye, M., Winslow, D., Zhang, D., Pandey, R. & Yap, Y. Recent Advancement on the Optical Properties of Two-Dimensional Molybdenum Disulfide (MoS_2) Thin Films. *Photonics* **2**, 288–307 (2015).
48. Parkin, W. M. *et al.* Raman Shifts in Electron-Irradiated Monolayer MoS_2. *ACS Nano* **10**, 4134–4142 (2016).
49. Li, H. *et al.* From bulk to monolayer MoS_2 : Evolution of Raman scattering. *Advanced Functional Materials* **22**, 1385–1390 (2012).
50. Mak, K. F., Lee, C., Hone, J., Shan, J. & Heinz, T. F. Atomically thin MoS_2: A new direct-gap semiconductor. *Physical Review Letters* **105**, 136805 (2010).
51. Splendiani, A. *et al.* Emerging Photoluminescence in Monolayer MoS_2. *Nano Letters* **10**, 1271–1275 (2010).
52. Tongay, S. *et al.* Defects activated photoluminescence in two-dimensional semiconductors: interplay between bound, charged and free excitons. *Scientific Reports* **3**, 2657 (2013).
53. Chhowalla, M., Jena, D. & Zhang, H. Two-dimensional semiconductors for transistors. *Nature Reviews Materials* **1**, 16052 (2016).
54. Choi, H. H., Cho, K., Frisbie, C. D., Sirringhaus, H. & Podzorov, V. Critical assessment of charge mobility extraction in FETs. *Nature Materials* **17**, 2–7 (2017).
55. Moore, G. E. Cramming more components onto integrated circuits. *Proceedings of the IEEE* **86**, 82–85 (1998).

56. Fiori, G. *et al.* Electronics based on two-dimensional materials. *Nature Nanotechnology* **9**, 768–779 (2014).
57. Jan, C. H. *et al.* A 22nm SoC platform technology featuring 3-D tri-gate and high-k/metal gate, optimized for ultra low power, high performance and high density SoC applications. *Technical Digest - International Electron Devices Meeting, IEDM* 44–47 (2012). doi:10.1109/IEDM.2012.6478969
58. Lemme, M. C., Echtermeyer, T. J., Baus, M. & Kurz, H. A graphene field-effect device. *IEEE Electron Device Letters* **28**, 282–284 (2007).
59. Liu, H. *et al.* Switching mechanism in single-layer molybdenum disulfide transistors: An insight into current flow across Schottky barriers. *ACS Nano* **8**, 1031–1038 (2014).
60. Li, S.-L., Tsukagoshi, K., Orgiu, E. & Samorì, P. Charge transport and mobility engineering in two-dimensional transition metal chalcogenide semiconductors. *Chem. Soc. Rev.* **45**, 118–151 (2016).
61. Park, W. *et al.* Contact Resistance Reduction using Fermi Level De-pinning Layer for MoS_2 FETs. *IEDM* **8**, 108–111 (2014).
62. Kang, J., Liu, W. & Banerjee, K. High-performance MoS_2 transistors with low-resistance molybdenum contacts. *Applied Physics Letters* **104**, 093106 (2014).
63. Kappera, R. *et al.* Metallic 1T phase source/drain electrodes for field effect transistors from chemical vapor deposited MoS_2. *APL Materials* **2**, (2014).
64. Guimarães, M. H. D. *et al.* Atomically Thin Ohmic Edge Contacts between Two-Dimensional Materials. *ACS Nano* **10**, 6392–6399 (2016).
65. Wang, Q. H., Kalantar-Zadeh, K., Kis, A., Coleman, J. N. & Strano, M. S. Electronics and optoelectronics of two-dimensional transition metal dichalcogenides. *Nature Nanotechnology* **7**, 699–712 (2012).
66. Bessonov, A. a *et al.* Layered memristive and memcapacitive switches for printable electronics. *Nature materials* **14**, 199–204 (2015).
67. Cheng, P., Sun, K. & Hu, Y. H. Mechanically-induced reverse phase transformation of MoS_2 from stable 2H to metastable 1T and its memristive behavior. *RSC Adv.* **6**, 65691–65697 (2016).
68. Vu, Q. A. *et al.* A High-On/Off-Ratio Floating-Gate Memristor Array on a Flexible

Substrate via CVD-Grown Large-Area 2D Layer Stacking. *Advanced Materials* **29**, 1–7 (2017).

69. Wang, W. *et al.* MoS_2 memristor with photoresistive switching. *Scientific Reports* **6**, 31224 (2016).
70. Ge, R. *et al.* Atomristor: Nonvolatile Resistance Switching in Atomic Sheets of Transition Metal Dichalcogenides. *Nano Letters* **18**, 434–441 (2018).
71. Kim, M. *et al.* Zero-static power radio-frequency switches based on MoS_2 atomristors. *Nature Communications* **9**, 2524 (2018).
72. Xu, R. *et al.* Vertical MoS_2 double layer memristor with electrochemical metallization as an atomic-scale synapse with switching thresholds approaching 100 mV. *Nano Letters* acs.nanolett.8b05140 (2019). doi:10.1021/acs.nanolett.8b05140
73. Le, D., Rawal, T. B. & Rahman, T. S. Single-layer MoS_2 with sulfur vacancies: structure and catalytic application. *The Journal of Physical Chemistry C* **118**, 5346–5351 (2014).
74. Komsa, H.-P., Kurasch, S., Lehtinen, O., Kaiser, U. & Krasheninnikov, A. V. From point to extended defects in two-dimensional MoS_2: evolution of atomic structure under electron irradiation. *Physical Review B* **88**, 35301 (2013).
75. Guzman, D. M., Onofrio, N. & Strachan, A. First principles investigation of copper and silver intercalated molybdenum disulfide. *Journal of Applied Physics* **121**, 55703 (2017).
76. Sangwan, V. K. *et al.* Gate-tunable memristive phenomena mediated by grain boundaries in single-layer MoS_2. *Nature Nanotechnology* **10**, 403–406 (2015).
77. Li, D. *et al.* MoS_2 Memristors Exhibiting Variable Switching Characteristics toward Biorealistic Synaptic Emulation. *ACS Nano* **12**, 9240–9252 (2018).
78. Li, Y., Wang, Z., Midya, R. M., Xia, Q. & Yang, J. J. Review of memristor devices in neuromorphic computing: materials sciences and device challenges. *Journal of Physics D: Applied Physics* (2018). doi:10.1088/1361-6463/aade3f
79. Kwon, D. H. *et al.* Atomic structure of conducting nanofilaments in TiO2 resistive switching memory. *Nature Nanotechnology* **5**, 148–153 (2010).
80. Yang, Y. *et al.* Observation of conducting filament growth in nanoscale resistive

memories. *Nature Communications* **3**, 732–738 (2012).

81. Radisavljevic, B., Radenovic, A., Brivio, J., Giacometti, V. & Kis, A. Single-layer MoS_2 transistors. *Nature Nanotechnology* **6**, 147–50 (2011).

Chapter 3

Ion Beam Modification

Chapter 2 introduced the concept of memristors and we saw that taking advantage of the unique properties of 2D materials can enable novel functionalities such as gate-tunable memtransistors. The modification and engineering of these materials on the nanoscale has the potential overcome some of the challenges faced by these novel devices as material properties (such as thickness, stoichiometry and conductivity) can be tailored precisely and controllably. In this chapter the modification of nanomaterials by the helium ion microscope (HIM) will be explored. The operating principles of the HIM and the advantages it offers over other charged beam microscopes are outlined. A particular focus is paid to defect engineering of MoS_2.

3.1 Ion Beams

Ion beam modification is based on the interaction of energetic ions with solids. It has widely been exploited as a means of controllably altering the electrical, physical, chemical, mechanical and optical properties of materials. A prime example is the doping of semiconductors for integrated circuit (IC) fabrication which is achieved through ion implantation and has spurred enormous technological advancement in microprocessors over the past number of decades.[1]

The Helium Ion Microscope (HIM), utilises a gas field ion source (GFIS) which can form a He^+ or Ne^+ beam with sub-nanometre resolution and is used for both imaging and modification. These beams have been demonstrated to enable material modification via direct write milling or sputtering[2], defect introduction[3], ion beam lithography[4], and gas assisted processing[5]. Engineering and modifying 2D materials with precision is essential to realising desired functionalities. 2D materials are particularly suited to ion beam modification as all their atoms are at the surface and thus equally accessible by the beam. Additionally, the nanometre spacial resolution of the HIM probe allows for precise

nanostructure engineering. Control over crystal structure, stoichiometry, thickness, doping, defect level and geometry has been demonstrated. HIM lithography has demonstrated sub 10 nm feature sizes,[6] and direct-write nanopatterning by material sputtering offers an alternative to mask- based lithography. Nanoribbons, that is laterally confined ribbons of ~10 nm, have been fabricated in graphene[7] and MoS_2[3]. Nanopores with diameters <3 nm have been fabricated in graphene.[8] Gas assisted ion etching can accelerate the rate of direct-write patterning with sub 10 nm WSe_2 nanoribbons having been demonstrated.[5] Ion beam mixing of graphene encapsulated in hexagonal boron nitride results in the n-doping of the material.[9] The introduction of sulfur vacancies to MoS_2, owing to the preferential sputtering of S by He^+, allows the resistivity of the material to be tuned over several orders of magnitude, resulting in distinct insulating and metallic phases to emerge.[3] The helium ion microscope is the key enabling technology in this work.

3.2 Helium Ion Microscope

The helium ion microscope unites many of the advantages of SEM and FIB in a single tool, while overcoming many of their drawbacks. Helium atoms are much more massive than electrons (7296× larger), so their de Broglie wavelength is short enough that the focussed probe is not strongly limited by diffraction effects. Also, the helium ions penetrate the sample with little scattering as compared to electrons resulting in a signal from a smaller interaction volume and thus higher resolution. A Ga ion beam is also not affected by diffraction due its much larger mass than that of an electron (12710× larger). However the liquid metal ion source (LMIS) used in the FIB has a much larger energy spread than a typical field emission gun of an SEM or the GFIS, leading to substantial chromatic aberrations in normal operating conditions which limits the spot size.[10] The large mass of Ga means it is also hard to avoid significant sputtering or amorphisation of the sample while imaging and the implantation of metal atoms in the sample may present issues for electronic devices. The mass of He ions is large enough to overcome the diffraction limits of electrons while resulting in less sample damage than Ga. As in the FIB, milling is possible in the HIM using an appropriate ion dose and can be achieved

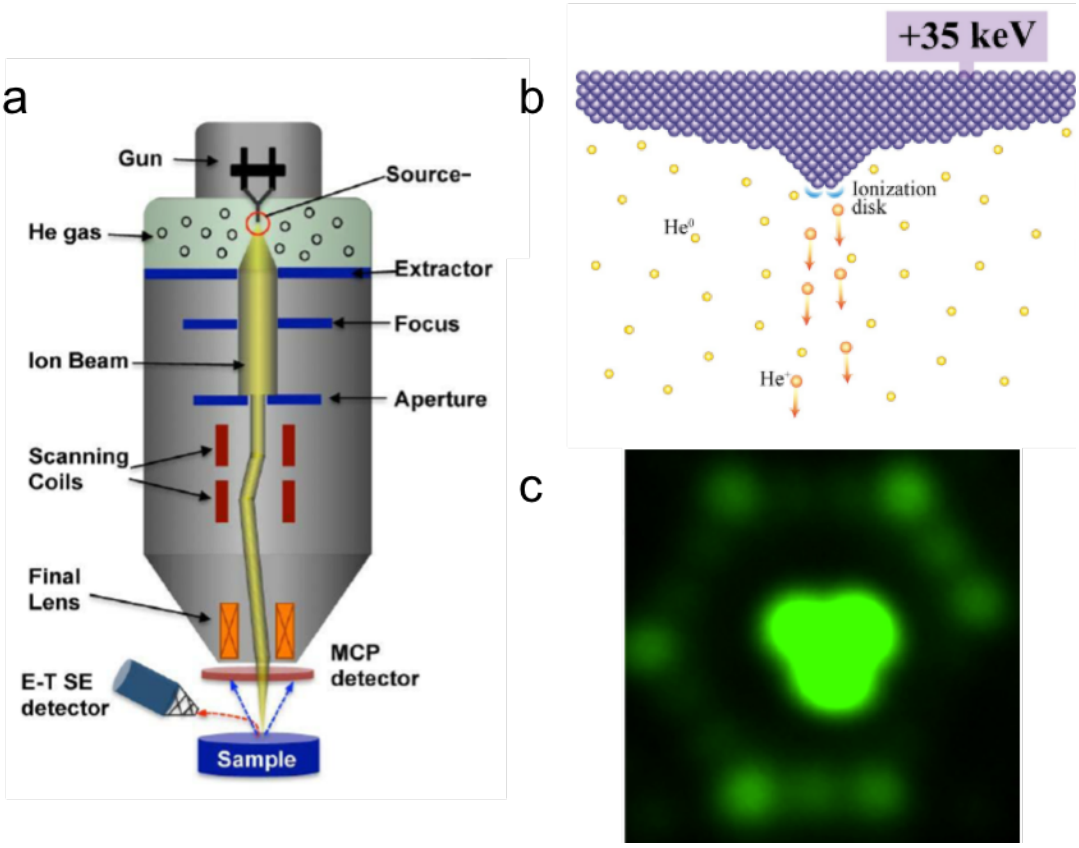

Figure 3.1 | (a) Schematic diagram of Helium Ion Microscope. The Gas Field Ion Source (GFIS) acts as a source of positively charged helium ions which are accelerated down the optical column.[25] (b) Diagram of tungsten source of the GFIS. The He gas atoms are ionised when they reach the high electric field at the apex. The ions (now positively charged) are accelerated by the field away from the source and down the microscope column. (c) SFIM image of a GFIS source. The centre trimer can be seen along with the edges and corner of the next crystal plane.[11]

with higher resolution. The fact He is a noble gas overcomes the unwanted chemical or electrical alterations of the sample.[10]

The HIM also facilitates the imaging of biological and other insulating samples without the need for a conductive coating or extensive sample preparation. This is because the He^+ ion's positive charging of the sample can be neutralised while imaging by an in-built electron flood gun.[11]

The key component enabling the HIM is its source, the gas field ion source (GFIS). The GFIS is formed from a cryogenically cooled (60 – 80 K) tungsten tip which is sharpened to an atomically sharp apex by field evaporation. Using Scanning Field Ion Microscopy

(SFIM) the apex can be monitored and shaped by using high fields to remove weakly bound atoms until a stable three atom (trimer) apex remains (see Figure 3.1c). A high electrical bias is applied between the tip and an extraction electrode and this generated field is concentrated at the apex.

Given the small size of the emission site, an extremely low 'base vacuum' pressure, that is the pressure in the absence of the imaging gas, must be maintained. This is in order to keep the apex free from adatoms which would destabilise the emission process. A rough calculation suggests a vacuum requirement on the order of 10^{-13} mbar in the region of the emitter.[12] In combination with a series of turbo pumps, which can achieve a base pressure in the range of 10^{-9} mbat, two features of the GFIS design contribute to achieving this extreme high vacuum at the emitter site. First, the cryogenic surfaces surrounding the gun provide an important degree of cryo-pumping and cryo-trapping. Secondly, due to the high electric field, undesired gas molecules are ionised as they approach the emitter when they experience an electric field surpassing their field ionisation limit (~2 V $Å^{-1}$). Thereafter, the ions are accelerated away from the emitter, leaving a small 'bubble' of extreme high vacuum bounded by the contour of the critical electric field magnitude. In contrast, as the imaging gases are noble gases, they have a much higher ionization energy and thus are not ionised until they reach the surface of the emitter.

The imaging gas (He or Ne) is injected into the GFIS chamber at low pressure, generally $\sim 1 \times 10^{-6}$ mbar. The concentrated electric field around the apex restricts the ionisation of the gas to the outer most atoms (see Figure 3.1b). The cryogenic temperature also acts to improve the collection and surface accommodation of the imaging gas, resulting in higher currents. Using an aperture in the beam path allows selection of current from ionisation events on a single apex atom which results in an atomically resolved ion source.[11,13] The brightness of the source is high, comparable to a cold field emission source, and the energy resolution is less than 0.2 – 0.5 eV.[14] This low energy spread means that at typical beam energies $\frac{\Delta E}{E} \sim 2 \times 10^{-5}$, which is much lower than low voltage SEMs and Ga FIBs, meaning the beam is less susceptible to chromatic aberrations.[10]

These ions are then accelerated down the column and are focussed using electrostatic lenses. The upper column contains a quadrupole for beam alignment and the lower column contains an octupole for astigmatism correction. A probe size of 0.3 – 0.5 nm is

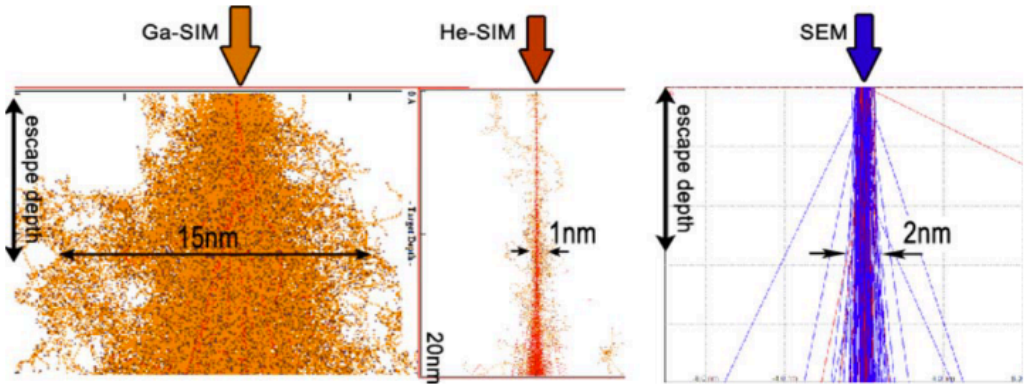

Figure 3.2 | Interaction volumes for Ga-FIB (left) HIM (centre) and SEM (right) all for beam energies of 30keV and a simulated beam of zero width. The escape depth is taken to be approximately 10nm.[19]

feasible for a He^+ beam. The beam convergence angle (<1 mrad) is typically five times smaller than that of an SEM, resulting in a depth of field which is correspondingly five times larger under the same conditions.[10] This allows imaging of objects on different planes, as well as high aspect ratio milling.

The beam current can be controlled by changing the strength of the condenser lens, or else by changing the size of the aperture, however these both also effect the probe size. Unique to GFIS, the beam current can also be altered by orders of magnitude by varying the imaging gas pressure in the tip chamber. The beam is raster scanned along a sample, similar to a SEM to produce a signal which is detected.

3.3 Beam Sample Interaction

The principles of image formation for the HIM are similar to the SEM and FIB. A beam of charged particles (ions for HIM and FIB, electrons for SEM) are focussed on a point of the sample and scanned across the surface. The beam penetrates the surface and interacts with the sample's atoms resulting in the excitation of secondary electrons (SEs) in some interaction volume. A each point, or pixel, a detector then measures the output of SEs escaping from the sample and assigns a greyscale value. The SE yield (δ) is greater in the HIM than in the SEM ($\delta \approx 7$ and $\delta \approx 0.1$ respectively) allowing a significantly higher signal to noise ratio and detection of more subtle variations in topographic and material contrast.

SEs lose energy as they travel through the sample, through collision cascades with other electrons. Only electrons which maintain enough energy to pass the surface potential barrier (on the order of 1 eV) can escape the sample for detection. Thus, only SEs generated near the sample surface (within the characteristic escape depth D_e, typically 5-15 nm for most solids) are relevant for image formation. Ultimately the imaging resolution is limited not by the probe size but by the spacial distribution of SEs generated within this escape depth.

Collisions between ions and sample atoms can be treated as two types of independent events: elastic scattering from electronic collisions and inelastic scattering from nuclear collisions. As the He^+ beam enters the sample it undergoes mainly electronic collisions, generating multiple SEs and losing kinetic energy while maintaining its direction, which is known as the electronic loss phase and occurs over a characteristic depth L. Beyond the characteristic depth the ions undergo mainly nuclear collisions which broadens the interaction volume. Nuclear collisions transfer a fraction of incident ion energy to the target atom. If this energy is greater than the binding energy of the atom, the atom is sputtered out of its lattice position and generates a SE cascade of its own. Sputtering of atoms is described in more detail in the next section. The key advantage of the HIM in achieving high resolution over the Ga FIB and SEM is its extremely fine probe and its smaller interaction volume. $L > D_e$ and thus the beam remains well columnated within the pertinent region of the sample. The Ga FIB interaction volume is never truly localised as it immediately broadens upon entering the sample. For an electron beam, the incident electrons scatter far more easily than ions. Comparison of simulated interaction volumes is shown in Figure 3.2.

3.4 Sample Modification

The focussed beam of ions enters the sample and transfers energy to the sample atoms through inelastic collisions. By modelling the atom and ion as two spheres the maximum transferrable energy (T_m) depends on the beam energy (E) and the ratio between the incident ion mass (M_1) and atom mass (M_2) given by[12]:

$$T_m = \frac{4M_1M_2}{(M_1 + M_2)^2}E \qquad \textbf{3 - 1}$$

If T_m is smaller than the threshold displacement energy (T_D) of the atom in the solid the atom remains bound in its position and the energy is converted into phonons. If $T_m > T_D$ the atom is recoiled out of its position. Thus, efficient energy transfer for a given ion occurs when the ion and sample atom are close in mass and this efficiency decreases as the masses diverge meaning a higher energy beam would be required to transfer significant kinetic energy. This dependence on atomic mass can be utilised to advance beam modification past simply removing material to altering the stoichiometry of materials with heteroatomic crystal structures. An illustration of this point relevant to this work is MoS_2 under He^+ irradiation. As the mass ratio of S and He ($\frac{M_S}{M_{He}} \approx 8$) is closer to unity than the mass ratio of Mo and He ($\frac{M_{Mo}}{M_{He}} \approx 24$) , the incoming He^+ will impart more energy to the sample S. The threshold displacement energy is also different for the different atoms in the crystal. Assuming a normally incident beam coming from above the sample, the top layer of S atoms, facing the beam, will have a higher T_D than the bottom layer as the displaced atom is effectively 'stopped' by the other layers ($T_D = 8.1\ eV$ for the top layer and $T_D = 6.9\ eV$ for the bottom layer). The displacement threshold for formation of a Mo vacancy is even higher, owing to the fact it is bonded to six neighbours rather than three ($T_D = 20\ eV$).[15] The ion interaction cross section ($\sigma_{d(ion)}$) for the removal of an atom is given by:

$$\sigma_{d(ion)} = \pi \frac{M_1}{M_2} Z_1^2 Z_2^2 e^4 \frac{1}{E} \left(\frac{1}{T_D} - \frac{1}{T_m}\right) \qquad \textbf{3 - 2}$$

where Z_1 and Z_2 are the atomic numbers of the ion and sample atom atomic number respectively, e is the electron charge.

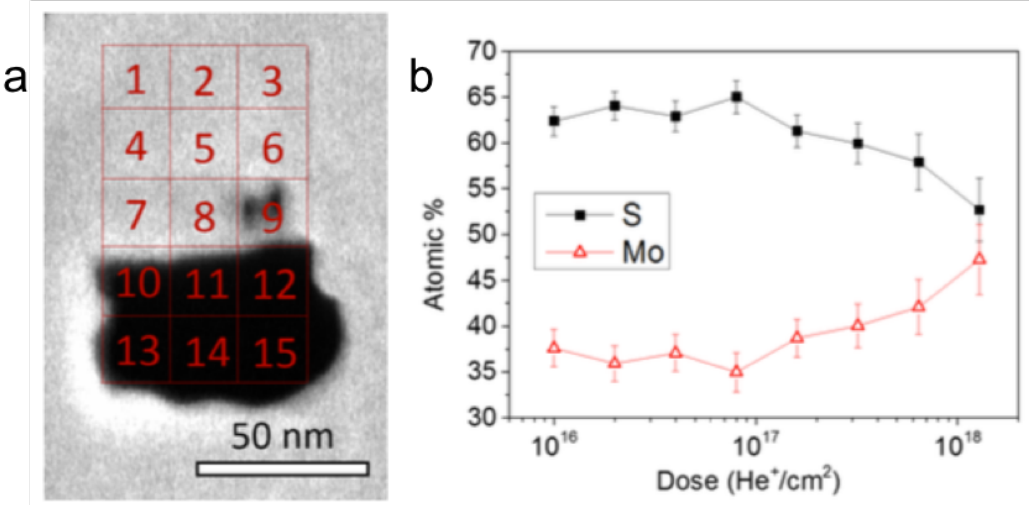

Figure 3.3 | Stoichiometry alteration of MoS_2 by He^+ irradiation. (a) STEM image of free standing MoS_2 flake irradiated with 15 different doses, beginning with 1×10^{16} He^+ cm^{-2} for region 1 and doubling with each subsequent region. (b) concentration of S and Mo extracted for the regions, extracted from EDX analysis.[3]

This preferential sputtering has been demonstrated experimentally[3]. Regions of a freestanding MoS_2 flake were irradiated with increasing dose of He^+ (Figure 3.3a). The resulting Mo and S concentrations were extracted from EDX analysis (Figure 3.3b). While preferential S sputtering in MoS_2 achievable through Ar^+ bombardment[16] the He^+ beam allows for stoichiometry tuning with a spacial resolution of just a few tens of nanometres.

3.5 Substrate Effects

In contrast to freestanding targets (e.g. MoS_2 suspended on a TEM grid) where all the defects are created by the incident ion beam, the substrate can affect defect formation in several ways. It is important to account for this as materials used for device fabrication necessitate an underlying supporting substrate. As well as by direct ion impacts, defects in supported 2D systems can be produced by backscattered ions and sputtered substrate atoms. A schematic of the mechanisms are shown in Figure 3. **4**a. Thus, sputtering yield (Y), that is number of sputtered atoms per incident He^+ ion, is higher for supported targets than for freestanding ones. Backscattered Si and O atoms from a SiO_2 substrate will have lower kinetic energy by definition than the incident beam. As we can see from equation

3 - 2**,** The interaction cross section for a projectile atom and sample atom scales as $\sigma \propto \frac{1}{E}$, so these backscattered atoms have a higher probability of collision with a target atom. In addition, from the binary collision approximation, equation 3 - 1, the mass ratio of O ($\frac{M_S}{M_O} \approx 2$) and Si ($\frac{M_S}{M_{Si}} \approx 1.1$) with sulfur are closer to unity than that of He, which results in a more efficient energy transfer in these collisions.

The substrate atoms can be backscattered at any angle and so spread laterally away from the impact point of the incident beam. Sputtering from backscattered atoms means the area in which defects are introduced is significantly enlarged compared to the beam diameter (typically <1 nm). Figure 3. **4**b shows simulated spatial distribution of defects for typical HIM energy range[17]. Defect formation remains a significant factor up to 10 nm from the incident beam. These backscattered atom effects are the main limiting factor in achievable resolution in patterning of supported 2D materials.[7]

Other effects are also present which are harder to quantify, such as in-situ annealing of defects, possible even at room temperature, and the extent to which defects can more easily be produced if an ion hits the sample in area where defects already exist. However, we can still use the calculated sputter yield to estimate the optimal ion dose to achieve a particular defect level.

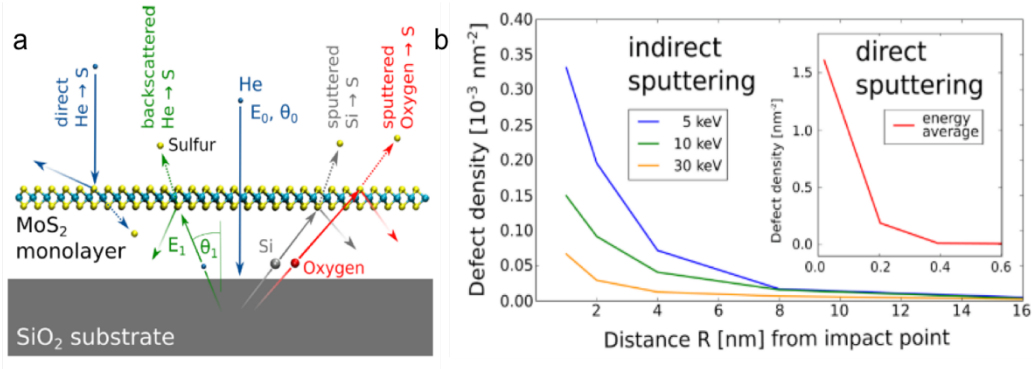

Figure 3. 4 | (a) Mechanisms for defect production in MoS_2 on SiO_2 substrate from He^+ beam. Defects can be produced from direct ion impacts, backscattered ions and atoms sputtered from the substrate. (b) Results of a simulation showing defect density from indirect sputtering as a function of distance from impact point. Three different incident beam energies are shown, compared to direct sputtering (inset).[17] The simulation used a combination of Monte Carlo methods (for projectile statistics) and molecular dynamics methods (for projectile atom interactions with the 2D layer) in its calculations.

For example, the calculated sputter yield of S atoms in MoS_2 on a SiO_2 substrate from a 30 keV He^+ beam is $Y \approx 0.008$ S atoms.[17] The dose (D) required to sputter half of all sulfur atoms from an area is then given by:

$$D = \frac{1}{2}\frac{N}{Y} \qquad \textbf{3 - 3}$$

where N is the total number of S atoms per unit area. MoS_2 has $1.5 \times 10^{15} cm^{-2}$ S atoms, which corresponds to a dose of $D \approx 1 \times 10^{17} He^+ cm^{-2}$. This matches well with experimental data from Fox et. al.[3] who observes about an order of magnitude lower dose required to achieve the same defect level on substrate as compared to a free standing sample (see Figure 3.3).

Recoiled substrate atoms need not simply sputter sample target atoms, or pass through, but can come to rest within the target lattice itself. There is a long history of using ion beams for mixing of layered solid systems, for example using ion beam irradiation of bilayer metallic systems to form alloys.[18] While this effect may be less pronounced for 2D materials owing to the atomically thin nature of the target layer, it is still present. It has been demonstrated that graphene encapsulated in hexagonal boron nitride (h-BN) irradiated with a 30 keV He^+ beam can incorporate N atoms into the C lattice as substitutional defects, which causes the effective n-doping of the graphene layer.[9]

3.6 Charging and Contamination effects

Unlike the SEM, the HIM utilises a positively charged primary beam which increases the risk of unwanted charging effect since both the incoming ions and escaping SEs contribute to positively charging the sample. Owing to the higher SE yield and small interaction volume of the HIM, this charging effect may hinder the achievable resolution of imaging and milling as the accumulated charge may perturb the trajectory of the incoming beam and escaping SEs. We can perform a quick calculation to obtain an upper bound for the accumulated charge (Q):

$$Q \approx Q_+ - Q_- \qquad 3.4$$

where Q_+ is the accumulated positive charge from the stopped ions and Q_- is the negative charge escaping from the sample. Using typical operating conditions of a SE yield of $\delta = 7$ and a beam current of $\mathrm{I} = 1$ pA, we find $\mathrm{Q} = 8 \times 10^{-12}\ \mathrm{C\,s^{-1}}$. Fortunately, as shown in Figure 3.2, the majority of incident ions are implanted deep within the sample, well away from the SE escape depth.[19] The charging effects can be significantly reduced by using an in-situ electron flood gun to neutralise the surface charge between image scans.[20] Beam induced contamination is regularly encountered in the SEM however the HIM is even more susceptible owing to its greater surface sensitivity.[21] Typically, a sample surface is never perfectly clean but has adsorbed water and hydrocarbons from the ambient atmosphere and from processing and handling. The microscope chamber and sample stage will also typically be coated with a layer of oily residue. These molecules can end up in the region of the sample surface hit by the incident beam and become polymerised and deposited in place. This causes the sample surface to change, increasing in height as contamination builds up. This effect can be monitored in real time when imaging with the HIM as the deposited hydrocarbon layer will change the SE emission yield altering the image formed.[22,23] Contamination can be significantly reduced by pre-cleaning with a low energy oxygen plasma, which is effective in removing hydrocarbons from the sample and vacuum chamber surfaces. This is not always possible however, depending on the sample in question, as it has been observed that even short exposure to oxygen plasma can cause chemical modification to MoS_2 crystals.[24]

3.7 Controlling the Ion Beam

There are many parameters which effect the material modification by the HIM. The kinetic energy of the beam can be varied from ~5 - 35 keV. As noted in section 3.2 the beam current is controlled by varying the condenser lens, the aperture and the gas pressure. The beam current represents the number of ions reaching the sample per unit time and can range from ~0.1 - 100 pA. The higher the beam current, the more quickly a particular dose of ions can be delivered. The time the beam spends at one point is known as the dwell time. Thus the beam current and dwell time are parameters used to vary the dose per point.

The size of these points is controlled by the probe size, which can be modified by the aperture and lenses. There is a general trade-off between probe size and beam current, the smaller the probe, the lower the current. The spacing between these points is known as the pixel spacing and can be specified. At each point the probe shape can be modelled as a gaussian distribution, thus a probe size equal to the pixel spacing (1 nm say) will have individual points with just the tails of the distribution overlapping. In order for a more equal dose distribution over a large area, and for efficient milling, a pixel spacing smaller than the probe size should be chosen. Typically an imaging dose is ~10^{10} - 10^{12} ions cm^{-2}.

Ultimately, vacancy formation, amorphisation and milling are controlled by the total dose delivered and are rate independent. Effects such as sample charging, inadvertent beam chemistry, and heating are dose rate dependent as there are competing rates which must be accounted for e.g. charge dissipation, adsorbate mobility or thermal dissipation. Furthermore, long exposures may be affected by sample drift relative to the beam, which would lower resolution. The HIM used in this work was a Zeiss ORION NanoFab.

This chapter outlined the helium ion microscope which is the primary tool used for material modification in this thesis. The next chapter will describe the other apparatus and methods used for fabrication and analysis in this work.

3.8 References

1. Williams, J. S. Material Modification with Ion Beams. *Rep. Prog. Phys.* **49**, 491–587 (1986).
2. Kalhor, N., Boden, S. A. & Mizuta, H. Sub-10 nm patterning by focused He-ion beam milling for fabrication of downscaled graphene nano devices. *Microelectronic Engineering* **114**, 70–77 (2014).
3. Fox, D. S. *et al.* Nanopatterning and Electrical Tuning of MoS_2 Layers with a Subnanometer Helium Ion Beam. *Nano letters* **15**, 5307–13 (2015).
4. Sidorkin, V. *et al.* Sub-10-nm nanolithography with a scanning helium beam. *Journal of Vacuum Science & Technology B: Microelectronics and Nanometer Structures* **27**, L18 (2009).
5. Stanford, M. G. *et al.* Tungsten Diselenide Patterning and Nanoribbon Formation by Gas-Assisted Focused-Helium-Ion-Beam-Induced Etching. *Small Methods* **1**, 1600060 (2017).
6. Winston, D. *et al.* Scanning-helium-ion-beam lithography with hydrogen silsesquioxane resist. *Journal of Vacuum Science & Technology B: Microelectronics and Nanometer Structures* **27**, 2702 (2009).
7. Naitou, Y., Iijima, T. & Ogawa, S. Direct nano-patterning of graphene with helium ion beams. *Applied Physics Letters* **106**, 1–5 (2015).
8. Emmrich, D. *et al.* Nanopore fabrication and characterization by helium ion microscopy. *Applied Physics Letters* **108**, (2016).
9. Nanda, G., Goswami, S., Watanabe, K., Taniguchi, T. & Alkemade, P. F. A. Defect Control and n -Doping of Encapsulated Graphene by Helium-Ion-Beam Irradiation. *Nano Letters* **15**, 4006–4012 (2015).
10. Ward, B. W., Notte, J. A. & Economou, N. P. Helium ion microscope: A new tool for nanoscale microscopy and metrology. *Journal of Vacuum Science & Technology B: Microelectronics and Nanometer Structures* **24**, 2871 (2006).
11. Hlawacek, G., Veligura, V., van Gastel, R. & Poelsema, B. Helium ion microscopy. *Journal of Vacuum Science & Technology B* **32**, 20801 (2014).
12. Hlawacek, G. & Gölzhäuser, A. *Helium Ion Microscopy*. (Springer, 2016).
13. Stanford, M. G., Lewis, B. B., Mahady, K., Fowlkes, J. D. & Rack, P. D. Review

Article: Advanced nanoscale patterning and material synthesis with gas field helium and neon ion beams. *Journal of Vacuum Science & Technology B, Nanotechnology and Microelectronics: Materials, Processing, Measurement, and Phenomena* **35**, 030802 (2017).

14. Ernst, N., Bozdech, G., Schmidt, H., Schmidt, W. A. & Larkins, G. L. On the full-width-at-half-maximum of field ion energy distributions. *Applied Surface Science* **67**, 111–117 (1993).
15. Komsa, H. P. *et al.* Two-dimensional transition metal dichalcogenides under electron irradiation: Defect production and doping. *Physical Review Letters* **109**, 1–5 (2012).
16. Baker, M. A., Gilmore, R., Lenardi, C. & Gissler, W. XPS investigation of preferential sputtering of S from MoS_2 and determination of MoSxstoichiometry from Mo and S peak positions. *Applied Surface Science* **150**, 255–262 (1999).
17. Kretschmer, S. *et al.* Supported Two-Dimensional Materials under Ion Irradiation: the Substrate Governs Defect Production. *ACS Applied Materials & Interfaces* acsami.8b08471 (2018). doi:10.1021/acsami.8b08471
18. Paine, B. M. & Averback, R. S. Ion beam mixing: Basic experiments. *Nuclear Inst. and Methods in Physics Research, B* **7**–**8**, 666–675 (1985).
19. Cohen-Tanugi, D. & Yao, N. Superior imaging quality of scanning helium-ion microscopy: A look at beam-sample interactions. *Microscopy and Microanalysis* **15**, 656–657 (2009).
20. Livengood, R. H., Greenzweig, Y., Liang, T. & Grumski, M. Helium ion microscope invasiveness and imaging study for semiconductor applications. *Journal of Vacuum Science & Technology B: Microelectronics and Nanometer Structures* **25**, 2547 (2007).
21. Postek, M. T., Vladár, A., Archie, C. & Ming, B. Review of current progress in nanometrology with the helium ion microscope. *Measurement Science and Technology* **22**, (2011).
22. Vladár, A. E., Purushotham, K. P. & Postek, M. T. Contamination specification for dimensional metrology SEMs. *Proceedings of SPIE* **6922**, 692217 (2008).
23. Zhou, Y., O'Connell, R., Maguire, P. & Zhang, H. High throughput secondary

electron imaging of organic residues on a graphene surface. *Scientific Reports* **4**, 7032 (2014).

24. Jadwiszczak, J. *et al.* Oxide-mediated recovery of field-effect mobility in plasma-treated MoS_2. *Science Advances* **4**, (2018).
25. Bell, D. C., Lemme, M. C., Stern, L. A., Williams, J. R. & Marcus, C. M. Precision cutting and patterning of graphene with helium ions. *Nanotechnology* **20**, 455301 (2009).

Chapter 4

Equipment and Methods

The fabrication of nanoscale devices requires the use of advanced sample processing and imaging techniques. This chapter describes in detail the methods used for sample preparation, device fabrication, imaging, material analysis and electrical measurement. These include microscopy such as scanning electron microscopy, atomic force microscopy and transmission electron microscopy; photoluminescent and Raman spectroscopy; mechanical exfoliation of 2D layered materials; UV and electron beam lithography; and electrical testing of semiconductor devices under vacuum. The underlying theory of these techniques is outlined as well as the specific application to the work that is presented in this thesis.

4.1 Scanning Electron Microscopy

Beginning in the early 20th century research suggested that electron beams (or cathode rays as they were then known) could be used to exceed the resolution of conventional optical microscopes (OMs). The resolving power of a microscope is constrained not only by the quality of the lenses used but by diffraction. The diffraction limit occurs when the first diffraction minimum of the image of one source point coincides with the maximum of another. This was formulated by Ernst Abbe as:

$$r = \frac{0.61\lambda}{n\sin(\theta)} \qquad \textbf{4 - 1}$$

where r is the minimum resolvable distance between two objects, λ is the wavelength of the light used, n is the refractive index of the medium between the point source and the lens and θ is the half-angle of the cone of light from the specimen plane which enters the objective.[1] For visible light this limit is ~200 nm. In 1924 *Louis de Broglie* postulated the wave nature of electrons with associated *de Broglie* wavelength given as:

$$\lambda = \frac{h}{mv} \qquad \textbf{4 - 2}$$

where h is Plank's constant, m and v are the mass and velocity of the electron respectively.[2] For electrons with kinetic energy of 30 keV, this wavelength is on the order of picometres. Using this principle in 1932 *Ernst Ruska* and *Max Knoll* developed the first electron lenses and acquired an image with electrons.[3] Shortly afterwards the resolution of these electron microscopes exceeded that of OMs.[4] The first commercial scanning electron microscopes (SEMs) became available in the 1960's and since then the SEM capabilities have grown to include a range of analytical and fabrication techniques such as energy dispersive X-ray diffraction (EDX) and electron beam lithography (EBL). The configuration of the SEM is similar to that of the helium ion microscope described in chapter 3 and is shown schematically in Figure 4.1. The electron gun provides a source of electrons which are accelerated down the microscope column towards the sample. In the column this beam of electrons is then focused by electromagnetic condenser lenses. Apertures in the column ensure the beam width is limited and the objective lens focusses the beam to a sharp probe. Scanning coils raster scan this probe over a defined area of the sample. The resulting interaction of the primary electron beam with the sample creates signals such as secondary electrons which are detected by appropriate detector and used to form the image. The sample is mounted on a stage in the chamber which is positioned at the bottom of the column. The chamber and column are kept at high vacuum (typically ~10^{-6} mbar) unless the microscope is designed to work at low vacuum.

The electron gun used in SEM systems needs to produce a stable electron beam with high current, small spot size, adjustable energy and small energy dispersion. Two types of guns are typically used, tungsten 'hairpin' cathodes or field emission sources. Field emission sources are used in more modern SEMs as they provide enhanced current with lower dispersion and generally exhibit longer lifetimes. This work made use of SEMs with both types of guns and their operation is described below.

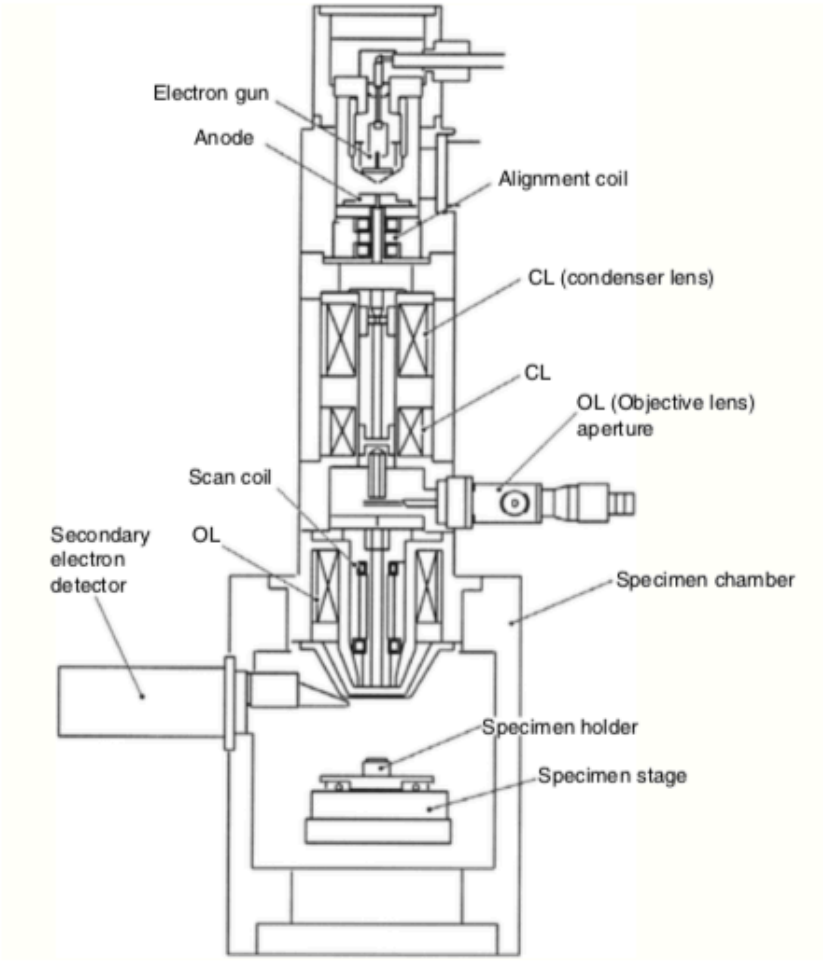

Figure 4. 1 | Schematic diagram of scanning electron microscope. The electron gun acts as a source of electrons which are accelerated down the column. The beam of electrons is focused to a fine probe by the objective lens and scanned over the surface of the sample, resulting in various signals which are detected by detectors.[1]

A *Zeiss EVO* SEM with a tungsten source was used for carrying out electrical measurements under vacuum. The beam was used for positioning the tungsten micromanipulator probes in contact with the device electrodes. This process is explained in detail in section 4.5.4. For high resolution imaging *Zeiss Ultra* and *Zeiss Supra* SEMs with field emission sources were used. The *Zeiss Supra* SEM was also used for EDX analysis of materials and EBL for device fabrication.

The tungsten thermionic electron guns are comprised of a V-shaped hairpin tungsten filament (the cathode), a Wehnelt cylinder, and an anode as shown in Figure 4.2a.

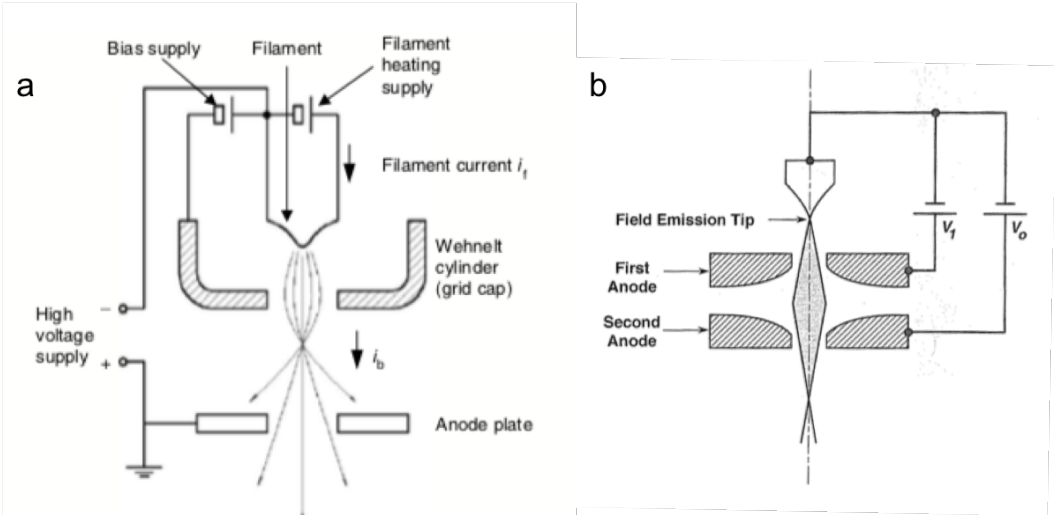

Figure 4. 2 | Schematic diagrams of electron guns. (a) Tungsten thermionic source. (b) Field emission source.[1,36]

The filament is ~100 μm in diameter and heated to a temperature over 2,800 K by applying a filament current. The high temperature allows the electrons to overcome the work function of the metal so that they escape from the cathode. A high voltage power supply is used to apply a negative potential in the range 0.1 kV – 30 kV to the filament and the Wehnelt cylinder. As the anode is kept grounded the electric field formed between the cathode and the anode extract and accelerate the electrons towards the anode. A slight negative bias is also kept between the Wehnelt cylinder and the cathode which produces crude focussing of the electron beam. Advantages of the thermionic sources is that they are inexpensive, and the vacuum requirement is relatively low. However, they have shorter lifetimes, lower brightness and larger energy spread than field emission electron guns (FEGs).

FEGs are comprised of a single crystal tungsten wire with a very sharp tip, shown schematically in Figure 4.2b. Two anodes are used in the field emission system. A voltage of a few kilovolts is applied between the first anode and the tip, and the highly concentrated electric field at the sharp tip allows the electrons to be extracted. The voltage between the tip and the grounded second electrode determines the accelerating voltage of the gun. FEGs provide electron brightness typically 100 × that of thermionic guns. Additionally, the energy spread from FEGs is typically 10 × smaller (0.3 eV vs. 3 eV),

significantly reducing chromatic aberration. FEGs must operate at ultra-high vacuum better than 10^{-9} mbar to stabilise the emission and prevent contamination.

After the electrons are emitted from the gun, they are accelerated down the column. Condenser lenses converge and collimate the beam to a relatively parallel stream. The associated condenser aperture is used to reject off axis electrons. The objective lens is used to focus the beam to a probe point at the specimen surface. The appropriate choice of lens demagnification and aperture size controls the diameter of the electron beam at the sample surface, known as the spot size. The probe cross-section may be asymmetric in shape, elliptical rather than circular, due to defects in the lens or contamination on the aperture which is known as astigmatism. Octopoles in the column referred to as 'stigmator' are used to correct the shape, allowing higher resolution to be achieved. The scanning coils are used to deflect the beam so that it scans along the sample surface. At each point along the scan a signal is detected from the beam-sample interaction and the variation in intensity of this signal is mapped to the variation brightness of a greyscale pixel. This is synchronised with the position of the scanned beam, thus a point to point image is produced.

The beam-sample interactions are key to understanding the image formation mechanism in the SEM. These interactions can be divided into two main categories: elastic interactions and inelastic interactions. Elastic scattering results from the deflection of the incident electrons by the sample atomic nucleus or by outer shell electrons of similar energy. Kinetic energy loss from the collision is negligible but results in a wide-angle direction change of the scattered electrons. If the incident electrons are scattered more than 90° , i.e. back towards the column, they are termed backscattered electrons (BSE). Inelastic scattering occurs through a variety of interactions of the primary beam with electrons and atoms of the sample, resulting in substantial energy transfer to the sample atoms. The excitation of the sample electrons by the incident electrons leads to the generation of secondary electrons (SEs). These secondary electrons can be subdivided into SE_1, SE_2 and SE_3 electrons. SE_1 electrons are generated by the primary beam so originate from the region near the incident point of the probe. SE_2 electrons are generated

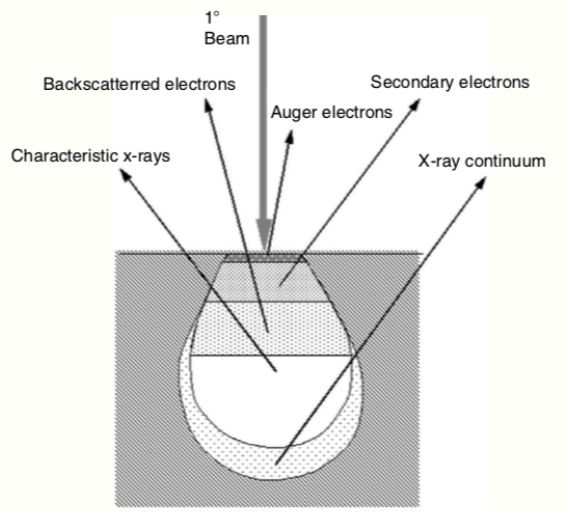

Figure 4. 3 | Schematic diagram of the beam-sample interaction volume in the scanning electron microscope and the regions from which the various signals can be detected.[1]

by backscattered incident electrons which are travelling through the material to the surface. SE_3 electrons are generated from other surfaces in the chamber excited by backscattered electrons.

The combined effect of these elastic and inelastic scattering events is to distribute the beam over a three-dimensional 'interaction volume' with dimensions on the micrometre scale. This is shown schematically in Figure4.3.

Secondary electrons typically have an energy average around 3 – 5 eV and 50 eV is considered the upper cut-off for what is considered secondary electrons. Due to this low energy SEs can only escape from a region within the first few nanometres of the sample surface, known as the escape depth and ranges from about 5 nm for metals to 50 nm for insulators.

Two types of detectors are typically used to detect secondary electrons. A detector developed by *Everhart* and *Thornley* (ET detector) is used in practically all conventional SEMs. It consists of three components, a scintillator which converts electron signal into light, a light-pipe to transport the light, and a photomultiplier tube (PMT) which converts the light signal back to electrical resulting in signal gain of 10^5 – 10^6. Positioned in the SEM chamber to one side of the sample, the ET detector collects only about 15 – 30% of the available SE_1 and SE_2 signal. This is due to the fact the SE emission intensity is

maximum normal to the sample surface (when the incident beam is also normal), so many of the SEs escape back up the column. Also, the asymmetric placement of the detector favours half of the SE distribution (those with a velocity component towards the detector). This relatively low yield of SEs is sufficient as the asymmetric detector geometry results in good topographical contrast producing shadows and highlights at edges, corners, surface roughness etc. depending on the relative position of the feature and the detector. The scintillator material emits light when struck by an energetic (~10 keV) electron. By applying a large positive potential (10 kV) to the front of the scintillator, the low energy SEs can be sufficiently accelerated to excite it. To protect the primary beam from unwanted deflection by this large potential, the scintillator is surrounded by a Faraday cage. This Faraday cage can have a separate bias applied to it, typically in the range -50 – +250 V. This provides the option to completely reject SEs (-50 V), collecting only BSE; or efficiently collecting SEs (+250 V), however with some loss of directionality.

The inLens or through-the-lens (TTL) detector is a standard ET device positioned in the column above the objective lens. Because of this, SE_3 electrons which are generated well away from the beam axis are not collected. Removing this nonspecific background signal results in higher signal to noise and enhanced contrast. Typically, 70 – 80 % of the SE signal from the sample can be collected. The top-down symmetric view means the inLens detector is less sensitive to topography, however enhanced SE_1 signal provides much greater surface sensitivity.

4.1.1 Energy-Dispersive X-ray Spectroscopy

Another signal produced by the beam-sample interaction is characteristic x-rays. These arise when incident electrons excite inner-shell electrons of the sample atoms causing inner-shell ionisation. When an outer-shell electron relaxes to fill this vacancy, an x-ray photon is emitted with an energy that is characteristic of the atomic species. A background continuum x-ray signal known as ‘Bremsstrahlung’ is also produced as incident electrons are decelerated by the electric field of the sample atomic nuclei. The characteristic x-rays can be detected by a semiconductor-based photo-detector positioned in the SEM chamber in a technique known as energy dispersive x-ray spectroscopy (EDX). This can provide quantitative elemental information about the sample. X-ray spectra are produced and

spatially correlated with the position of the scanning beam, and thus when filtered for the appropriate energy peaks, an image can be formed displaying the distribution of various elements within the sample.

4.1.2 Transmission mode SEM

SEMs can also incorporate a transmission detector. This is a charged-couple device located below the sample and used to collect the beam of electrons which have passed through the sample. The sample must be very thin for the beam to pass through, no more than 10's of nanometres. In bright-field mode electrons which have been transmitted directly through the sample are used to form the image, while in dark-field mode electrons which have been diffracted to geometry specified by the detector are used. Contrast in bright-field mode arises due to composition and thickness changes. Atomic layer thickness differences can be distinguished. The spatial resolution is generally superior (1 nm achievable) than the other SEM modes. The technique is limited by the requirement of the sample to be thin enough to be electron transparent. However, this means it is well suited to studying flakes of 2D materials as long as they are free standing.

4.1.3 Electron Beam Lithography

The SEM can also be adapted for use as a powerful nanofabrication tool. Electron beam lithography (EBL) dates back to 1961 with the first demonstration by *Mollenstedt* and *Speidel*.[5] EBL makes use of the focused electron beam to write a custom pattern onto an electron sensitive film known as a resist. The process is shown schematically in Figure 4.4. The resist is deposited on the sample and an even covering is achieved by spin coating, which is then followed by a baking step. Electron beam exposure induces changes to the molecular structure and solubility of the resist. The resist is then developed in a suitable solvent to selectively dissolve either the exposed or unexposed areas of the resist. The patterned resist can now act as a mask for a metal deposition or etching process. EBL is a direct-write technique, which means it does not require a hard mask, allowing custom patterns to be designed for each specific sample. This is critical for rapid prototyping and for fabricating contacts to 2D flakes.

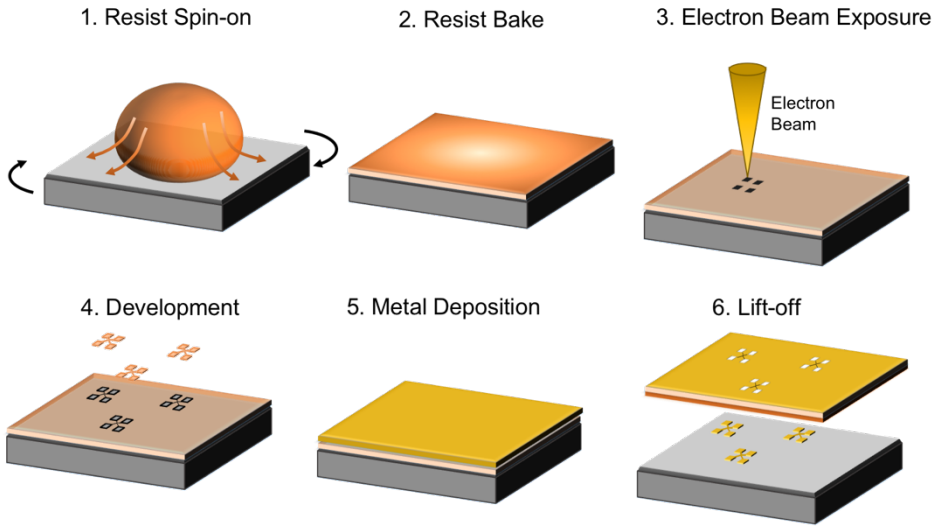

Figure 4.4 | Electron beam lithography work flow. Resist is spun on to a cleaned substrate and subsequently baked. The electron beam is exposed to regions predefined by a CAD pattern. The resist is then developed in a suitable developer. A thin layer of metal is deposited, which adheres to the substrate strongly where the resist has been removed. The remaining resist and excess metal is removed in a lift-off step in acetone. The desired metal features remain on the substrate.

During EBL the beam is controlled externally by an add-on module to the SEM which takes external control of the X-Y positioning of the beam. It also includes installing a beam blanker in the SEM column which is used to rapidly (>1 MHz) divert the beam from the column axis to prevent the electrons reaching the sample where they are not designated. These are controlled by proprietary software which includes in-built computer aided design (CAD) software for designing patterns. EBL in this work was performed on the *Zeiss Supra* SEM with the *Raith Elphy Plus* attachment.

Resists may be positive-tone or negative-tone. Positive-tone resists become more soluble in the developer on exposure to the electron beam and thus exposed areas are removed. Negative-tone resists become less soluble on exposure to the beam and so the developer leaves only the exposed areas behind. The mechanism by which the solubility is altered is either through bond-breaking or polymerisation of cross-linking hydrocarbon bonds.[1] Polymethyl-methacrylate (PMMA) is a commonly used positive-tone resist. For PMMA, bond-breaking occurs on electron beam exposure due to the relatively weak carbon-carbon and carbon-hydrogen bonds. Hydrogen silsesquioxane (HSQ) is a commonly used

negative-tone resist. Upon electron irradiation HSQ undergoes cross-linking via Si-H bond scission, resulting in an amorphous structure which is relatively insoluble in alkaline hydroxide developers.[1] HSQ is also used as a resist for helium ion lithography.

During the exposure, electrons travel through the resist can undergo multiple scattering events. Forward scattering effectively broadens the beam within the resist, increasing the line width and blurring the features. Backscattered electrons from the substrate can expose regions up to 100 nm away from the beam. This is known as the proximity effect and limits the minimum pitch of features as one exposure contributes to dose received by the other. The scattering effects will vary with beam energy. At low energy the electrons scatter readily but travel only a small distance after scattering. Higher energy electrons will scatter at a lower rate, but the scattered electron range is increased. Additionally, the clearing dose, that is the dose needed to fully expose an area, is dependent on beam energy, resulting in longer exposure times at higher beam energies. For a 20 keV beam the clearing dose is typically 50 – 500 $\mu C\ cm^{-2}$. The clearing dose will also depend on the developer used and the development time. A commonly used developer for PMMA is a 1:3 methyl isobutyl ketone (MIBK) and isopropyl alcohol (IPA) mix. Thee developing time is typically 10 – 90 s.

4.2 Transmission Electron Microscopy

The transmission electron microscope (TEM) shares many of the same features as the SEM. Electrons are sourced from a gun, accelerated down the column containing electromagnetic lenses, however they are now transmitted though the sample, where they are converged by a second series of lenses onto a detector or screen. The TEM can achieve higher resolution than any other charged beam microscopes. The electrons are accelerated to higher energy than in the SEM, typically 60 – 300 keV. From the *de Broglie* relation given in eqn. 4.2 the wavelength of an electron accelerated to 100 keV is 4×10^{-12} m and hence a diffraction limited resolution of ~ 2 pm is in principle possible. The actual achievable resolution in the TEM is limited by aberrations which cause image distortion. Spherical aberrations arise due to lens geometry and chromatic aberrations arise due to electrons with different energies being focused onto different focal planes. In recent years, breakthroughs in aberration correction has allowed atomic resolution imaging and

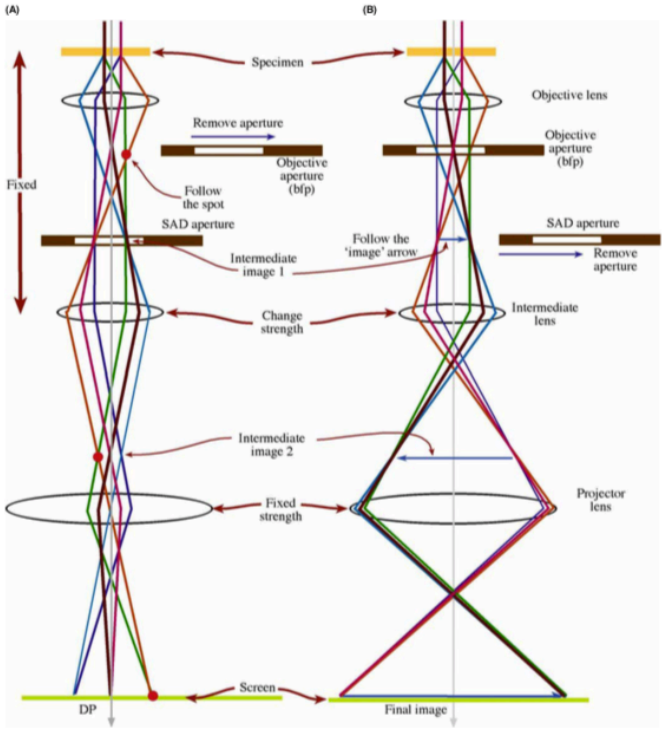

Figure 4.5 | Schematic of the TEM imaging system in (a) diffraction mode and (b) imaging mode. [4]

spectroscopic chemical mapping.[6] A separate set of aberration corrector coils in the column can be used to negate the spherical aberration caused by the lenses, while chromatic aberrations can be minimised by using an electron source with a low energy spread. Aberration correction has also allowed high resolution to be achieved at lower energy which has enabled the imaging of beam sensitive samples.[7]

In TEM the sample is illuminated by a parallel electron beam. The exiting beam first encounters the objective lens. There are two basic modes of operation of the TEM; imaging mode and diffraction mode which are shown schematically in Figure 4.5. Depending on the position and strength of the intermediate lens either the back focal plane or the image plane of the objective lens can be selected to be projected onto the detector. In imaging mode, the positioning of the objective aperture can select for either the direct beam (bright field) or one of the diffracted beams (dark field) to contribute to the image formation. A select area diffraction (SAD) aperture can be used to specify an area of the sample to contribute to the diffraction pattern in diffraction mode. Contrast arises through

a number of different mechanisms including mass-thickness contrast, diffraction contrast and phase contrast. The sample atomic mass, thickness and crystal structure all contribute to the contrast of the image. For a crystalline material at high resolution the phase contrast contributes heavily to the image formation. A fast Fourier transform (FFT) can be performed on the image which produces a reciprocal space representation of the image, analogous to the diffraction pattern. A central spot corresponds to the direct beam and surrounding spots corresponding to the diffracted beams. The intensity ratio between the central spot and the surrounding spots can give an indication of the crystallinity of the sample.[4]

The incident beam can be focused into a convergent probe at the sample plane and raster scanned in an analogous way to the SEM. This is known as scanning transmission electron microscopy (STEM). In bright field mode, the directly transmitted beam is detected. In this case the beam is weakened by its interaction with the sample and mass-thickness and diffraction contrast contribute to the image formation. Elastic interactions with the sample atomic nuclei scatter the electrons off axis. Those scattered far off axis (>10°) are incoherently scattered and are detected by what is known as a high angular annular dark field (HAADF) detector. This provides strong Z-contrast and the atomic structure of the sample is resolvable.[4] The TEM performed in this thesis was performed using an *FEI Titan 80-300 kV FEG S/TEM*.

For imaging in the TEM, the sample must be sufficiently thin (< 100 nm) in order for electrons to be transmitted. This is achieved by default in the case of 2D materials. TEM has been used extensively in the study of MoS_2, for example to investigate growth kinetics[8–10], grain boundaries[11–13], and defects[14–17]. Producing a thin sample from bulk material requires thinning by electro-polishing or by ion milling to a thin slice, known as a lamella. TEM lamellas can be prepared by milling using the FIB or more recently using

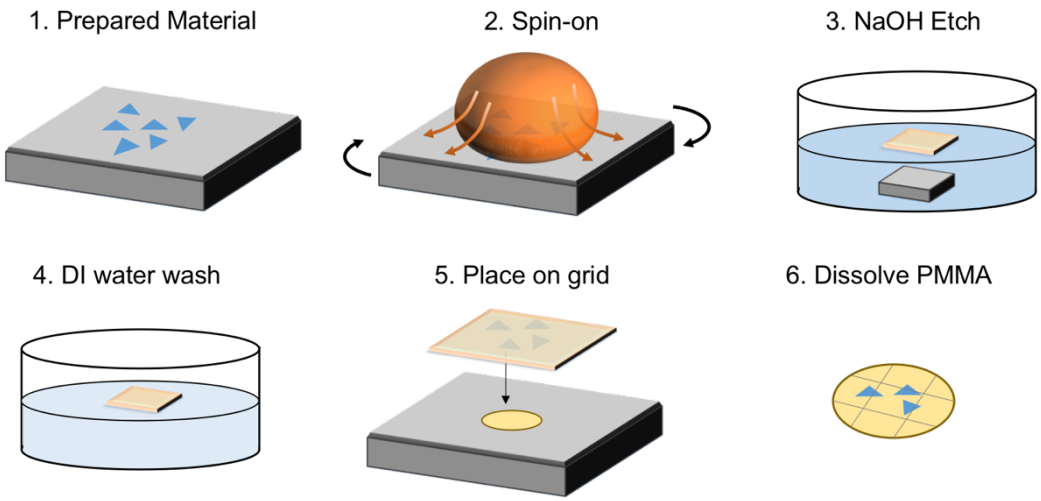

Figure 4.6 | Schematic work-flow for the transfer of MoS_2 flakes from an Si/SiO_2 substrate to a TEM grid.

the HIM. Such thin samples are inherently delicate and must be mounted on a support frame, known as a TEM grid for imaging. A common type of TEM grid used is a holey carbon grid. These are made with a ~100 μm thick copper frame covered on one side by an amorphous carbon layer (~50 nm thick) with holes which range from 100s of nanometres to microns in diameter. This allows regions of sample to be suspended over the holes, so the beam can be transmitted. Lamellas are transferred onto the TEM grid by using a micromanipulator and tip.

2D flakes or films can be transferred to a TEM grid using a polymer support. This process is outlined in Figure 4.6 for MoS_2. The material is first prepared on a Si/SiO_2 substrate by mechanical exfoliation, a process which is described in detail in section 4.5. A film of PMMA is spin-coated onto the prepared sample and baked in atmosphere on a hotplate (150°C for 3 min), as is done for EBL, described above. The sample is then floated on 2 M NaOH at 80°C which etches the SiO_2. After some time (~ 1 h) the MoS_2/PMMA film detaches from the substrate completely and remains floating on the surface of the NaOH solution. The film is then cleaned using deionised water before being transferred onto the TEM grid. Finally, the PMMA film is removed with acetone, leaving the MoS_2 flakes on the grid.

4.3 Atomic Force Microscopy

The atomic force microscope (AFM) is a form of scanning probe microscope (SPM) which was developed by *Gerd Binnig*, *Calvin Quate* and *Christoph Gerber*.[18] SPM utilises a physical probe rather than a beam of radiation (light, electrons, ions) to interrogate the sample. As there are no diffraction effects or lens aberrations to overcome extremely high resolution is achievable and is limited only by the size of the probe. The AFM emerged from earlier work[19] by *Binnig* and *Heinrich Rohrer* on the scanning tunnelling microscope (STM), for which they won the Nobel Prize, as a way to expand the capabilities of the STM to insulating samples. The AFM operates by raster scanning a sharp tip (typically 10's of nanometres at its apex) over the sample surface while monitoring and controlling the tip-sample interaction via feedback electronics. In this way the tip can track the variations in height of the sample surface and a 3-dimensional topographic map can be built up. Importantly, quantitative height information of surface features can be extracted. Furthermore, the probe can be used to perform force measurements either impinging normally into the surface or laterally to measure shear forces. By using specialised tips, it is possible to probe a range of different interactions such as magnetic, electrical, thermal forces.[20]

The AFM is comprised of a few key components including the probe, the piezo scanners, the force sensor, feedback electronics. These are shown schematically in Figure 4.7. The AFM used for work in this thesis was the *Asylum Instruments MFP-3D.*

The probe is the crux of the instrument as it is brought in closest contact with the sample and gives rise to the image through its force interactions with the surface. The probe consists of a tip which is mounted on the end of a small cantilever fabricated from a single piece of silicon or silicon nitride. The cantilever itself is mounted on a chip which is millimetres in dimension and can be picked up with tweezers. The probe is considered a consumable part of the AFM and needs to be replaced regularly as the tip succumbs to wear.

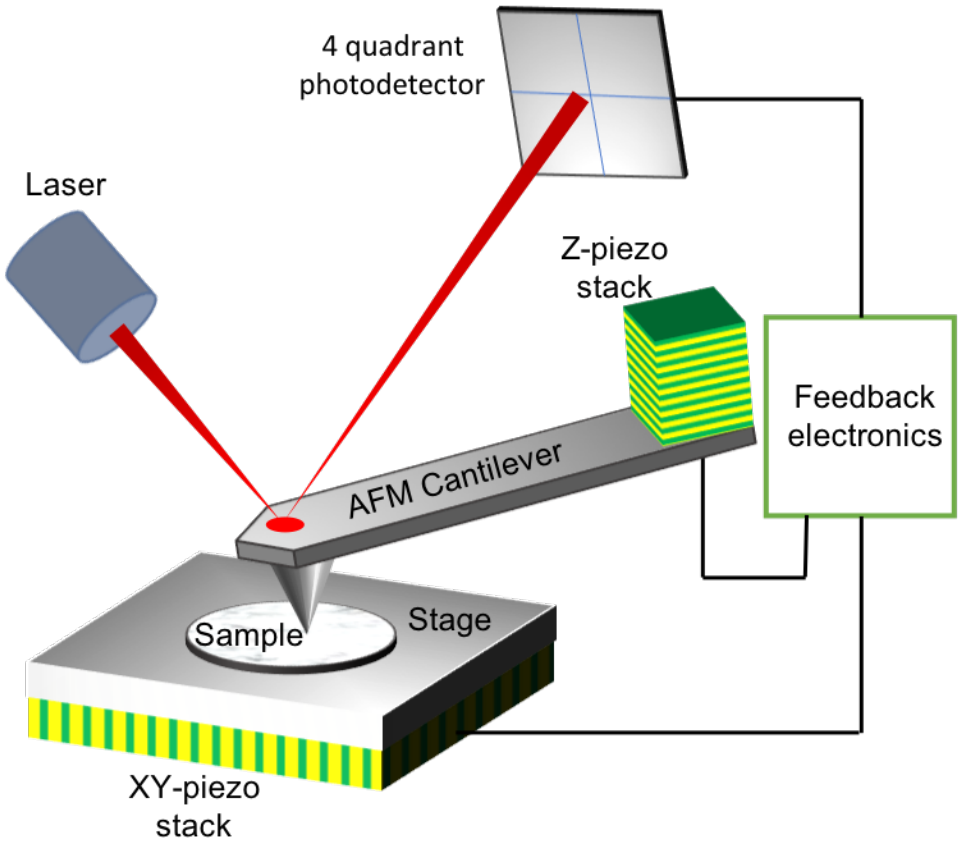

Figure 4.7 | Schematic diagram of an AFM. The cantilever deflection is measured on the photodetector as the sample is scanned with the piezo scanners.

The apex of standard AFM tips is around 20 nm, while high resolution tips can have an apex ~ 5nm. Single carbon nanotubes have been used as tips to achieve ultra-high resolution.[21] The AFM can achieve 0.1 nm vertical resolution however lateral resolution is lower due to the tip pyramidal shape. As the tip encounters a feature which is higher than its current position, the angular edge of the tip will start imaging this before the apex. Thus, lateral dimensions tend to be not reliable. Using higher aspect ratio tips can mitigate this problem. The cantilever may be coated in a reflective metal such as aluminium to increase reflectivity and thus, signal to the detector.

The movement of the probe relative to the sample surface in three dimensions is performed by piezoelectric scanners. In the *Asylum* AFM the X and Y direction scanners are built into the stage, which scans the sample laterally under the probe. The Z direction scanner is built into the head unit which houses the probe, allowing it to move vertically.

The scanners are made from piezoelectric materials which expand and contract in response to an applied voltage. The piezo scanners allow for extremely fine movements of ~0.1 nm. The response to the applied voltage is not always linear so the scanners also contain displacement sensors to accurately track their position. In the closed-loop configuration the sensors are calibrated and feedback to the piezo actuators in real time to correct the nonlinearities.

The position of the tip is magnified and detected by an 'optical lever' which acts as the force sensor. A laser or super-luminescent diode is aligned to the backside of the cantilever. The beam is reflected by the cantilever onto a four-quadrant photodetector (PD). Any small deflection of the cantilever will tilt the reflected beam and change its position on the PD. The ratio between the four quadrants indicates the position of the laser spot and thus can monitor both the vertical and lateral motion of the cantilever. Typically, the distance between the cantilever and the detector is three orders of magnitude greater than the length of the cantilever thus the optical lever greatly magnifies the motion of the tip yielding high sensitivity.

There are two modes of operation in AFM: contact mode and tapping or alternating contact (AC) mode. In contact mode the tip is brought into contact with the sample surface. Figure 4.8 shows a simplified plot of the force variation vs. distance between the tip and the sample. As the tip approaches, it first experiences a long-range attractive force. As the distance is decreased a strong, short- range repulsive begins to counteract the attractive force, until the net force is solely repulsive. Contact mode operates entirely in the repulsive regime. As the tip encounters the repulsive forces of the surface this cause the cantilever to bend and this deflection if measured by the optical lever. The force applied to the surface by the probe is given by Hooke's law:

$$F = -k \times D \qquad \textbf{4 - 3}$$

where F is the force, k is the cantilever force constant and D is the deflection distance. The feedback electronics act to keep this force at a certain value known as the force set-point, which is set by the operator.

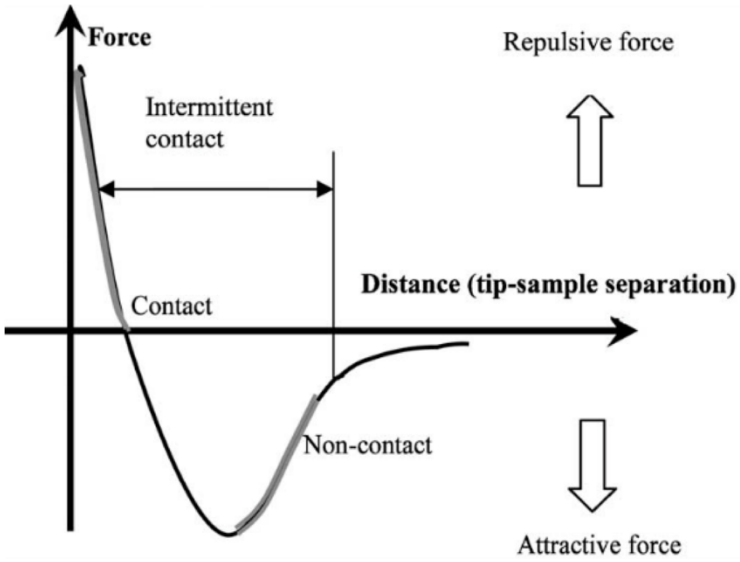

Figure 4.8 | Force variation versus distance between AFM tip and sample surface.

As the tip is scanned laterally over the sample deviations from this set point act as an error signal which is fed back to the Z-piezo actuator, raising or lowering the cantilever to restore the desired deflection. The voltage applied by the amplifier to the piezo element is a measure of the topography and is recorded as function of the lateral sample position. In tapping-mode the cantilever is oscillated at or near its resonant frequency, typically 50 – 500 kHz at an amplitude typically 20 – 100 nm. This amplitude is measured on the photodetector with the optical lever. The vibrating tip is brought close to the sample until it begins to lightly tap the surface, oscillating in and out of the repulsive regime shown in Figure 4.8. This causes damping of the cantilever vibration, reducing the amplitude. An amplitude set-point is chosen by the operator, typically 60 – 80 % of the free air amplitude. As the tip is scanned, surface features will cause this amplitude to change, due to greater or lesser damping. As in contact mode, this difference acts as an error signal which is fed back to the Z-piezo to adjust the height of the cantilever and maintain a constant amplitude. The z-position is thereby tracked as a function of sample position and can be displayed as a height map. The error signal itself, i.e. variation in amplitude, can also form an amplitude map, which is useful in providing edge contrast. Additionally, the phase shift between the cantilever oscillation relative to the driving frequency is also recorded. This provides information on local properties such as stiffness, viscosity and adhesion. Although difficult to interpret quantitatively, qualitatively the phase maps

provide good material contrast. The main advantage of tapping mode AFM is it overcomes the adhesion and frictional forces as the tip scans the surface which can lead to image artefacts. Also, less force is applied to the sample resulting in less damage to sensitive samples and less wear on the tip.

Another AFM mode known as non-contact mode oscillates the probe further from the sample surface, in the attractive regime indicated in Figure 4.8. This requires a specifically designed AFM and is performed in ultra-high vacuum. Atomic resolution is achievable in this mode.[22]

4.4 Raman and Photoluminescent Spectroscopy

Raman spectroscopy is a powerful, non-destructive, technique for characterising the structural properties of materials. Monochromatic laser light is used to probe the material by inelastic scattering which involves an exchange of energy between the incident photon and the vibrational mode of the material. The resultant scattered photons are detected by a charge-coupled device (CCD) and plotted as an energy shift from the incident beam. Peaks on this spectrum correspond to vibrational modes in the material and reveal information about crystal structure, strain, defect level, and doping.[23]

The Raman effect was discovered by *Sir C. V. Raman* in 1928[24] for which he received the Nobel Prize in Physics in 1930. It was not until decades later with the development of the laser in the 1960s that routine Raman spectroscopic experiments became possible. In the 1970s and 1980s, the development of CCDs[25] allowed simultaneous detection over a broad band replacing the previously used photomultiplier tubes (PMT) and increasing efficiency by at least three orders of magnitude. *William Boyle* and *George E. Smith* were awarded the Nobel Prize in 2009 for the invention of the CCD camera. When a photon of visible light, too low in energy to excite an electronic transition, interacts with a material it can be scattered in one of three ways, which are shown pictorially in Figure 4.9.

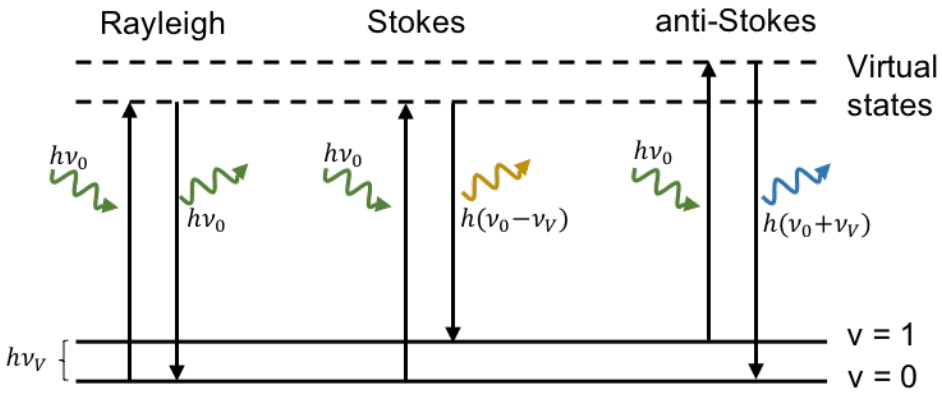

Figure 4.9 | Idealised model of Rayleigh scattering and Stokes and anti-Stokes scattering.

Most light is scattered elastically, which is known as Rayleigh scattering. The scattered photon will have the same frequency as the incoming photon (ν_0). This does not offer any information about the system under study, only the incident light in the system. The rest of the light is scattered inelastically, which is known as Raman scattering and is very weak (~ 10^{-5} of the incident beam).[26] This involves the exchange of energy between the incident photon and the vibrational modes of the material. These vibrational modes are themselves quantised. The scattered photon will have either gained or lost energy and have frequencies of $\nu_0 + \nu_V$ or $\nu_0 - \nu_V$, which correspond to anti-Stokes and Stokes scattering respectively. The ν_V term corresponds to the frequency of the vibrational mode interacted with. Stokes Raman scattering arises from the transitions which start in the ground state vibrational energy level and finish at a higher vibrational energy level, whereas anti-Stokes Raman scattering results from a transition from a higher to a lower vibrational energy state. The anti-Stokes scattering lines will be mirrored in position around the Rayleigh peak to the Stokes lines. However, at room temperature, the ground states are much more populated than the excited states, thus anti-Stoke transitions are less likely to occur than Stokes transitions resulting in Stokes Raman scattering being more intense. This relative intensity becomes greater as the energy of the vibrations increase. These are shown schematically in Figure 4.10. For this reason, it is usually the Stokes Raman scattering which is studied in Raman spectroscopy.

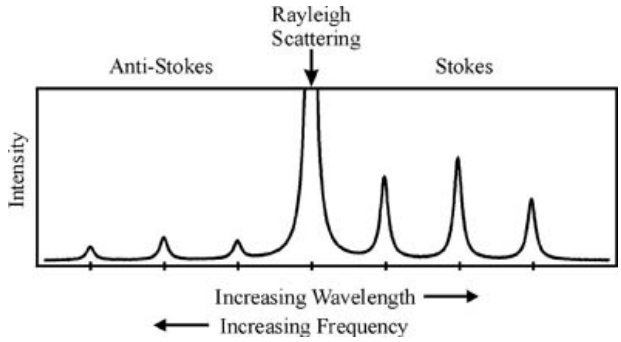

Figure 4.10 | Schematic diagram of Stokes and anti-Stokes scattering peaks. The peaks are positioned symmetrically around the Rayleigh line, while the Stokes peaks have a greater intensity.

Vibrational modes which result in peaks in the Raman spectrum are denoted as Raman-active. Other vibrational modes may be Raman-inactive but may be infrared (IR) active. Selection rules derived from group theory specify which modes are Raman or IR active (or neither). For centrosymmetric molecules Raman and IR modes are mutually exclusive. More complex molecules without a centre of symmetry can have modes which are active in both. In order for a vibrational mode to be Raman active there must be a non-zero rate of change to the polarizability of the molecule with the vibration.[26] Raman and IR spectroscopy can be thought of as complimentary techniques, each detecting different vibrational modes. In practice, Raman spectroscopy detects scattered light using a grating to disperse the scattered photons based on their energy while IR spectroscopy typically detects transmitted photons.

The layout of a Raman microscope is shown in Figure 4.11. To obtain a Raman spectrum a monochromatic light source (a laser) is focused onto the sample. The spacial resolution is limited by diffraction so the signal is typically collected over a > 300 nm region of the sample. The incident photons interact and excite the sample as discussed above after which the emitted photons are collected with a lens onto a diffraction grating. The grating spatially separates the photons according to their energy at which point they are detected by a CCD array. The grating density (grooves mm^{-1}) determines the dispersion characteristics of the signal.

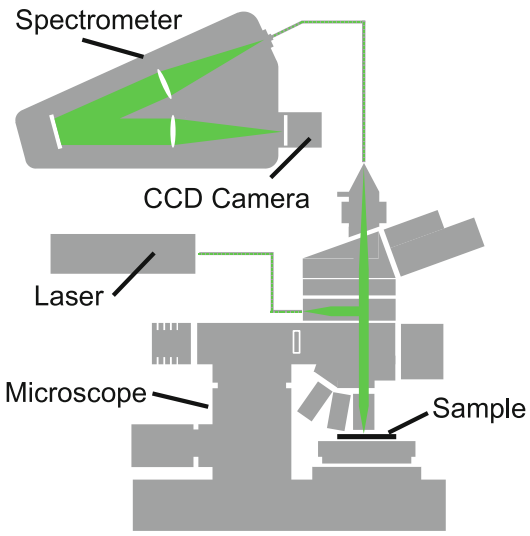

Figure 4.11 | Typical layout of a Raman microscope with a fibre-coupled laser source and spectrometer.[23]

A higher density grating results in greater dispersion and thus higher energy resolution, while trading-off the range of energy detected. The collected spectrum is plotted as an energy shift, or Raman shift, from the incident wavelength. Typically, this is outputted as counts from the CCD, which can be plotted as arbitrary units (a.u.), vs. wavenumber in cm^{-1}. Raman spectroscopy can be performed in ambient conditions with minimal sample preparation, yielding high throughput. Additionally, the technique is typically non-invasive although thermal damage to the sample may occur if an excessively high laser power is used.

As mentioned above, molecular vibrational modes are quantised so one might expect perfectly sharp spectral peaks at well-defined energies. However, many environmental factors affect the peaks such as density and distribution of defects, surface adsorbates, strain, doping, temperature etc. The resultant spectrum is a sum of all the active vibrational modes and these environmental factors. Additionally, the spectrum may contain a fluorescent signal which arises due to the coupling of the vibrational transition with an electronic transition. The peak from a fluorescent signal appears as a wide background signal in the Raman spectrum. Using a confocal detection setup limits the collection of fluorescence to photons from the focal plane. Typically this can be removed

by background subtraction or curve fitting in software.[27] Fluorescence arises commonly in the spectra of electron and ion irradiated materials due to the presence of beam induced deposition (BID) of amorphous carbon.

In order to quantitatively evaluate the peaks that appear in a Raman spectrum, they are usually fitted in software to a Gaussian or Lorentzian distribution. From this the full width at half maximum (FWHM), the position, and the height (intensity) of the peaks can be extracted. Peaks are identified by their position which act as a fingerprint for a material. These quantities are affected by the quality and environment of the material. For example, for MoS_2 the relative separation of the E' and the A_1' (or their bulk counterparts) allows the determination of thickness by layer number.[28]

A further advancement of the Raman spectroscopy technique is achieved by equipping the apparatus with a stepper motor driven positioning stage. This allows the laser probe to raster scan the sample and collect Raman spectra at a given number of sample positions. This technique is known as Raman mapping, and can be used to create a map of the distribution of chemical components in the sample.[23] Resolution is limited by the laser spot size ~500 nm. This technique can be used, for example, to map the spacial distribution of defects in MoS_2.[29] The throughput of this technique is relatively low. For example, using an integration time of 1s/spectrum, a 60×60 pixel map takes 3600 s = 1 h.

Raman spectroscopy carried out in this thesis was performed with a *WITec alpha 300R* with a 532 nm excitation wavelength laser, a $100\times$ objective lens (NA = 0.95, spot size ~300 nm), and a 1800 grooves mm^{-1} diffraction grating.

4.4.1 Photoluminescence Spectroscopy

Luminescence is a phenomenon that involves the emission of light caused by the relaxation of an electron from a higher energy excited state. Photoluminescence (PL) is the case in which the electron is excited to the higher energy level by the absorption of an incident photon. For semiconductor research, laser light provides photons of higher energy than the material bandgap.

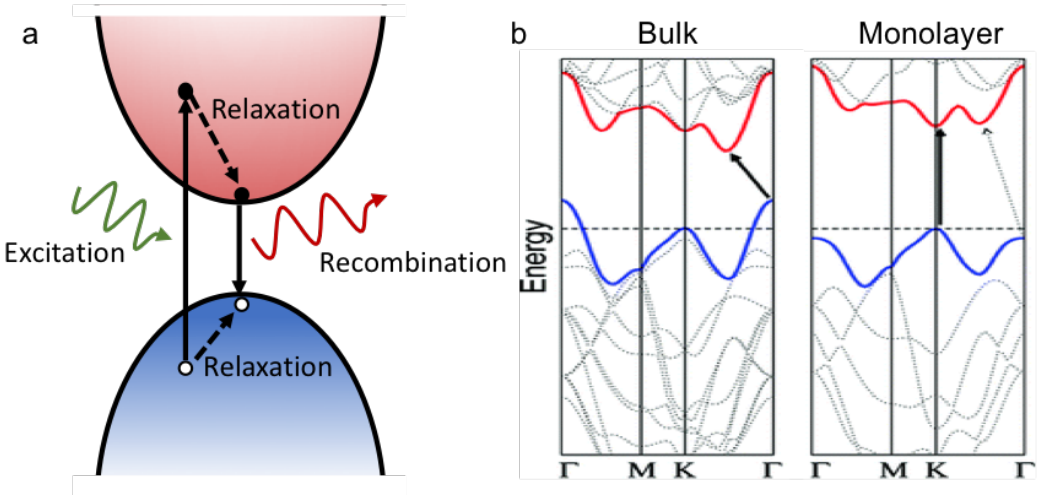

Figure 4.12 | (a) Schematic for the excitation, relaxation and recombination process of photoluminescence. (b) Band diagram of bulk and monolayer MoS_2. The solid arrow indicates the lowest energy transition in each case.[30]

The photons are absorbed forming an electron-hole pair in the conduction and valance bands respectively. These then undergo energy and momentum relaxation towards the energy gap minimum. Finally, the electrons recombine with holes emitting a photon of lower energy than the incident beam. This process is illustrated in Figure 4.12a.

PL spectroscopy probes a fundamentally different interaction than Raman, electronic states rather than atomic vibrations. However, both require the illumination of the sample with a monochromatic light source and the collection of emitted photons as a function of their energy. Indeed, PL and Raman are performed using the same instrument, and PL maps can be acquired in the same manner as Raman maps.

PL is valuable tool for characterising MoS_2. As seen in the band diagram in Figure 4.12b, MoS_2 undergoes an indirect to direct bandgap transition as it is thinned from bulk to monolayer. This results in a dramatic increase in quantum efficiency in the single-layer case.[30] The PL spectral peaks also depend on the crystal structure quality and can be used to investigate defects.[31]

PL spectra for this thesis were acquired as described above, using the *WITec alpha 300R*, with a 532 nm excitation laser and a 1800 gratings mm^{-1} diffraction grating.

4.5 Device Fabrication

This thesis is concerned with the electrical behaviour of ion beam modified MoS_2 devices. Fabrication of electrical contacts to isolated 2D flakes requires a complex, multistep process which is outlined below.

4.5.1 Substrate Preparation

Substrates used in this work were silicon wafers with a 285 nm thermal oxide supplied by *Graphene Supermarket*. The 100 mm diameter wafers were cleaved into 6 approximately equally sized pieces to carry out UV lithography. UV lithography works on a similar principle to EBL however all patterns are exposed in parallel with a mercury vapour discharge lamp. UV lithography is used to define alignment marks which are needed for later fabrication steps and a hard mask. The alignment marks consist of an array of crosses at a regular 200 μm spacing. These crosses are indexed with a pair of letters A through Z (excluding Q) denoting the X and Y position. Prior to lithography the substrates are clean by sonicating in acetone for 5 min followed by sonicating in IPA for 5 min. They are then dried under N_2 flow followed by a dehydration bake on a hotplate at 150°C for 2 min to desorb volatile organic contaminates. The lithography procedure is outlined in table 4.1 below.

Table 4.1 | UV lithography protocol.

UV lithography procedure
1. Spin-on S1813 resist at 5000 RPM for 45 s with a 5 s ramp up at 500 RPM.
2. Soft bake on hotplate at 115°C for 75 s.
3. Expose to 365 nm for 5.5 s. (Dose = 66 mJ cm^{-2}).
4. Develop in MF319 (*Shipley*) for 45 s. Stop in DI water.

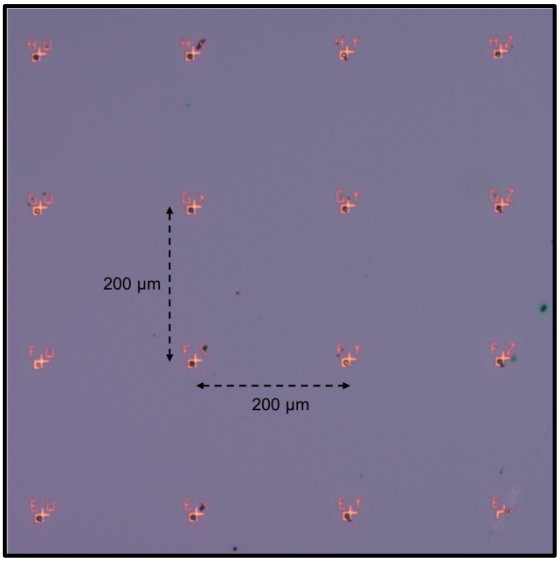

Figure 4.13 | Indexed alignment marks deposited on Si/SiO_2 substrate.

Following development of the resist, a film of Ti/Au (5 nm/35 nm) is deposited onto the sample using the *Temescal FC-2000* electron beam evaporator. The Ti layer acts as adhesion layer between the Au layer and the SiO_2 surface. The metallised sample is then placed in acetone overnight which lifts-off the resist and the excess metal layer, leaving the metal alignment marks on the substrate. An optical image of the alignment marks is shown in Figure 4.13.

The substrates can now be cleaved to size (typically 8 mm × 8 mm) when needed. Prior to use the chips are clean once again in a sonic bath as described above.

4.5.2 Mechanical Exfoliation

Monolayer and few-layer MoS_2 is isolated from bulk via mechanical exfoliation with *Scotch* tape. This method produces crystals with good structural integrity but of small lateral size, typically < 10 µm. The yield of monolayer flakes to thicker flakes is also very low. An exfoliation onto an 8 mm × 8 mm chip typically yields only 1 or 2 monolayer nanosheets. The advantage of this method is that it is a simple, low-cost way of preparing high quality samples. Bulk MoS_2 crystals were supplied by *SPI Supplies.* A schematic workflow for the exfoliation is shown in Figure 4.14.

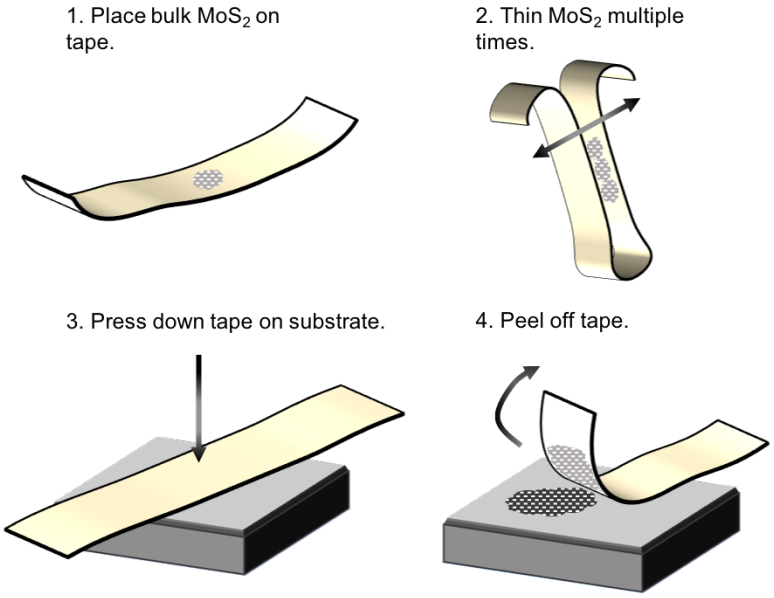

Figure 4.14 | Schematic workflow for the mechanical exfoliation of MoS_2.

First a small piece (~ 5 mm) of bulk MoS_2 is placed on the adhesive side of a strip of *Scotch* tape about 20 cm long. The MoS_2 is then thinned by repeatedly folding and peeling to different areas of the same piece of tape. This is done approximately 10 times which results in good coverage of the tape with MoS_2. The tape is then pressed, adhesive side down onto the surface of the substrate with intermittent pressure applied for ~ 5 min. Following this, the tape is peeled back slowly, leaving MoS_2 deposited on the substrate. The sample is bathed in acetone (5 min) and IPA (5 min) before drying under airflow to remove tape residue.

The mechanical exfoliation method produces flakes of MoS_2 of varying thickness. As the electronic properties of 2D nanomaterials are closely related to their layer thickness it is important to be able to determine the location and layer-number of the exfoliated mono- and few-layer nanosheets among the 'debris-field' of thicker flakes. This needs to be done efficiently over the millimetre-sized area of the substrate. A reliable method has been developed which uses the optical contrast between the 2D nanosheet and the substrate as imaged by an optical microscope.[32,33]

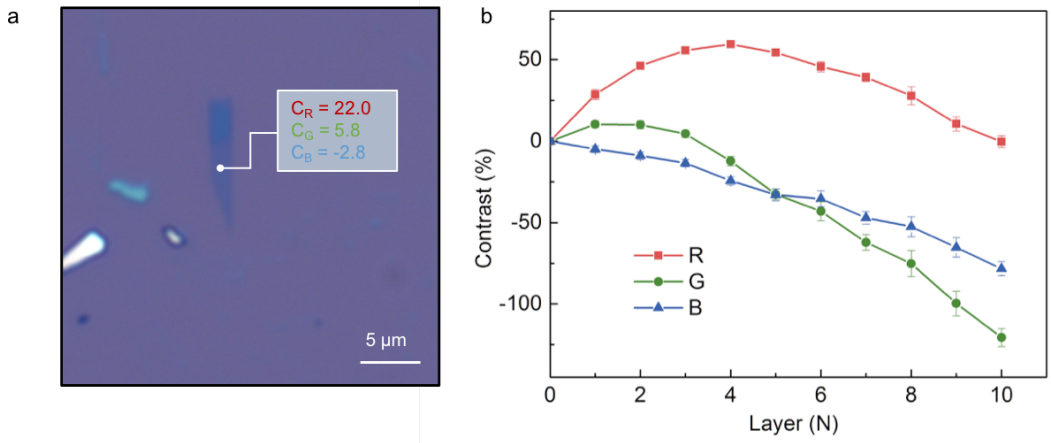

Figure 4.15 | (a) Optical image at 50× magnification of mechanically exfoliation MoS_2 on 285 nm SiO_2/Si. The optical contrast values for the monolayer portion of the flake are shown. **(b)** Graph of optical contrast values for the R G and B channels as a function of MoS_2 layer number.

The image is processed using the *ImageJ* software to separate the colour image into the greyscale (intensity) values for the R G and B channels. For each channel the contrast (C) is calculated as:

$$C = \frac{I_{sub} - I_{2D}}{I_{sub}} \qquad \textbf{4 - 4}$$

where I_{sub} and I_{2D} are the intensity values for a region of the substrate and a region of the flake respectively. These three contrast values are then compared to the chart shown in Figure 4.15b to guide the layer number identification. Figure 4.15a shows a mechanically exfoliated MoS_2 nanosheet annotated with its R G B contrast values indicating that it is a monolayer flake.

A clear advantage the optical contrast technique is its speed and simplicity. The only equipment needed is and optical microscope with a digital camera. This technique can be used for many 2D materials (TMDCs, graphene, boron nitride) on many different substrate (SiO_2 of a range of thickness, Al_2O_3).[34] This method is much faster than using AFM to directly measure the thickness of the flake, which itself poses some problems. Anomalous AFM height measurements have been reported for MoS_2 on SiO_2.[35] Offsets of 2 – 3 nm can be seen in the nominal step-height of ~0.7 nm of a monolayer. This has been attributed to the difference in tip-sample tip-substrate adhesion effects, the presence of an interlayer of adsorbed water between the nanosheet and the substrate, or the

presence of further residual surface contaminates. Whatever the source, this means that exact layer number of few-layer sheets may be ambiguous and the measurement should not be relied on for layer identification.

Work in this thesis uses both mechanically exfoliated and CVD grown MoS_2. The CVD growth was carried out by collaborators at TCD (*Conor P. Cullen*) with the method outlined in chapter 5. Typically for this work isolated, single domain, monolayers were required, rather than continuous films. These are unambiguously identifiable with the optical microscope due to their distinctive equilateral triangular shape which arises from the growth kinetics. Thus, for these samples no further thickness characterisation was performed.

Once an appropriate MoS_2 flake is identified its location is catalogued with reference to the closest alignment mark for further processing.

4.5.3 Electron Beam Lithography

After individual MoS_2 flakes have been identified, an optical photograph is taken at 20× magnification with two of the UV lithography defined alignment marks in the field of view. This image is then processed using *DraftSight* CAD software. This software is used to produce a vector graphic of the outline of the flake which is correctly scaled and aligned to the alignment grid. The .dxf file produced can be imported into *Raith* in which the electrode patterns are designed using the in-built CAD capabilities. A writefield of 600 × 600 μm was used for the patterns which included large-area contact pads (50 × 50 μm) leading to the small electrodes (1 μm wide) in contact with the MoS_2. Once the patterns are designed the resist is spun on the sample and the exposure is performed with the SEM. Table 4.2 outlines the parameters used for the EBL process.

When the samples are loaded, prior to exposure in the SEM, the beam current is measured by focussing the beam into a Faraday cup. Larger beam currents limit the achievable resolution however require shorter exposure times. Large currents were used in this work in order to shorten the time taken to expose the contact pads. Excessive exposure times run the risk of misalignment due to thermal drift of the stage.

Table 4.2

Electron beam lithography procedure
1. Spin-on PMMA A3 resist at 6000 RPM for 45 s with a 5 s ramp up at 500 RPM.
2. Soft bake on hotplate at 180°C for 180 s.
3. Electron beam exposure with following parameters. Accelerating voltage: 20 kV Aperture size: 20 μm Beam Current: ~300 pA Clearing Dose: 300 μC cm^{-2}
4. Develop in MIBK : IPA (1:3) for 45 s. Stop in IPA.

Once the beam current is measured an alignment procedure is performed using *Raith*. This defines a new coordinate system concordant with the alignment marks previously defined with UV lithography. The stage is then driven, with the beam blanked, to centre on the mark closest to the MoS_2 flake, previously noted. Final adjustments are made to align the writefield more accurately using nearby marks and the exposure is performed. The resist is developed using the parameters in table 4.2.

Once the pattern is developed it is checked with the optical microscope for correct alignment and complete exposure. Misalignment may cause the pattern to be offset from the intended flake. As the flakes are only a few microns in length, misalignment greater than 1 μm will typically result in the electrode not contacting the flake. If the resist is underexposed the developer will fail to remove it from the required area. Thus, the electrodes will not adhere to the sample surface and will be removed along with the film during the lift-off step. If the resist is overexposed the neighbouring regions of opposing electrodes may merge causing the device to be shorted.

The same metal deposition procedure as outlined for UV lithography can then be performed to deposit the electrodes.

4.5.4 Electrical measurements

The electrical characterisation in this work was primarily performed with the *Keysight B2912A* source-measurement unit (SMU). The two channel outputs on this unit were connected via coaxial cables to *Imina Technologies miBot* mobile probes, shown in Figure 4.16b. These probes are piezo-actuated allowing movement over millimetre scale with a resolution down to a few tenths of nanometres. The probes are mounted on the *miBot* stage which houses the controller. This stage is inserted into the chamber of the *Zeiss Evo* SEM chamber. This allow the electrical measurements to be performed under vacuum. A three-probe configuration was used shown schematically in Figure 4.16a. The silicon chip is mounted on copper tape to allow contacting for back-gating. The tape itself is mounted on a glass microscope slide to isolate the back gate from the grounded stage. One output channel of the SMU is used for the source and drain while the second channel is used for the gate probe. The SEM is used to position the probes in contact with the device contact pads. Figure 4.16c shows an SEM image of a device with the source and drain probes contacted. The SMU was controlled using the proprietary *B2900A Quick IV* measurement software to specify the measurement parameters.

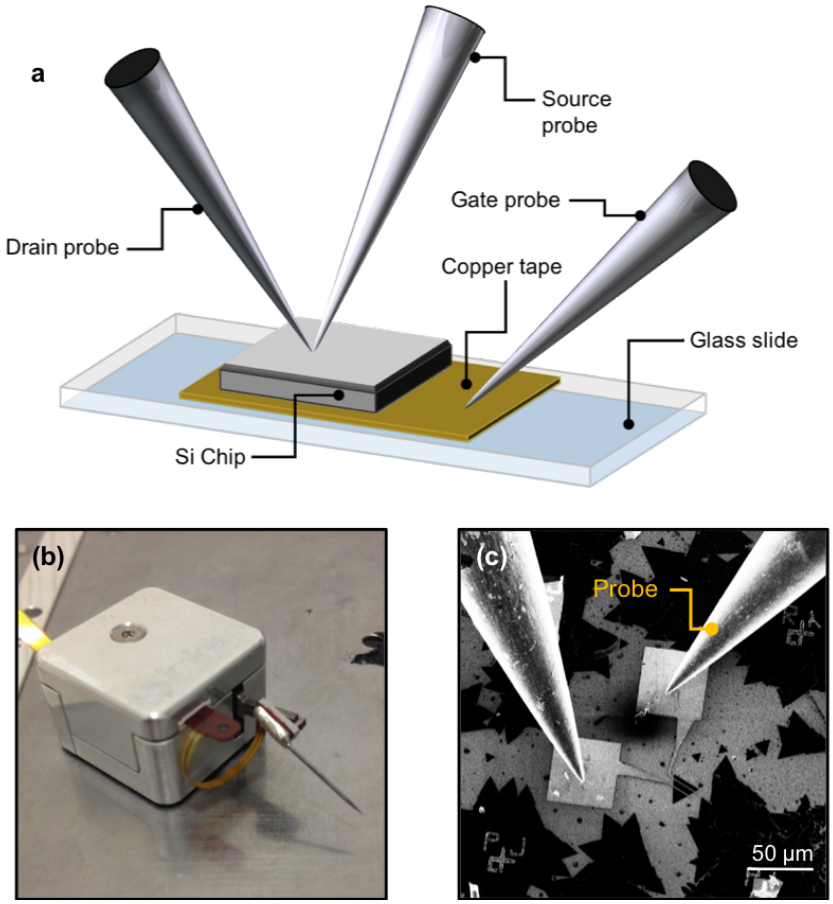

Figure 4.16 | (a) Three-probe configuration for performing electrical characterisation of MoS_2 FET device. (b) Single *Imina Technologies miBot* probe. (c) SEM image of source and drain probes contacted to the device electrode pads.

4.6 References

1. Zhou, W. & Wang, Z. L. *Scanning Microscopy for Nanotechnology: Techniques and Applications* (2006). doi:10.1007/978-0-387-39620-0
2. De Broglie, L. Recherches sur la théorie des quanta. (Migration-université en cours d'affectation, 1924).
3. Freundlich, M. M. Origin of the electron microscope. *Science* **142**, 185–188 (1963).
4. Williams, D. B. & Carter, C. B. *Transmission Electron Microscopy: A Textbook for Materials Science* **30**, (2009).
5. Utke, I., Moshkalev, S. & Russell, P. *Nanofabrication using focused ion and electron beams: principles and applications*. (Oxford University Press, 2012).
6. Wu, H. *et al.* Progress and prospects of aberration-corrected STEM for functional materials. *Ultramicroscopy* **194**, 182–192 (2018).
7. Egerton, R. F. Mechanisms of radiation damage in beam-sensitive specimens, for TEM accelerating voltages between 10 and 300 kV. *Microscopy research and technique* **75**, 1550–1556 (2012).
8. Zhu, D. *et al.* Capture the growth kinetics of CVD growth of two-dimensional MoS_2. *NPJ 2D Materials and Applications* 1–7 (2016). doi:10.1038/s41699-017-0010-x
9. Jeon, J. *et al.* Layer-controlled CVD growth of large-area two-dimensional MoS_2 films. *Nanoscale* **7**, 1688–1695 (2015).
10. Zhan, Y., Liu, Z., Najmaei, S., Ajayan, P. M. & Lou, J. Large-area vapor-phase growth and characterization of MoS_2 atomic layers on a SiO2 substrate. *Small* **8**, 966–971 (2012).
11. Zhou, W. *et al.* Intrinsic structural defects in monolayer molybdenum disulfide. *Nano Letters* **13**, (2013).
12. van der Zande, A. M. *et al.* Grains and grain boundaries in highly crystalline monolayer molybdenum disulphide. *Nature materials* **12**, 554–61 (2013).
13. Komsa, H.-P. & Krasheninnikov, A. V. Engineering the Electronic Properties of Two-Dimensional Transition Metal Dichalcogenides by Introducing Mirror Twin Boundaries. *Advanced Electronic Materials* 1600468 (2017).

doi:10.1002/aelm.201600468

14. Wang, S., Lee, G. Do, Lee, S., Yoon, E. & Warner, J. H. Detailed Atomic Reconstruction of Extended Line Defects in Monolayer MoS_2. *ACS Nano* **10**, (2016).
15. Lin, Z. *et al.* Defect engineering of two-dimensional transition metal dichalcogenides. *2D Materials* **3**, 022002 (2016).
16. Lin, J., Pantelides, S. T. & Zhou, W. Vacancy-Induced Formation and Growth of Inversion Domains in Transition-Metal Dichalcogenide Monolayer. *ACS Nano* **9**, 5189–5197 (2015).
17. Hong, J. *et al.* Exploring atomic defects in molybdenum disulphide monolayers. *Nature Communications* **6**, 6293 (2015).
18. Binnig, G., Quate, C. F. & Gerber, C. Atomic force microscope. *Physical review letters* **56**, 930 (1986).
19. Binnig, G. & Rohrer, H. Scanning tunneling microscopy. *Surface science* **126**, 236–244 (1983).
20. Haugstad, G. *Atomic force microscopy : understanding basic modes and advanced applications*. (John Wiley & Sons, 2012).
21. Wilson, N. R. & Macpherson, J. V. Carbon nanotube tips for atomic force microscopy. *Nature Nanotechnology* **4**, 483 (2009).
22. Giessibl, F. J. Atomic resolution of the silicon (111)-(7x7) surface by atomic force microscopy. *Science* **267**, 68–71 (1995).
23. Dieing, T., Hollricher, O. & Toporski, J. *Confocal Raman Microscopy*. (Springer Series in Optical Sciences, 2011).
24. Raman, C. V. & Krishnan, K. S. A new type of secondary radiation. *Nature* **121**, 501 (1928).
25. Boyle, W. S. & Smith, G. E. Charge coupled semiconductor devices. *Bell System Technical Journal* **49**, 587–593 (1970).
26. Ferraro, J. R. *Introductory raman spectroscopy*. (Elsevier, 2003).
27. Bradley, M. Curve fitting in Raman and IR spectroscopy: basic theory of line shapes and applications. *Thermo Fisher Scientific, Madison, USA, Application Note* **50733**, (2007).

28. Ye, M., Winslow, D., Zhang, D., Pandey, R. & Yap, Y. Recent Advancement on the Optical Properties of Two-Dimensional Molybdenum Disulfide (MoS_2) Thin Films. *Photonics* **2**, 288–307 (2015).
29. Sangwan, V. K. *et al.* Gate-tunable memristive phenomena mediated by grain boundaries in single-layer MoS_2. *Nature Nanotechnology* **10**, 403–406 (2015).
30. Splendiani, A. *et al.* Emerging Photoluminescence in Monolayer MoS_2. *Nano Letters* **10**, 1271–1275 (2010).
31. Kaupmees, R., Komsa, H. P. & Krustok, J. Photoluminescence Study of B-Trions in MoS_2 Monolayers with High Density of Defects. *Physica Status Solidi (B) Basic Research* **1800384**, 3–7 (2018).
32. Li, H. *et al.* Rapid and Reliable Thickness Identification of Two-Dimensional Nanosheets Using Optical Microscopy. *ACS Nano* 10344–10353 (2013). doi:10.1021/nn4047474
33. Simsek, E., Mukherjee, B., Chen, Z. & Gacem, K. Visibility of dichalcogenide nanolayers. *Nanotechnology* (2011). doi:10.1088/0957-4484/22/12/125706
34. Muller, M. R. & Gumprich, A. Visibility of two-dimensional layered materials on various substrates. *Journal of Applied Physics* **145305**, (2017).
35. Ottaviano, L., Palleschi, S., Perrozzi, F. & Olimpio, G. D. Mechanical exfoliation and layer number identification of MoS_2 revisited. *2D Materials* 1–6 (2017).
36. Goldstein, J. *et al.* Scanning Electron Microscopy and X-ray Microanalysis. (2003).

Chapter 5

MoS_2 Memtransistor Fabricated by Local Helium Ion Beam Irradiation

As outlined in chapter 2, novel device paradigms are being sought in order to improve the performance of next generation memory devices. Two dimensional layered materials such as MoS_2 offer distinct advantages over silicon-based components due to enhanced electrostatic control, mechanical flexibility and optical transparency. MoS_2 memory cells based on vertical stacks[1–4] and mechanically-printed lateral devices[5] have been demonstrated in recent years. Single layer polycrystalline MoS_2 films have been shown to exhibit gate-tuneable memristive switching combining the functionality of a memristor and transistor into a single device, called a memtransistor.[6,7] Switching of resistance states in these memtransistors is mediated by the presence of defect rich grain boundaries in the channel which arise during the CVD growth process. However, the downscaling of these devices is ultimately limited by the grain boundary distribution. The density, location and orientation of these grain boundaries is not controllable thus the compatibility with silicon based fabrication processes is limited. The ability to locally modify MoS_2 to induce memristive behaviour with scalable and industry-compatible methods has remained a challenge.

In this chapter the fabrication of a single crystal, monolayer, MoS_2 memtransistor enabled by local irradiation of the channel with a focussed helium ion beam is demonstrated. As discussed in chapter 3 the HIM has emerged as a powerful tool for modifying the structural and electrical properties of 2D materials. Here it is used to introduce a sulfur vacancy rich region, bisecting the channel of a MoS_2 FET. The nature of the damage region is investigated using SEM, TEM, AFM as well as Raman and PL spectroscopic analyses. Electrical characterisation of the modified device reveals stable bipolar resistive

switching, in which the current levels, on/off ratio and set voltage are gate tuneable. Evidence is provided to support the proposed switching mechanism, whereby the field-driven drift of sulfur vacancies sourced from the irradiated region towards one electrode and back, serves to realise the different resistance states. The performance parameters of the device are investigated and exhibit endurance > 600 cycles and a non-volatile retention time > 12 h. Finally, neuromorphic functionality, such as pulse width dependent potentiation and heterosynaptic plasticity on multiterminal devices, is demonstrated.

5.1 Experimental Procedure

CVD MoS_2 sample preparation

Monolayer MoS_2 was prepared by collaborators (C. P. Cullen, N. McEvoy, TCD) via sulfurisation of MoO_3 precursors on marked 285 nm SiO_2/Si chips in a chemical vapour deposition furnace, as has been described in the literature previously[8]. Sulfur powder was heated at 120°C and the resulting vapour carried downstream by Ar gas to a hot zone kept at 750°C. The vapour was flown through a microreactor containing MoO_3 precursor substrates face up with target Si/SiO_2 substrates face down on top of them for 20 minutes. The samples were then annealed in Ar carrier gas at 750°C for 20 minutes after which they were cooled to room temperature.

Mechanically exfoliated MoS_2 sample preparation

Few-layer MoS_2 was prepared by the *Scotch*-tape micromechanical cleavage technique of bulk crystals (*SPI Supplies*) onto marked 285 nm SiO_2/Si chips. Samples were bathed in acetone for 30 minutes to remove tape residue. Layer thickness was identified using optical contrast (*Olympus* optical microscope 50× objective).

Device fabrication

Electrodes were defined by electron beam lithography (*Zeiss Supra* SEM and *Raith Nanopatterning* software), utilising PMMA A3 resist exposed at a dose of 200 μC cm^{-2} followed by development for 45 seconds in MIBK:IPA (1:3). Metal deposition was carried out in an electron beam-evaporator (*Temescal FC-2000*) to deposit Ti/Au (5/35 nm) pads, followed by lift-off in acetone overnight at room temperature.

Helium ion beam irradiation

Helium ion irradiation was performed using a *Zeiss Nanofab* helium ion microscope at a base pressure of ~10^{-7} mbar. Irradiation patterns were designed using the *NanoPatterning and Visualisation Engine (NVPE)* software and consisted of single pixel line scan delivering the dose of ions in a single pass.

The delivered ion dose to induce memristive switching was ~1.6 $\mathrm{pC\ \mu m^{-1}}$ at a beam energy of 30 keV, a beam current of 1 pA and using a 10 μm aperture. This dose was chosen as it is equivalent to a single scanning line from an areal dose of 10^{17} ions cm^{-2} which has been shown to significantly increase the conductivity of MoS_2.[9]

The beam probe size was < 3 nm which was evaluated using the GaussFit module in *ImageJ* software. Briefly, a high magnification image was acquired of a sharp edge near the device, such as the edge of an MoS_2 flake. The intensity profile across the flake edge was plotted using the *ImageJ* software package. The intensity drop across the edge is attributed to the size of the imaging probe. The intensity of the flake is taken as 100% while the surrounding area was taken as 0% intensity. The distance over which the intensity drops from 75% to 25% was taken as the probe size.

Imaging of the device channel was necessary for positioning the line scan but minimised with imaging dose kept to < 10^{11} ions cm^{-2}.

Electrical characterisation

Electrical testing of the devices was performed in the vacuum chamber of a *Zeiss EVO* scanning electron microscope at a base pressure of ~10^{-5} mbar. Devices were left to outgas for > 12 h before testing. *Imina miBot* piezoelectric tungsten probes were used to contact the Ti/Au electrodes which acted as the source and drain. The devices were back-gated with a third probe electrically contacted by copper tape to the underside of the 285 nm SiO_2/Si chip. An *Agilent B2912A* semiconductor parameter analyser using *Keysight* software was used for sourcing voltage and collecting data. Endurance and potentiation measurements were carried out in Peking University by Jakub Jadwiszczak in an *Oxford Instruments* cryostat with no applied magnetic field, pressure of ≈ 10 mbar and temperature of 280 K. The data were obtained using a semiconductor analyser (*Agilent B2912A*) interfaced with *LabVIEW* software.

Raman and PL mapping

Raman and photoluminescence spectroscopic mapping was done in a *WITec Alpha 300R* system in ambient conditions. The device was switched between resistance states *ex-situ* between each map acquisition by sweeping the drain source voltage between 0 V and 35 V (-35 V) 5 times to switch to the LRS (HRS). The excitation wavelength was 532 nm, with a diffraction grating of 1800 grooves mm^{-1} and a 100× objective lens (NA = 0.95, spot size ~ 0.3 μm). The 4 μm^2 areas in Figure 5.11 were scanned in 60 lines at 60 px per line with an integration time of 0.6 s. Mapping was carried out at low incident powers (< 100 μW) to avoid altering the sample with the laser, with the beam refocused manually every time between each scan to ensure an accurate comparison.

Cross-section TEM sample preparation

The cross-sectional lamella was prepared from a bilayer MoS_2 sample by Dr. Pierce Maguire and Clive Dowling. Once irradiated in the HIM, the sample was transferred to a *Zeiss Auriga* focused ion beam system, where a platinum layer was deposited to protect the flake. A gallium beam (30 keV) was used to cut the lamella for lift-out and welding to an Omniprobe grid made of copper. The lamella was then thinned to an electron-transparent width with a 900 eV argon beam (*Fischione 1040 Nanomill*).

Freestanding TEM sample preparation

Freestanding samples were obtained by covering the on-chip MoS_2 samples with PMMA, dissolving the underlying SiO_2 in NaOH at 80°C and transferring onto copper TEM grids; followed by dissolution and washing in acetone/IPA.

TEM imaging

TEM was performed in an *FEI Titan 80-300* microscope operated at a chamber pressure of ~ 10^{-7} mbar. The beam energy used for imaging was 300 keV.

AFM imaging

AFM was performed in ambient using an *Oxford Asylum* atomic force microscope in tapping mode with 140 kHz or 300 kHz cantilevers (Budget Sensors Tap300AL-G).

5.2 Results and Discussion

5.2.1 Device fabrication and helium ion irradiation

Figure 5.1a shows an optical micrograph of a typical device. An equilateral triangular shaped monolayer MoS_2 flake of side length ~25 µm is top contacted by two Ti/Au electrodes spaced 4 µm apart. These electrodes extend to 50 µm × 50 µm pads which can be contacted by tungsten probes for electrical characterisation The area marked with a red square is shown in a SEM image in Figure 5.1b. No grain boundaries are present in the device. Prior to the irradiation the pristine devices display typical n-type MoS_2 FET electrical behaviour, as outlined in chapter 2, with no hysteresis in the I-V curves and can be seen in Figure 5.7

The helium ion irradiation strategy consists of a single pixel line scan with a dose of 1.6 pC μm^{-1} bisecting the channel, i.e. parallel to the electrodes and spanning the whole width of the channel as shown schematically in Figure 5.1c. The irradiation is performed in a single pass with no repeats. At 30 keV the beam has been shown to preferentially introduce sulfur vacancies to the material however at this high dose, damage to the Mo sublattice has also been observed.[9] The probe size is maintained < 3 nm. The damage

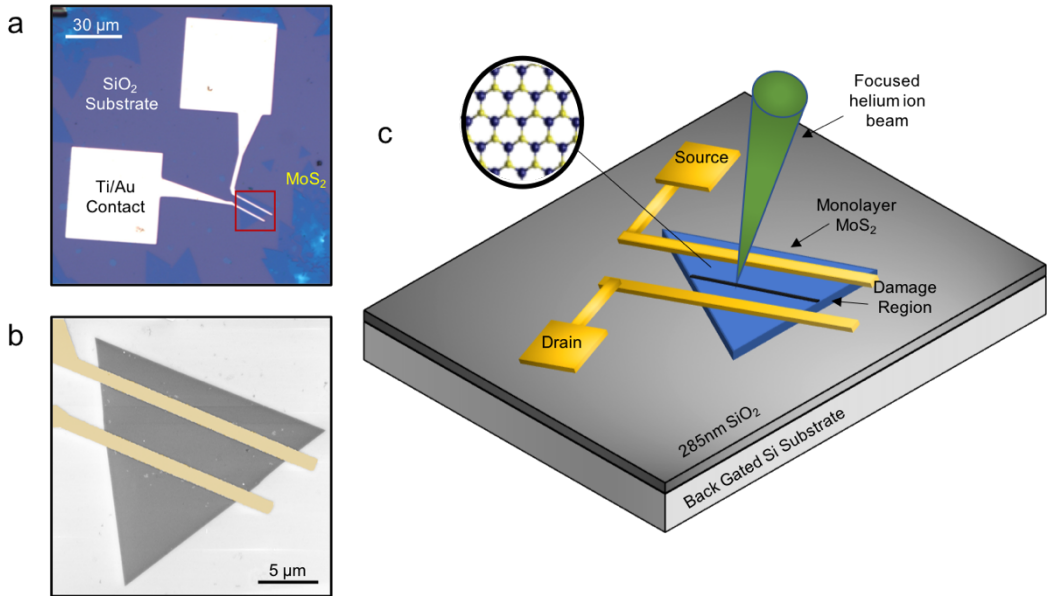

Figure 5.1 | *Device Fabrication*. (a) Optical micrograph of CVD MoS_2 flakes grown on SiO_2 substrate contacted with EBL defined Ti/Au electrodes. (b) SEM image of region marked by red square in (a) showing single domain MoS_2 crystal contacted by two false coloured electrodes. (c) Schematic of device and helium ion beam irradiation strategy.

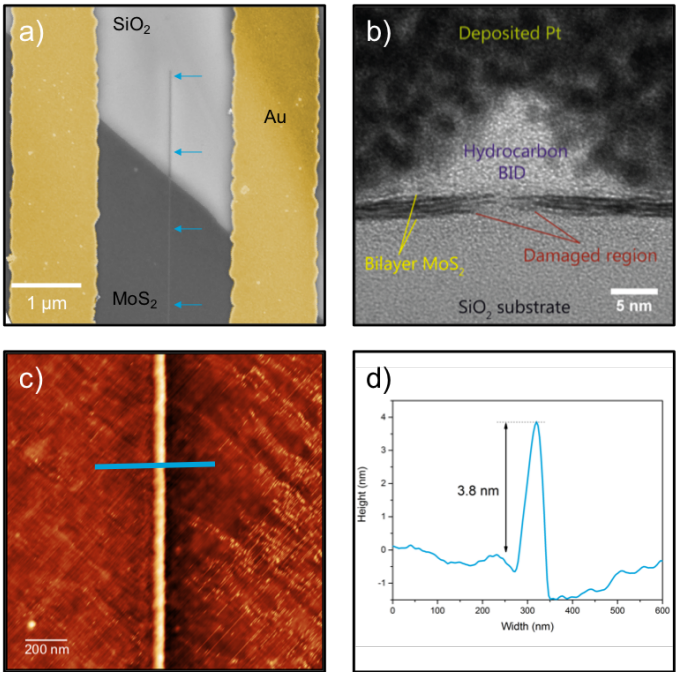

Figure 5.2 | *Characterisation of irradiated region.* (a) SEM micrograph of irradiated device with false coloured electrodes. The helium ion irradiated line runs vertically and is indicated by the blue arrows. (b) TEM cross-section image of irradiated bilayer MoS_2 sample. Hydrocarbon beam induced deposition lies on top of the irradiated line, which was observed to be a defective MoS_2 region spanning ~6 nm. (c) AFM scan of irradiated line on monolayer MoS_2. (d) Height profile take from blue line in (c). Height of BID is ~3.8 nm

region, however, will be extended laterally due to backscattered ions and sputtered substrate atoms.[10]

5.2.2 Characterisation of Irradiated Region

Figure 5.2a shows an SEM image of a device after it has been line irradiated by the helium ion beam. A mound of hydrocarbons formed by beam induced deposition (BID), which locally alters the SE emission yield, can be seen spanning the MoS_2 channel and extending out onto the SiO_2 substrate. A lamella of an irradiated sample was prepared by focussed ion beam (FIB) lift-out and imaged by transmission electron microscope (TEM). The cross-section TEM image is shown in Figure 5.2b showing the MoS_2 flake supported by the SiO_2 substrate. On top of the flake the contamination mound can be seen and above

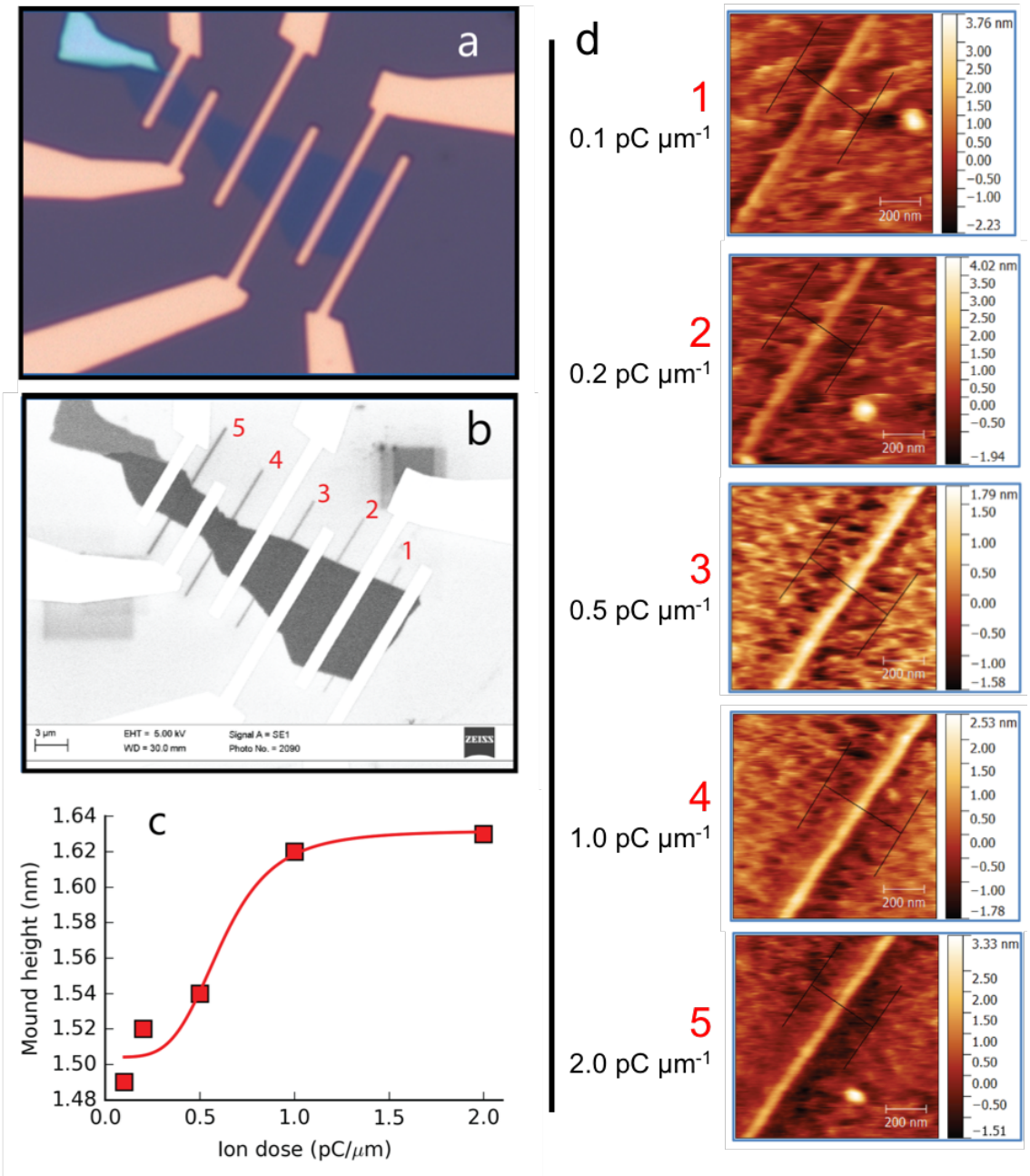

Figure 5.3 | *Dependence of hydrocarbon BID mound on ion dose*. (a,b) Optical and SEM images of monolayer MoS_2 device irradiated at various helium ion doses. The labels 1-5 correspond to the AFM height maps presented below. (c) Extracted heights of BID mounds from line profiles indicated in (a) plotted vs. delivered ion dose. The solid line is a saturated fit scaling as $\propto \frac{1}{1+d^p}$ where d is the dose and p is the fitting exponent.

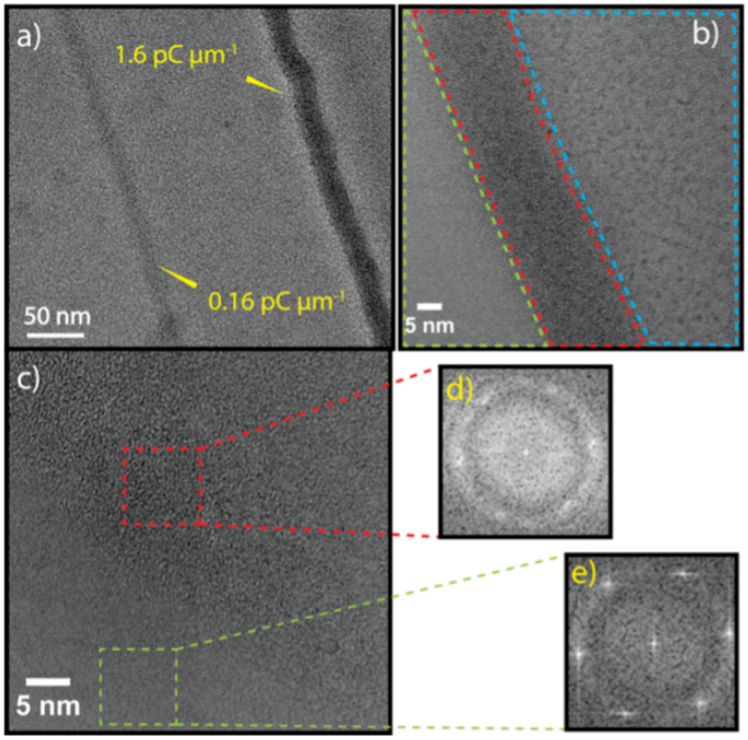

Figure 5.4 | *TEM images of helium ion irradiated suspended MoS_2.* (a) Two HIM line irradiations at doses of 0.16 pC μm^{-1} and 1.6 pC μm^{-1}. Visible contrast difference can be seen between the two doses due to the different levels of BID build-up. (b) Magnified image of 1.6 pC μm^{-1} irradiation which is outlined in red. An asymmetry in the defect level can be observed on either side of the cut, lower outlined in green and higher outlined in red. (d) Magnified image of the interface between the green and red regions. (d,e) Fast Fourier Transforms from the marked regions showing a more crystalline lattice in the unirradiated region.

that the Pt layer used during the lift-out procedure. It should be noted the presence of the hydrocarbon BID obscures the true size of the lattice damage from top view. The MoS_2 lattice damage region extends laterally less than 10 nm. This lateral extension is in agreement with the range estimated by simulation for a 30keV beam.[10] The spatial resolution achieved by the highly-focussed helium ion beam is a critical advantage of this method. It allows site-specific and spatially-controllable defect generation which is compatible with the requirements of large-scale fabrication.

Figure 5.2c shows an AFM height map of the irradiated region. The BID mound height is ~3.8 nm which is shown in the line profile in Figure 5.2d. This BID mound obscures from view the damage to the MoS_2 lattice. The damage region acts as a source of charged

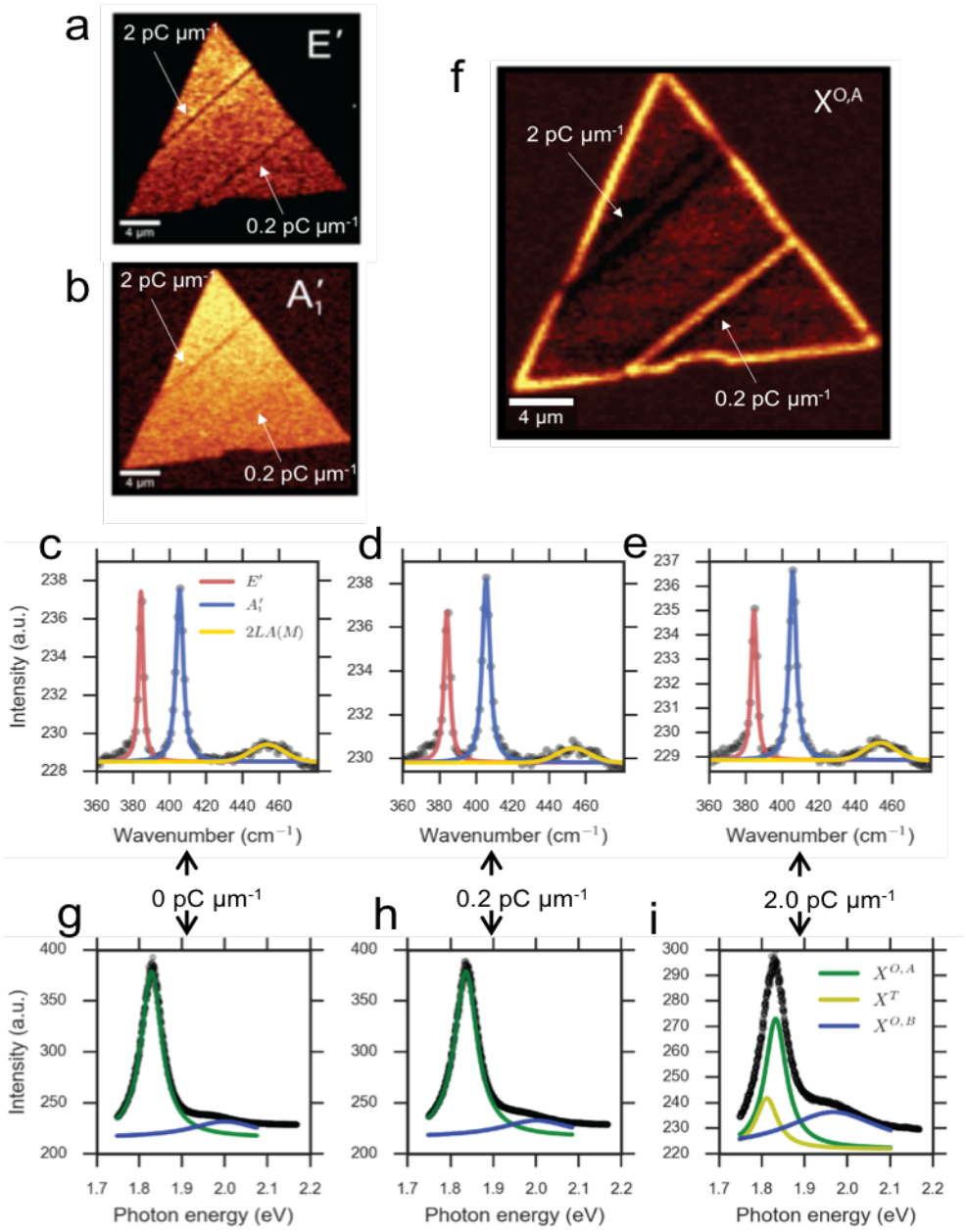

Figure 5.5 | *Raman an PL spectroscopic characterisation of helium ion irradiated MoS_2.* (a,b) Raman maps filtered for the E' and A_1' modes showing the effect of peak shifting and quenching in the ion irradiated regions. (c-e) Spectra extracted from pristine middle region (0 pC µm^{-1}) and the two irradiated regions. No significant peak shifting is observed even at the higher dose of 2 pC µm^{-1}, but the intensity is reduced. (f) PL map of A exciton intensity, showing enhanced emission at the site of the 0.2 pC µm^{-1} (h) due to increased concentration of available donor adsorption sites. At 2 pC µm^{-1} corresponding to the memristor dose, significant quenching compared to (g) and (h) with the emergence of a defect-associated trion peak seen in yellow on the spectrum in (i)

mobile defects. Under electric field they drift and modulate the carrier concentration in the MoS_2 channel which facilitates the memristive switching of the device.

In order to systematically investigate the hydrocarbon BID a monolayer MoS_2 device, shown in Figure 5.2, was irradiated with five different helium ion doses ranging from 0.1 $\mathrm{pC\ \mu m^{-1}}$ to 2 $\mathrm{pC\ \mu m^{-1}}$. The resulting mound heights were extracted by AFM and plotted against ion dose, shown in Figure 5.3c. The absolute value of the height of the deposits will vary from sample to sample due to differing levels of sample contamination as well as differing levels of contamination of the HIM chamber at the time of the irradiation. However a clear dependence of height with dose can be observed.

Free standing MoS_2 samples were prepared by polymer transfer from SiO_2 substrate to a TEM grid. The MoS_2 flake was irradiated with two doses: 0.16 $\mathrm{pC\ \mu m^{-1}}$ and 1.6 $\mathrm{pC\ \mu m^{-1}}$. Figure 5.4a shows a TEM image of the two irradiated regions showing a clear phase contrast difference due to the higher level of hydrocarbon BID for the higher dose. Figure 5.4b shows a magnified image of the 1.6 $\mathrm{pC\ \mu m^{-1}}$ dose. The irradiated region spans ~10 nm laterally and is highly defective.

There is a clear asymmetry in the defectivity of the regions either side of the cut. The integrity of the crystal structure is higher in the region to the left of the cut (marked in green) than to the right (marked in red). This may be due to stigmation of the probe or the sample not lying perfectly flat during the irradiation. This asymmetry may be what causes the preferential migration of defects on one side of the cut as explored in Section 5.2.5. Figure 5.4cshows a magnified image of the interface between the pristine and irradiated region revealing a sharp boundary extending only a few atomic rows. Figure 5.4d,e show Fast Fourier Transform (FFT) taken from the cut and pristine regions respectively, revealing a clearly more crystalline lattice in the adjacent unirradiated region. The material modification of the MoS_2 flake by line irradiation with the helium beam is further investigated by Raman and PL spectroscopic mapping. Figure 5.5a,b show Raman maps filtered for the E' and A_1' peaks which correspond to the in-plane and out of plane vibrational modes respectively.[11,12] The dark lines indicated in the maps correspond to irradiation doses of 2 $\mathrm{pC\ \mu m^{-1}}$ (top line) and 0.2 $\mathrm{pC\ \mu m^{-1}}$ (bottom line). Line-averaged Raman spectra taken from these regions as well as from a pristine region in the centre of

the flake parallel to the cuts are shown in Figure 5.5c-e. Small peak shifting is observed between the irradiated and pristine regions.

The E' peak is red-shifted by 0.2 cm^{-1} for 0.2 pC μm^{-1} and 0.4 cm^{-1} for 2 pC μm^{-1}. The A_1' peak is blue-shifted by 0.1 cm^{-1} for 0.2 pC μm^{-1} and red-shifted by 0.1 cm^{-1} for 2 pC μm^{-1}. No broadening is observed.

The intensity of both peaks is reduced in the irradiated regions however the quenching is stronger for E' than for A_1'. Figure 5.5f shows the PL map of the A-exciton intensity for the same flake. A clear difference can be seen in the emission from the irradiated regions at the two different doses. At 2 pC μm^{-1} the emission is significantly quenched while at 0.2 pC μm^{-1} the emission is enhanced. The associated spectra are shown in Figure 5.5g-i. Reduction in emission intensity is associated with an increase in structural defects which generate mid-gap states that provide non-radiative recombination pathways.[13] Indeed at a dose of 2 pC μm^{-1} peak splitting can be seen, as well as a defect associated trion peak shown in yellow in Figure 5.5i.[14] PL enhancement has been reported due to the accumulation of sulfur vacancies at grain boundaries in CVD MoS_2.[6] These act as adsorption sites for atmospheric molecules which can supress the excitonic radii around defects and passivate the mid-gap states.[15] This would suggest that at the memristive dose of 1.6 pC μm^{-1} the helium ion beam is introducing significant lattice damage which is consistent with the TEM cross-section image in Figure 5.2b. It also suggests that at lower ion doses, like those received by the areas further from the centre of the beam path, sulfur vacancy creation will occur.

It has now been shown that irradiation with the helium ion beam can introduce structural damage to the MoS_2 crystal as well as introduce sulfur vacancies. It is useful to try to estimate the number of vacancies that will be introduced during the fabrication of the memtransistor device. As discussed in chapter 2 the helium ion probe is not spatially uniform but can be modelled as a 2-dimensional gaussian distribution. Also, further spreading of this distribution will occur if the irradiated material is being supported by a substrate.[10] Thus, a single pixel line scan of the beam as used here will be shaped as a series of overlapping gaussian distributions spaced by the chosen pixel spacing.

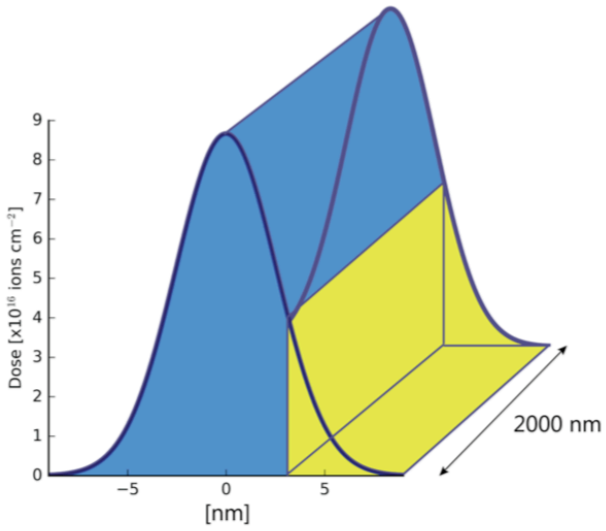

Figure 5.6 | *Plot of simulated dose delivered by helium ion line scan for a linear dose of 1.6 pC* μm^{-1} *with pixel spacing of 1 nm. The FWHM probe size is 6 nm based on the TEM cross-section from Figure5.2b.*

Figure 5.6 shows the simulated resultant helium ion dose distribution for a line of overlapping gaussians with their centres spaced 1 nm apart. Each gaussian contributes 10^4 ions which is what is required to deliver a linear dose of 1.6 pC μm^{-1}. The FWHM of the gaussians is set to 6 nm which is larger than the measured probe size in order to account for substrate broadening and chosen to correspond to the width of the visibly damaged region in the TEM cross-section in Figure 5.2b. If it is assumed that any ions delivered within this width create the heavily damaged region observed therefore they effectively do not contribute to the creation of any mobile V_s species. The yellow region marks the distribution of ions (for one side of the cut) capable of contributing to the sputtering of sulfur atoms which create mobile vacancies. The integrated areal dose in the yellow portion of the curve was calculated to be 6.4×10^{16} ions cm^{-2}. At 30 keV the sputter yield[16] of S per helium ion is ≈ 0.007, the higher bound for V_s concentration sourced from one side of the cut is then 4.2×10^{14} V_s cm^{-2}.

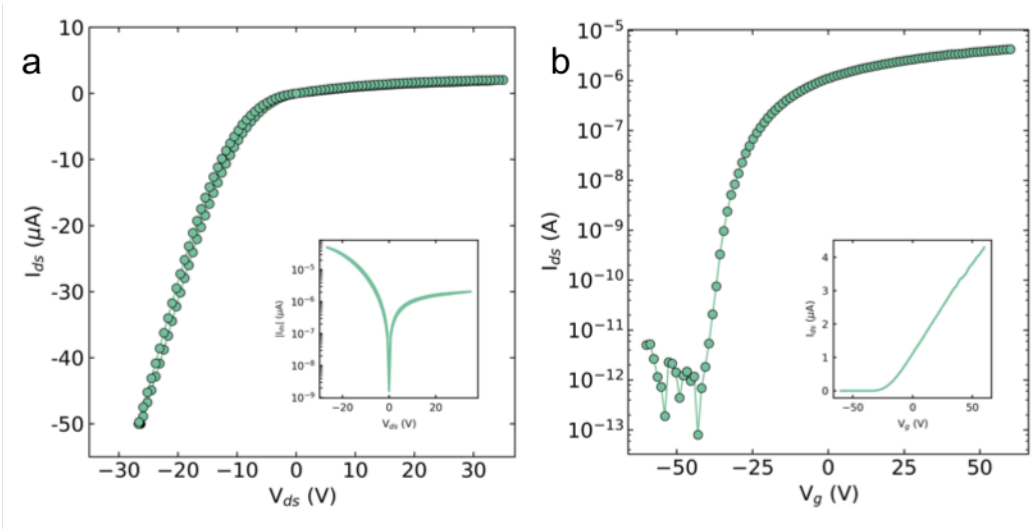

Figure 5.7 | *Electrical behaviour of unirradiated device.* (a) I-V curve of typical CVD MoS_2 device pre-irradiation, V_g = 0 V . Inset: Same plot on semilog scale. Note no significant hysteresis in the output curve. (b) Gate transfer curve of same device, V_{ds} = 1 V. Inset: Same plot on linear scale. Transfer curve show typical MoS_2 n-type FET behaviour.

5.2.3 Electrical characterisation

The device as fabricated before irradiation with the helium ion beam is structured as a standard backgated MoS_2 field effect transistor (FET), as described in chapter 2. The output curve, measured by applying a voltage across the top contacted source and drain electrodes, is shown in Figure 5.7a. The voltage is swept from 0 V to 35 V back through 0 V to -35 V and then finally back to 0 V. The forward and backward trace are well overlaid with no significant hysteresis. The transfer curve in Figure 5.7b shows the typical n-type electrical conductance of MoS_2 FETs. The extracted field effect mobility is 2.7 $cm^2\ V^{-1}\ s^{-1}$.

It has been shown that irradiation of the channel with the helium ion beam creates a confined damage region of defective MoS_2. After irradiation, significant hysteresis opens up in the output curve of the device, shown in Figure 5.8a. The device begins in a high resistance state (HRS). As the drain source bias V_{ds} is swept up from 0 V to 35 V (red trace), a sudden non-linear increase is observed as the device switches into the low resistance state (LRS). The device remains in LRS as the voltage is swept back to 0 V and the polarity is reversed (blue trace). During the negative bias sweep the device is reset back from LRS to HRS which persists as the device is swept back to 0 V.

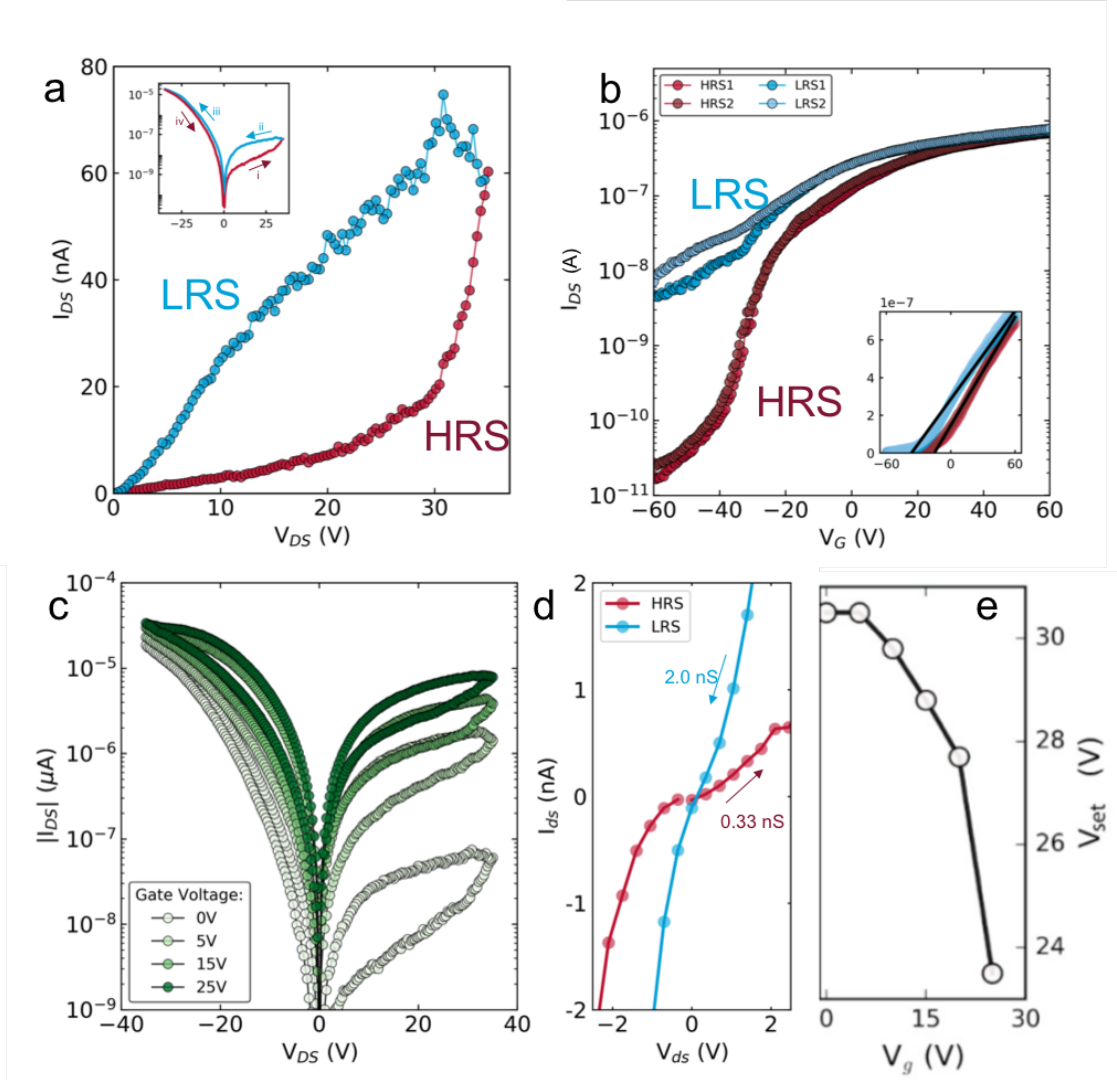

Figure 5.8 | *Gate tuneable resistive switching.* (a) Positive bias sweep of irradiated device at $V_g = 0$ V. Inset: Semi-log plot of I-V sweep over entire bias range with labelled sweep directions. As the voltage is swept to 35V a sharp non-linearity marks the set point from the high resistance state (HRS) to the low resistance state (LRS). The device remains in the LRS as the polarity is reversed and switches back to HRS during the sweep to -35V. (b) Transfer curves of the memtransistor after the device is switched alternately into the LRS (blue curves) and HRS (red curves). Inset: Same plot on linear scale. Straight lines fitted to linear portion of curves in each state to extract gate threshold voltages, V_{th}. (c) Semi-log plot of full I-V sweeps of the device at different gate biases. (d) Magnified plot of the zero-bias pinch-off region of I-V curve in (a) The conductance of both states extracted from straight line fits near 0V marked. (e) Set bias modulation with gate bias. Increasing positive gate field enables earlier onset of resistive switching.

This pinched hysteresis loop is the 'fingerprint' of memristive devices as outlined in chapter 2. The requirement to reverse the bias polarity in order to reset the device is characteristic of bipolar resistive switching.

As outlined, a key difference between these planar memtransistor devices and conventional memristor devices is the ability to tune the conductance by an applied gate field. This is not only beneficial for enabling novel functionality but can be used to more deeply investigate their electrical behaviour. The gate field is applied through the back-gate oxide. The gate transfer curves in LRS and HRS are shown in Figure 5.8b. The device was alternately switched between states and a gate sweep performed after each switching half-cycle.

A marked shifting of the gate threshold voltage (V_{th}) between states, from -19 V in HRS to -37 V in LRS is observed. The V_{th} remains stable within states. This shifting of threshold voltage is not the same as the transfer curve hysteresis observed in MoS_2 transistors which is caused by charge trap/detrapping.[17,18] High output current levels in LRS at V_g = -60 V indicates surplus donors in the channel. No major change in mobility at V_g = 0 V is observed between states (0.14 $cm^2 V^{-1} s^{-1}$ and 0.16 $cm^2 V^{-1} s^{-1}$ in HRS and LRS respectively), despite a ten-fold increase difference in conductivity. This would indicate a fundamentally similar transfer mechanism in both states, with the major difference between states being the level of available donors in the channel. The difference in carrier density is calculated to be ~1.6×10^{12} cm^{-2} from equation 2.6 in chapter 2. This is well within the amount of potential mobile donors generated by the helium ion beam estimated in the previous section.

Figure 5.8c shows I-V sweeps of the device on a semilog scale at different positive gate biases. The size of the hysteresis loop and the overall output current is modulated by the gate field. Figure 5.8d shows a magnified plot of the zero-bias pinch-off region of the I-V. The resistance states are well distinguished as the device is swept to 0 V with conductances of 2 nS and 0.33 nS in the LRS and HRS respectively. The pinch-off at 0 V shows that no energy is being stored by the device, a key feature of memristors differentiating it from the hysteresis seen in capacitive devices. Figure 5.8e plots the set voltage (defined as the bias at which the sharp nonlinearity emerges in the I-V) versus

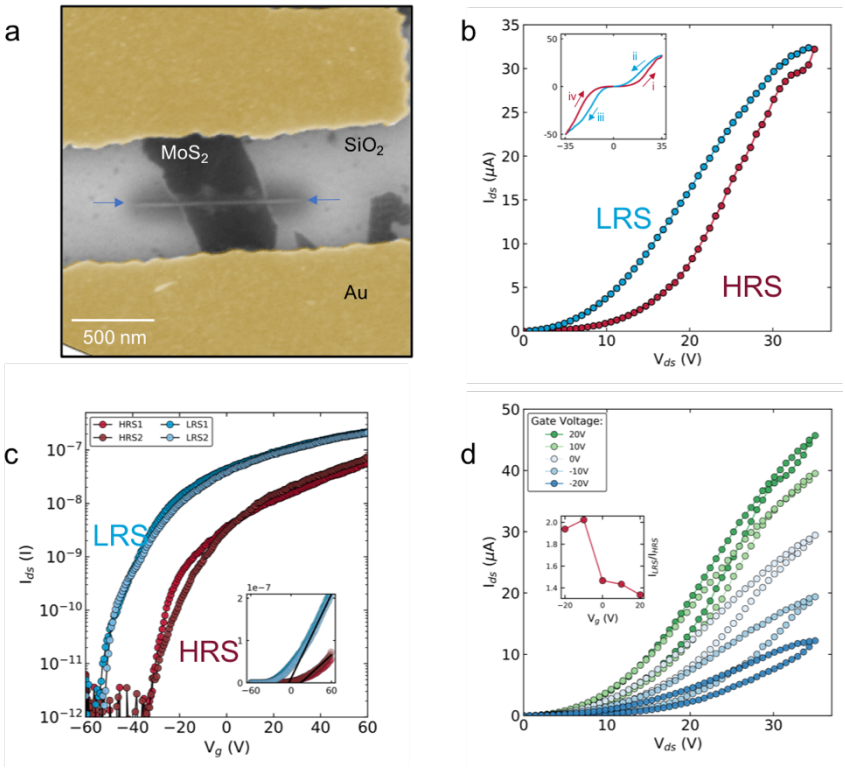

Figure 5.9 | *Bilayer MoS_2 memtransistor*. (a) False colour SEM image of mechanically exfoliated bilayer MoS_2 flake contacted with two Ti/Au electrodes. Region irradiated with HIM marked with blue arrows showing visible BID. (a) Positive bias sweep of device showing the switch from HRS to LRS. Inset: Full range of I-V sweep with labelled seep directions showing bipolar resistive switching. (c) Gate transfer curves measured alternately in HRS and LRS. Inset: Same plot on linear scale with fits to linear portion of curves in black extending to V_{th}. (d) Positive region of gate modulated I-V sweeps for the same device. Inset: Modulation of on/off ratio with gate bias.

gate bias. Increasing gate fields reduces the drain source bias necessary to switch from HRS to LRS.

To demonstrate the effectiveness of the helium ion beam in inducing resistive switching in layered materials, the effect was reproduced in mechanically exfoliated bilayer and few-layer MoS_2. Figure 5.9a shows a false colour SEM of fabricated bilayer device. As with the CVD grown monolayer samples a mound of BID is visible in the region irradiated by the beam. Figure 5.9b shows the drain source I-V sweep for the device, switching from HRS to LRS as the device is swept up to 35 V and exhibiting bipolar switching behaviour requiring reversal of the voltage polarity to switch reset the device

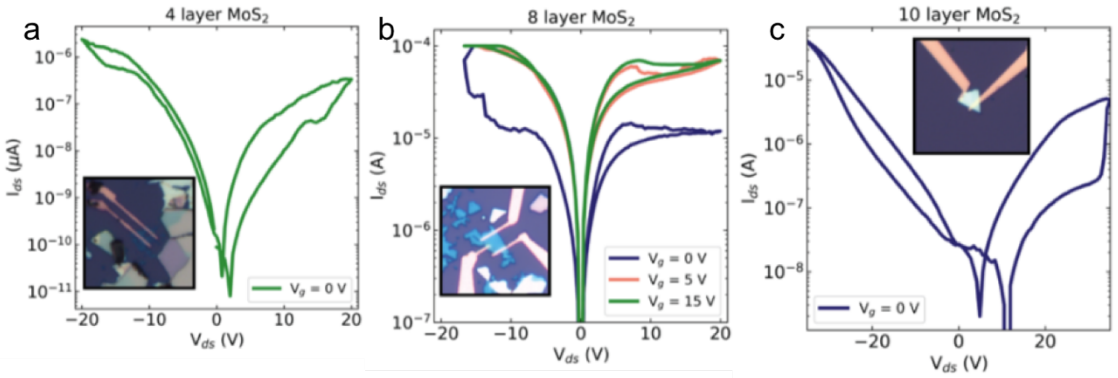

Figure 5.10 | Resistive switching of mechanically exfoliated MoS_2 devices of different layer thicknesses: (a) 4-layer (b) 8-layer and (c) 10-layer. Each irradiated at a $He^{=}$ dose of ~ 1.6 pC μm^{-1}, demonstrating the generalisability of this technique to MoS_2 flakes of larger layer thickness. Insets show optical image of each device.

to HRS. The gate transfer curve shown in Figure 5.9c shows a clear shift in the threshold voltage in the different resistance states. V_{th} = 15.4 V and V_{th} = -4.7 V in HRS and LRS respectively, indicating an increase in carrier density in LRS. Figure 5.9d shows the modulation of the I-V hysteresis curves with gate voltage. The inset figure plots the current ratio in both state as a function of gate voltage, showing that the on/off ratio is controllable by the applied gate field.

Figure 5.10 shows this methodology applied to thicker mechanically exfoliated MoS_2 devices (4, 8, and 10 -layer samples). Similar gate-tuneable resistive switching can be observed however, a systematic investigation into the interaction of thickness and switching behaviour is to be carried out in future work.

5.2.4 Visualising defect drift by Raman and PL spectroscopy mapping.

Figure 5.11 shows the Raman and photoluminescence (PL) spectroscopy mapping of a contacted CVD monolayer MoS_2 memtransistor. The channel length of the device is ≈ 1 μm, extending from 0.5 μm to 1.5 μm on the x-axes in the figures. Raman and PL maps were collected in each resistance state. Note that this device was mapped and electrically switched in ambient conditions. To visualise the mapping results, the E′ Raman mode at 386 cm^{-1} was summed over a spectral window of ± 5 cm^{-1} on either side of the peak. The fractional intensity of the B exciton, B/(A+B), was obtained from the B and A peaks at 2.01 eV and 1.89 eV respectively and was summed over a spectral window of 0.1 eV. Figure 5.11a,b show line profile intensities of the E′ Raman mode averaged across the device channel, alternating between LRS (a) and HRS (b). The source and drain electrodes are shown in gold on either side of the MoS_2 channel, with the red arrows indicating direction of mobile defect drift under the applied bias. The drain and source sides of the device are indicated and are separated by a helium ion created damage region of the standard dose of 1.6 $pC\ \mu m^{-1}$. The location of the irradiated region is indicated by the black dashed lines. In LRS, the spatial distribution of the Raman intensity on either side of the black line is roughly equal, as represented by the uniform blue colour in (c). The red areas represent low signal regions from the MoS_2 hidden by the electrodes. In HRS (d), the intensity is observed to drop off strongly on the drain side and is distributed non-uniformly in the material. Figure 5.11e-h show analogous PL profiles and maps of the fractional B intensity. The purple regions indicate areas where contributions from the B exciton are strongest. The emission on the source side changes significantly by switching from LRS to HRS, while the drain side emission declines in intensity; with particular quenching of the B exciton (factor of ∼7) in the PL maps. The spatial uniformity of the emission on both sides of the cut is disrupted in HRS, with most of the signal from the top and bottom regions of the channel quenching drastically between states.

No significant shifts or broadening of the E′ and A'_1 Raman peaks on the drain- side is observed, despite a large drop in intensity. The separation of the in-plane E′ (386 cm^{-1}) and out- of-plane A'_1 (405 cm^{-1}) first-order modes is ∼20 cm^{-1}, consistent with single-layer MoS_2[11] when switching between states, maintaining good integrity of the crystal

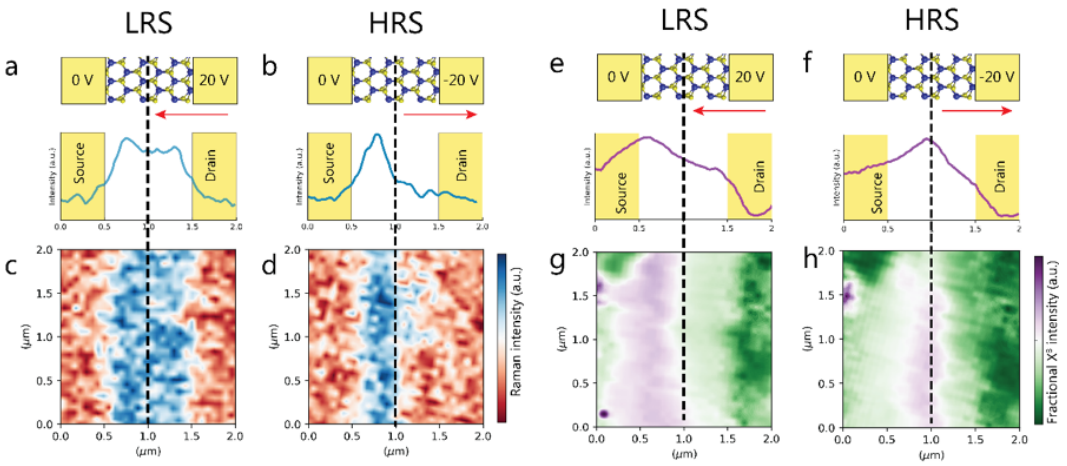

Figure 5.11 | *Raman and PL spectroscopic characterisation of device in different resistance states.* (a,b) Line profiles of Raman intensities across the helium ion cut. Red arrow marks the direction of dopant drift when the applied bias is as indicated on electrodes on schematic above. (c,d) Spatially resolved Raman intensity maps of the E' mode, normalised to colour bar on the right. (e-h) Analogous B/(A+B) exciton photoluminescence data from the same device. PL data also shows a significant drop in intensity on the drain-side of the damage region (marked with the blacked dashed line) after switching into HRS.

structure. The drop in Raman intensity suggests a large decrease in electron-phonon coupling as defects migrate from the fissure region into the unirradiated lattice. PL emission from the direct-recombination A exciton and spin-orbit split B exciton is centred at 1.89 eV and 2.01 eV respectively throughout the switching with no shifts. This range is usually reported for typical monolayer MoS_2[19,20] also confirming the relative structural integrity of the material in both LRS and HRS.

Based on this data, it is proposed that when switching the device into LRS, the defects migrate towards the source electrode from the irradiated region. Their depletion from the drain-side of the channel attenuates B exciton intensity which is usually associated with defect concentration.[19,21] Helium ion irradiation above doses of 1 pC μm^{-1} results in V_S concentrations[9] induced by beam sputtering that far exceed sub-stoichiometries achieved naturally by CVD growth.[13] As sulfur vacancies are defects with the lowest formation energy in MoS_2[22], are stable on substrates when charged[23], and also have a lowered energy barrier for diffusion when in clusters[24,25] and when charged[26], it is likely that they are the majority species responsible for resistance switching in these devices. However,

computational works have challenged the role of V_S in donating electrons to the MoS_2 lattice[22,27] so Mo interstitials or antisite defects, inevitably introduced by the helium beam, cannot be ruled out as also contributing to the mechanism. Note that a downshift of E′ is expected if the V_S concentration is higher than 1%.[28] As the difference in V_S concentration between LRS and HRS as calculated from the shift in the gate curves (Figure 5.8b) in this case is less than 1%, no peak shifts in the Raman spectra are detected. The physico-chemical process occurring at the MoS_2/contact interface[7] effectively strips V_S of their ability to donate free charge to the FET channel in HRS. The optical properties of the source-side of the device in this experiment were not affected as defects from the source-side are not able to readily pass the beam-created barrier in this monolayer device, forming an asymmetric material structure necessary to achieve bipolar resistive switching. The spectroscopic observations are in line with transfer curves obtained in HRS and LRS (Figure 5.8b), showing a reduced degree of n-type doping in HRS, as donor defects are depleted at the drain electrode interface.

The asymmetry observed in the Raman and PL maps suggests that the cause of the bipolar switching is the asymmetric distribution of vacancies, either introduced by the helium ion beam or induced by the initial I-V sweep. To test this, a purposefully skewed distribution of defects was delivered to the device by tilting the microscope stage during the helium ion irradiation. Two channels were fabricated on the same monolayer MoS_2 fake and the stage was tilted by 15° for the irradiation. The source and drain electrodes were then exchanged when sweeping the I-V curves on the two channels, inverting the electric field direction relative to the skewed V_S distribution. This forces vacancies on the preferentially defect-rich side to migrate away from the barrier in one channel, and across the barrier in the other channel.

Figure 5.12a,b show the initial I-V sweeps of the asymmetric devices with the source electrode tilted away and towards the helium ion beam respectively. Insets are PL intensity maps of the B exciton around the barrier (marked in the map as a red line) taken in HRS and LRS for each device. As can be seen from the relative magnitude of the red and blue sweep portions on both plots, the resistance state initially obtained by each device from the beam depends on the direction of bias relative to the asymmetric vacancy distribution introduced by the tilted irradiation.

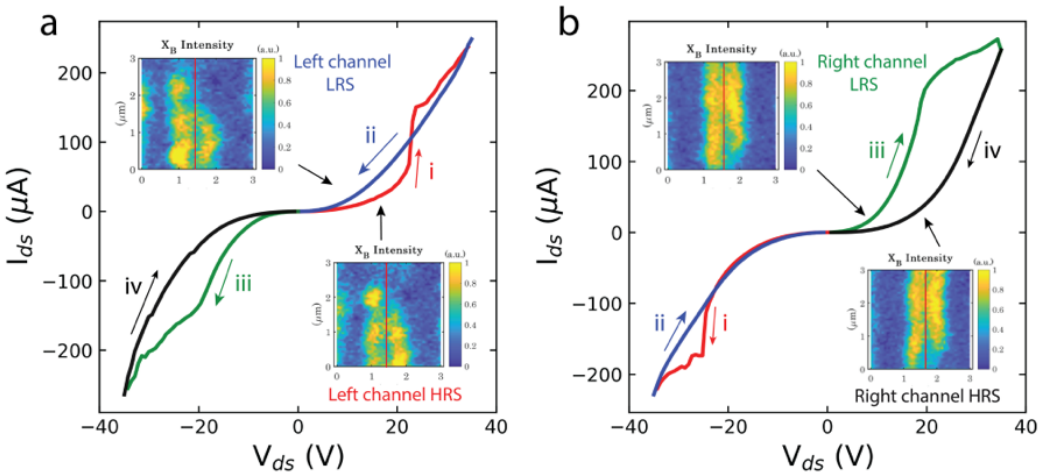

Figure 5.12 | *Effects of asymmetric irradiation on initial resistance state setting.* (a) Left channel had the source electrode tilted 15° away from the incident helium ion beam. In this case the memtransistor is initiated into HRS (red trace, i). PL maps of the device in LRS and HRS are included in the insets, showing a clear asymmetry in the recorded signal across the ion-created barrier. (b) Right channel had the source electrode tilted 15° towards the beam. In this case the helium ion irradiation initiates the device into the LRS for the first sweep (red trace, i). PL maps show a more symmetric defect distribution after biasing, suggesting that the asymmetric vacancy arrangement introduced by the tilted irradiation is the dominant variable for device functionality over the initial sweep polarity. The blue areas on the PL maps are the device electrodes which obscure the MoS_2 signal.

The PL maps of the left channel device exhibit intensity variations on both sides of the cut in the two resistance states which suggests a more prominent defect migration in this device, i.e. the skewed V_S distribution is closer to the active electrode. In the right channel PL maps, the asymmetry between the resistance states is not as pronounced, implying that vacancies cannot pass as readily through the barrier towards the active electrode. Hence, we observe the flip for LRS to HRS as the bias is increased and more vacancies are forced into the cut region. Both channels retain similar levels of current, set biases and resistance ratios despite the differing switching dynamics. Thus, we propose that the bipolar nature of the resistive switching is dependent on the initial V_S distribution introduced by the beam and it is the cut region which ultimately governs the switching behaviour of the device.

5.2.4 Evaluating the device performance

In order to fully assess the potential of our fabricated memtransistor devices, performance indicators along several axes must be evaluated. This will enable us to ascertain where our devices have a comparative advantage over other memristor devices and to identify where further improvements must be made. The device endurance was evaluated through repeated I-V cycling between ± 20 V, switching it between HRS and LRS, at various sweep frequencies. For this device the switching was performed in the sub-threshold regime (V_g = 5 V) and the state current levels were read at V_{ds} = 4 V. Figure 5.13a shows a plot of the current levels in each state (blue and red points) and the current ratio (I_{LRS}/I_{HRS}) (black points) vs. cycle count. The device exhibits an endurance > 616 cycles. The plot is also delineated by ramping speed (s_r) with each coloured region indicating the s_r at which the voltage bias was swept. The HRS and LRS currents exhibit negligible temporal variation between cycles when tested in the optimal s_r range of 2.1-2.9 V s^{-1}. Sub-optimal frequencies on either side of this range overdamp/underdamp the ionic drift process resulting in loss of stability or no switching of resistance at all. Figure 5.13b plots the distribution of the current ratio across these 616 cycles, with most recorded values between 5 and 10. Set bias stability was evaluated over 100 consecutive cycles at s_r = 2.32 V s^{-1} and its distribution is plotted in Figure 5.13c. The set bias is extracted from a reached current threshold. The value oscillates for the initial 20 cycles but settles to a steady state and is stabilised by subsequent cycling. The V_{set} standard deviation is ± 0.41 V on a ± 20 V sweep range.

The device-to-device variability is examined in Figure 5.13d. Shown is a histogram of the set and reset voltages recorded from 16 different monolayer CVD memtransistor devices. A distribution of values is to be expected due to channel non-uniformity and different intrinsic level of defects present from different crystal growths.

A key feature of memristor devices is the possession of non-volatile memory i.e. the ability to retain their resistance state when the power is switched off. Figure 5.14a shows the state retention characteristics for a monolayer memtransistor device. The current level in each state is read with a constant read voltage and plotted versus time. The device was measured first in HRS then immediately after switching to LRS. The power was removed

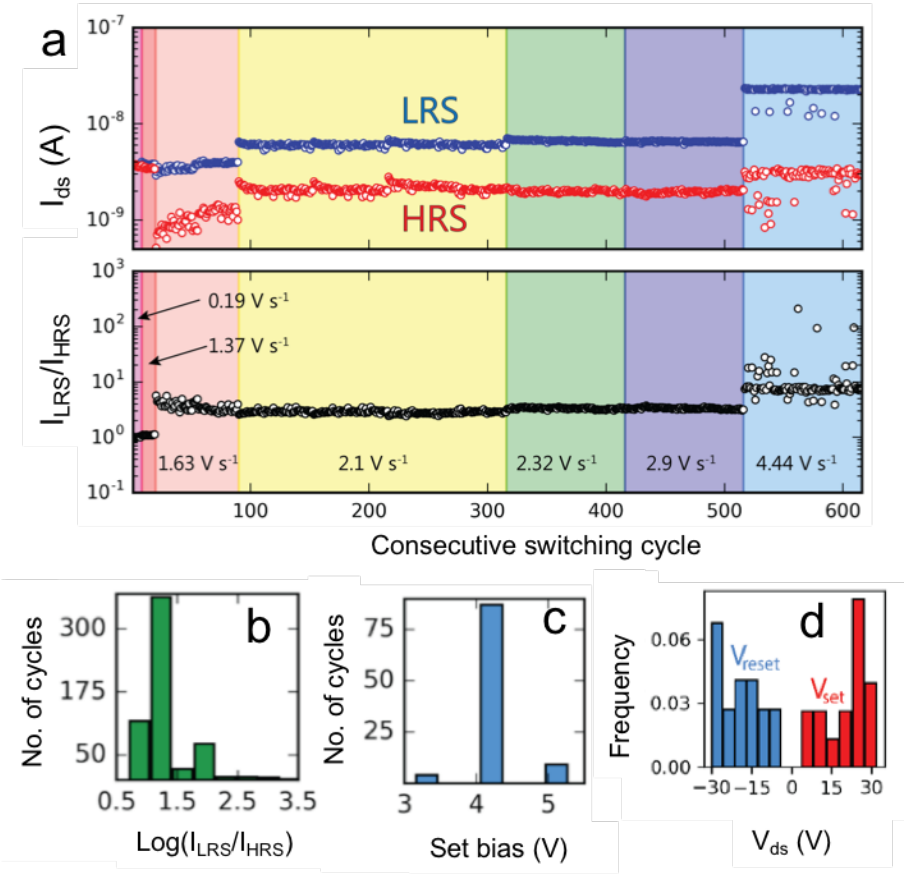

Figure 5.13 | *Switching performance of memtransistor device.* (a) Current endurance (top) and resistance ratio (bottom) of states read at V_{ds} = 4 V and V_g = 5 V across 616 switching cycles. Each coloured portion corresponds to the labelled ramping speed employed for that set of cycles. (b) Histogram showing the log-transformed distribution of resistance ratios from (a). (c) V_{set} distribution over 100 sweeps at s_r = 2.32 V s^{-1}. (d) Histogram of V_{set} and V_{reset} values recorded for 16 monolayer CVD memtransistor devices at V_g = 0 V.

for 1 hour and then the current measured again in LRS. The variability in current level is less than 1.5% after 1 hour.

The same procedure was carried out for a bilayer device shown in Figure 5.14b. This time however the current was measured again in LRS after 15 hours with the power supply removed. The bilayer device was then switched back to HRS and the current was immediately measured. The variability in LRS after 1 h is ~ 1.5% and 8% after 15 hours. It should be noted that the current level in LRS is actually higher after 15 hours with this variance reflecting some instability within states rather than a decay over time, suggesting that the retention could be well over 15 hours.

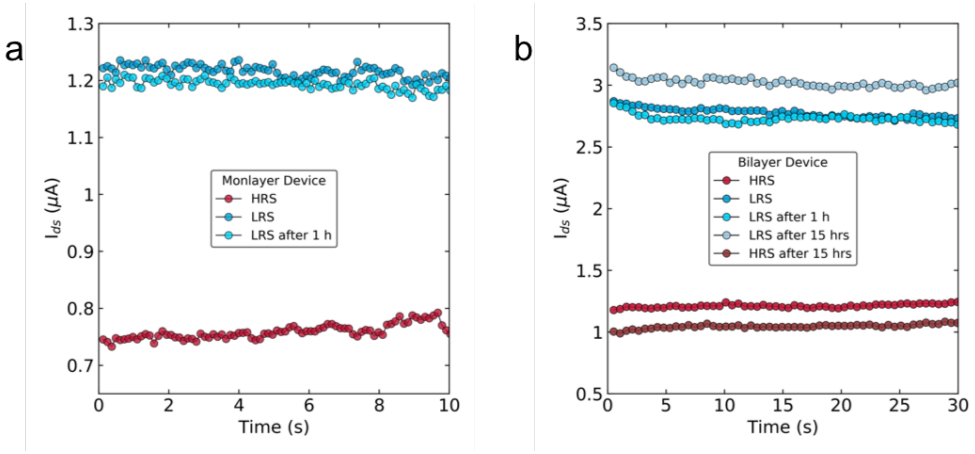

Figure 5.14 | *Retention time.* (a) Current readout in HRS and LRS of monolayer device. Device was first measured in HRS then immediately after switching to LRS and again 1 h after cutting the power supply. (b) Current read out for bilayer device. First measured in HRS then immediately after switching to LRS. Current measured again 1h and 15 hrs after cutting the power supply before being switched back to HRS and measured a final time. Read voltage of 10 V used in all cases.

Table 5.1 summarises the performance parameters of relevant MoS_2 memristors recently published in the literature and compares them to this work. It is evident that device geometry plays a large role in determining the required set voltage, with planar devices showing a range of 3.5 V to 80 V (this work demonstrating 35 V). Vertical devices, however, require lower set voltages with a range of 66 mV to 3.5 V. The power consumption in standby mode ($P = I_{HRS} \times V_{read}$) of 16 nW is comparable with the planar polycrystalline MoS_2 devices, and compares favourably to the printed multilayer MoS_2 devices (mW range). These parameters could be improved by optimisations such as reducing the channel length. The key advantage of this work over the polycrystalline devices is that the small lateral extension of the helium ion induced defective region is much more conducive to downscaling than grain boundary rich channels. In fact, with further reduction of the channel length we should approach the ballistic transport regime of MoS_2 which would greatly reduce the power losses and operating voltage range.[29]
The endurance demonstrated by our device is higher than that for any of the other planar devices (>616 switching cycles compared to 475 cycles for the next highest device). The ON/OFF ratio our device appears limited compared others (10 vs. 10^4), however this ratio has been shown to be sufficient for use in some scaled-up neuromorphic architectures.[30]

REFERENCE	SUMMARY	GEOMETRY	V_{SET}	ON/OFF RATIO	RETENTION	ENDURANCE	SWITCHING TIME	POWER CONSUMPTION
This Work	HIM fabricated	Planar	35 V	~ 10	> 1 hr	> 616 Cycles	> 0.1 s	~ 16 nW
1	1L TMD between Cr/Au electrodes	Vertical	1 V	$> 10^4$	> 1 week	150 cycles	1 s	~ 10 nW
2	Stacked graphene/ $MoS_{2-x}O_x$/ graphene	Vertical	3.5 V	~ 10	> 1 week	$> 10^7$ cycles	100 ns	> 1 pW
5	Mechanically printed 15nm MoS_2 with Ti/Au electrodes	Planar	15 V	< 10	> 30 s	> 5 cycles	2 ms	< 0.05 W
7	Polycrystalline large area monolayer CVD films with Ti/Au electrodes	Planar	80 V	~ 100	24 hours	475 cycles	1 ms	50 pW – 1 mW
31	(92% 1T) MoS_2 sandwiched between Ag electrodes	Vertical	66 mV	$\sim 10^4$	N/A	1000 cycles	N/A	0.1 mW
6	CVD Monolayer MoS_2 with individual grain boundary	Planar	3.5 V – 8.4 V	10^4	N/A	15 cycles	N/A	> 1 µ W
32	1L MoS_2 between Cr/Au electrodes	Vertical	1 V	10^4	$> 10^4$ s	20 cycles	< 30ns	< 1 µ W
4	Annealed MoS_2/MoO_x matrix between Ag electrodes	Vertical	150mV	10^4	$> 10^4$ s	> 1000 cycles	5 ms	< 1 µ W

Table 5.1 | Summary of various device parameters from relevant MoS_2 memristive devices from literature. This work is highlighted in blue.

5.2.5 MoS_2 memtransistors as multiterminal synaptic devices

The success of two-dimensional materials for future neuromorphic applications will depend on their ability to mimic synaptic processes with good accuracy. Training pulses which simulate neuronal input signals were used to demonstrate the neuromorphic capabilities of the device. Consecutive pulses of long-term potentiation (LTP) and depression (LTD) were recorded, shown in Figure 5.15a, by stressing the device into HRS or LRS respectively with a train of 16 evenly-spaced action potential pulses. The post-excitation current was read out at V_{ds} = 6 V following each pulse and is well fitted with a sharp exponential rise/decay function, shown in Figure 5.15b. The memtransistor was back-gated at V_g = 5 V throughout this testing. Note that the lowest power consumption (disregarding gating) in standby is $P = I_{HRS} \times V_{read}$ = 16 nW, which compares favourably with the polycrystalline films and multi-layer devices (15 μW and 0.1 μW in HRS respectively[5,6]). With optimisations such as reduced channel lengths and contact area, our devices should start approaching sub-pW levels demonstrated by some vertically stacked 2D devices.[32]

As demonstrated recently by Sangwan et. al.[7], planar memtransistors enable emulation of heterosynaptic plasticity through the seamless incorporation of multi-terminal architectures. Figure 5.15c shows low-bias I-V traces measured between electrodes 3 and 4 of the device in the inset image. By electrically stressing the He^+ irradiated region (between contacts 1 and 2), defects can migrate between the cut region and electrode 2. This modulates the conductance of the MoS_2 channel between perpendicular terminals 3 and 4. This also directly demonstrates that the resistance of the channel is a function of mobile defect concentration. The output current of the 3-4 junction is modulated only by stressing the 1-2 junction, even below its V_{set}.

The logic and switching applications of any memristive device will ultimately be limited by the speed at which states can be accessed and read out. Functionalities such as pattern recognition rely on effective thresholding of output currents[33] and the smearing of state resistances at high switching frequencies will lower the tolerance required for multi-level operations.[34] Our devices maintain state distinguishability above switching rates of 10 Hz on a 8.5 μm channel containing a single sub-10 nm He^+ cut.

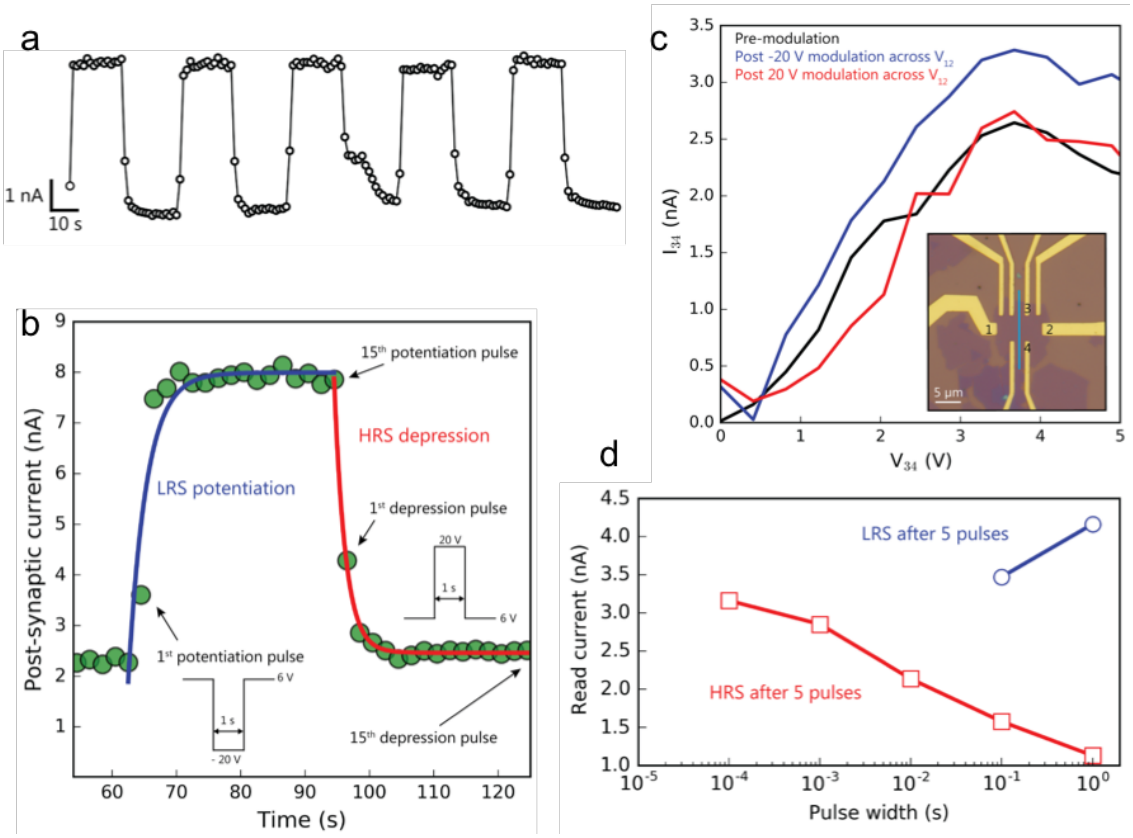

Figure 5.15 | (a) Plot of post-synaptic current recorded during 5 sequential LTP/LTD training cycles. Trains of 16 pulses were applied passed the reset voltage into LRS and set voltage into HRS. (b) Magnified plot of the second potentiation/depression cycle from (a). The rise and decay are fitted with exponentials and habituate to saturated resistance values in each state within <5 pulses. (c) Cross terminal modulation of resistance by lateral drift of defects sourced from the irradiated region. Inset: Optical image of device with labelled terminals and irradiated region marked in blue. (d) State current levels as a function of width of pre-synaptic learning pulses. Timescales below 0.1 s inhibit complete habituation into LRS. The read voltage was 5 V.

Figure 5.15d tracks the dependence of read current on width of the applied 5-pulse train used to stress the device into the different resistance states. HRS can be reliable accessed down below the millisecond range, while LRS down to 0.1 s.

5.3 Conclusion

In summary, an experimental approach to locally creating gate-tunable memristive circuit elements in atomically-thin materials has been successfully demonstrated. The advantages of employing a helium ion beam include high material sensitivity for sputtering, remarkable nanoscale precision and scalability of fabrication. Additionally, the instrument is strongly compatible with established industrial lithographic processes. In contrast to growing polycrystalline films, this method allows for site-specific inclusion of memristive elements in large-area mono-layer circuits, as well as post-metallisation alterations. Stable neuromorphic functionality is demonstrated, advancing the potential of two-dimensional semiconductors for application in future revolutionary nanoelectronics devices.

5.4 References

1. Ge, R. *et al.* Atomristor: Nonvolatile Resistance Switching in Atomic Sheets of Transition Metal Dichalcogenides. *Nano Letters* 18, 434–441 (2018).
2. Wang, M. *et al.* Robust memristors based on layered two- dimensional materials. *Nature Electronics* 1, (2018).
3. Cheng, P., Sun, K. & Hu, Y. H. Memristive Behavior and Ideal Memristor of 1T Phase MoS 2 Nanosheets. *Nano Letters* 16, 572–576 (2016).
4. Bessonov, A. A. *et al.* Layered memristive and memcapacitive switches for printable electronics. *Nature Materials* 14, 199–204 (2015).
5. Li, D. *et al.* MoS_2 Memristors Exhibiting Variable Switching Characteristics toward Biorealistic Synaptic Emulation. *ACS Nano* 12, 9240–9252 (2018).
6. Sangwan, V. K. *et al.* Gate-tunable memristive phenomena mediated by grain boundaries in single-layer MoS_2. *Nature Nanotechnology* 10, 403–406 (2015).
7. Sangwan, V. K. *et al.* Multi-terminal memtransistors from polycrystalline monolayer molybdenum disulfide. *Nature* 554, 500–504 (2018).
8. O'Brien, M. *et al.* Transition Metal Dichalcogenide Growth via Close Proximity Precursor Supply. *Scientific Reports* 4, 7374 (2014).
9. Fox, D. S. *et al.* Nanopatterning and Electrical Tuning of MoS_2 Layers with a Subnanometer Helium Ion Beam. *Nano letters* 15, 5307–13 (2015).
10. Kretschmer, S. *et al.* Supported Two-Dimensional Materials under Ion Irradiation: the Substrate Governs Defect Production. *ACS Applied Materials & Interfaces* acsami.8b08471 (2018). doi:10.1021/acsami.8b08471
11. Lee, C. *et al.* Anomalous Lattice Vibrations of Single- and Few-Layer MoS_2. *ACS Nano* 4, 2695–2700 (2010).
12. Ye, M., Winslow, D., Zhang, D., Pandey, R. & Yap, Y. Recent Advancement on the Optical Properties of Two-Dimensional Molybdenum Disulfide (MoS_2) Thin Films. *Photonics* 2, 288–307 (2015).
13. Kim, I. S. *et al.* Influence of stoichiometry on the optical and electrical properties of chemical vapor deposition derived MoS_2. *ACS Nano* 8, 10551–10558 (2014).
14. Lin, Y. *et al.* Dielectric screening of excitons and trions in single-layer MoS_2. *Nano Letters* 14, 5569–5576 (2014).

15. Nan, H. *et al.* Strong photoluminescence enhancement of MoS_2 through defect engineering and oxygen bonding. *ACS Nano* 8, 5738–5745 (2014).
16. Maguire, P. *et al.* Defect Sizing, Distance and Substrate Effects in Ion-Irradiated Monolayer 2D Materials. (2017).
17. Late, D. J., Liu, B., Matte, H. S. S. R., Dravid, V. P. & Rao, C. N. R. Hysteresis in single-layer MoS 2 field effect transistors. *ACS Nano* 6, 5635–5641 (2012).
18. Kaushik, N. *et al.* Reversible hysteresis inversion in MoS_2 field effect transistors. *npj 2D Materials and Applications* 1, 34 (2017).
19. Chow, P. K. *et al.* Defect-induced photoluminescence in monolayer semiconducting transition metal dichalcogenides. *ACS Nano* 9, 1520–1527 (2015).
20. Splendiani, A. *et al.* Emerging Photoluminescence in Monolayer MoS_2. *Nano Letters* 10, 1271–1275 (2010).
21. Kaupmees, R., Komsa, H. P. & Krustok, J. Photoluminescence Study of B-Trions in MoS_2 Monolayers with High Density of Defects. *Physica Status Solidi (B) Basic Research* 1800384, 3–7 (2018).
22. Komsa, H.-P. & Krasheninnikov, A. V. Native defects in bulk and monolayer MoS 2 from first principles. *Physical Review B* 91, 125304 (2015).
23. Urasaki, S. & Kageshima, H. First-principles study on charged vacancies in MoS_2. *Japanese Journal of Applied Physics* 57, 125202 (2018).
24. Le, D., Rawal, T. B. & Rahman, T. S. Single-layer MoS_2 with sulfur vacancies: structure and catalytic application. *The Journal of Physical Chemistry C* 118, 5346–5351 (2014).
25. Komsa, H.-P., Kurasch, S., Lehtinen, O., Kaiser, U. & Krasheninnikov, A. V. From point to extended defects in two-dimensional MoS_2: evolution of atomic structure under electron irradiation. *Physical Review B* 88, 35301 (2013).
26. Sensoy, M. G., Vinichenko, D., Chen, W., Friend, C. M. & Kaxiras, E. Strain effects on the behavior of isolated and paired sulfur vacancy defects in monolayer MoS 2. *Physical Review B* 95, 14106 (2017).
27. Shang, M.-H. *et al.* Eliminate S-vacancy as the Cause for n-type Behavior of MoS_2 from First-principles Perspective. *Physical Properties of Nanomaterials and Materials J. Phys. Chem. Lett., Just Accepted* (2018).

doi:10.1021/acs.jpclett.8b02591

28. Parkin, W. M. *et al.* Raman Shifts in Electron-Irradiated Monolayer MoS_2. *ACS Nano* 10, 4134–4142 (2016).
29. Liu, H., Neal, A. T. & Ye, P. D. Channel length scaling of MoS_2 MOSFETs. *ACS Nano* 6, 8563–8569 (2012).
30. Yu, S. *et al.* Scaling-up resistive synaptic arrays for neuro-inspired architecture: Challenges and prospect. *Technical Digest - International Electron Devices Meeting, IEDM* 2016-February, 17.3.1-17.3.4 (2015).
31. Cheng, P., Sun, K. & Hu, Y. H. Memristive Behavior and Ideal Memristor of 1T Phase MoS2Nanosheets. *Nano Letters* 16, 572–576 (2016).
32. Kim, M. *et al.* Zero-static power radio-frequency switches based on MoS2 atomristors. *Nature Communications* 9, 2524 (2018).
33. Prezioso, M. *et al.* Training and operation of an integrated neuromorphic network based on metal-oxide memristors. *Nature* 521, 61 (2015).
34. Bessonov, A. a *et al.* Layered memristive and memcapacitive switches for printable electronics. *Nature materials* 14, 199–204 (2015).

Chapter 6

Charge Trapping in Helium Ion Irradiated MoS_2

In this chapter the evolution of the conductivity of MoS_2 devices in-situ is investigated as an accumulating dose of helium ions is delivered to the centre of the channel. A single pixel wide line irradiation (probe size <5 nm) delivers an ion dose of $0.1\ \mathrm{pC\ \mu m^{-1}}$ to $4\ \mathrm{pC\ \mu m^{-1}}$ in 14 discrete steps with two drain-source voltage sweeps performed after each step. The ion irradiation introduces defects to the material which act as charge traps. The density of traps increases approximately linearly with delivered dose before saturating above $2.5\ \mathrm{pC\ \mu m^{-1}}$. At low ion doses the output curve exhibits a 'transient' hysteresis, that is only present in the positive region of the first I-V sweep after irradiation and is not present in the second sweep. Traps introduced by the ion irradiation degrade the conductivity of the device but are filled by injected carriers during the forward bias sweep; thus the return sweep and subsequent forward sweep are higher in current. As the ion dose is increased the hysteresis remains present for both the first and second sweep. As the dose is increased further the I-Vs cross over with the second sweep showing slightly larger hysteresis than the first. At this point the density of traps is no longer increasing with the delivered ion dose, and the additional defects may begin donating carriers to the channel.

6.1 Experimental Procedure

Device Fabrication

Chemical vapour deposition monolayer MoS_2 was prepared via sulfurisation of MoO_3 on marked 285 nm SiO_2/Si chips outlined in reference [1]. Electrodes were defined by electron beam lithography (Zeiss Supra SEM), utilising PMMA A3 resist exposed at a dose of 200 μC cm^{-2} followed by development for 45 seconds in MIBK:IPA (1:3). Metal deposition was carried out in an electron beam-evaporator (Temescal 2000) to deposit Ti/Au (5/35 nm) pads, followed by lift-off in acetone overnight at room temperature.

Ion beam irradiation and in-situ electrical testing

The devices were inserted into the Zeiss Nanofab helium ion microscope fitted with MM3A-EM Kleindiek micro-manipulators. Before contacting the device, a high dose (10^{18} Ne^+ cm^{-2}) beam was used to sputter MoS_2 around the perimeter of the contact pads, to electrically isolate them from the larger MoS_2 film. Two of the micro-manipulators with tungsten probes were brought into contact with the device electrodes before irradiation. Care was taken to avoid irradiation of the channel region while positioning the probes. One of the probes remained grounded throughout the irradiation. The milling pattern was generated using *NanoPatterning and Visualisation Engine (NVPE)* from *FIBICS Inc* and consisted of a single pixel line bisecting and spanning the width of the channel. A 30 keV beam was used at normal incidence with a beam current of ~1 pA and with a 10 μm aperture. The probe size was ~1 nm. The step size was 1 nm. The number of repeats was varied to achieve the desired dose. A Keithley semiconductor parameter analyser was connected to the probes to perform the electrical measurements. Two bipolar current-voltage (I-V) sweeps were performed after each irradiation. In-situ irradiation and testing was performed at HZDR, Dresden, Germany, with assistance from Dr. Gregor Hlawacek.

AFM imaging

AFM was performed in ambient using an *Oxford Asylum* atomic force microscope in tapping mode with 300 kHz cantilevers (Budget Sensors Tap300AL-G).

6.2 Results and discussion

Figure 6.1a shows an optical micrograph of the MoS_2 device. An equilateral triangular-shaped, single-crystal, monolayer flake is top-contacted by two Ti/Au electrodes with a 3 μm channel length. The average width of the channel between the electrodes is 2 μm. The electrodes extend to 50 × 50 μm contact pads, which are sitting on a larger MoS_2 film. As this film may short the contact pads around the intended channel, the pads were isolated from the film by using a high dose (10^{18} Ne^+ cm^{-2}) Ne^+ beam irradiation. A 10 nm wide pattern was traced with the beam around the perimeter of the pads in order to sputter a gap into the MoS_2 film. The sputtered region can be seen in the inset of Figure 6.1a. Ne^+ was chosen over He^+ for its higher sputtering efficiency, and the chosen dose is sufficient to completely remove the MoS_2.[2] The contact pads were contacted with tungsten probes inside the HIM chamber, so electrical testing could be performed in-situ. A schematic of the device and the irradiation strategy is shown in Figure 6.1b. The device was repeatedly irradiated at the same site, with a single pixel line traced by the beam through the centre of the channel, parallel to the electrodes. After each irradiation, two bipolar sweeps were performed between the source and drain electrodes, and the current was measured. To perform a bipolar sweep the voltage is swept from 0 V to 35 V back through 0 V to -35 V and then finally back to 0 V.

Figure 6.1c shows an SEM image of the device after all the irradiations have been performed. The electrodes are false coloured in gold. The darker MoS_2 flake can be seen supported by the brighter SiO_2 substrate. The helium ion irradiated region can be seen clearly in the image as it spans the entire channel and extends out onto the substrate. An AFM height map of the same region was taken and is shown in Figure 6.1d. Here, a line profile of the irradiated region was produced and is shown in the inset. The irradiated region is lower in height than the surrounding non-irradiated MoS_2. This contrasts with build-up of the hydrocarbon beam induced deposition (BID) as seen for the devices in chapter 5. This may be due to the fact that this device was repeatedly irradiated and thus the subsequent irradiations would remove the BID from the earlier ones. However, this would not explain why the BID is still present on the irradiated region of the substrate, as can be seen as the brighter region on the height map. One key difference between the irradiation of this device is that the source electrode remained grounded throughout the

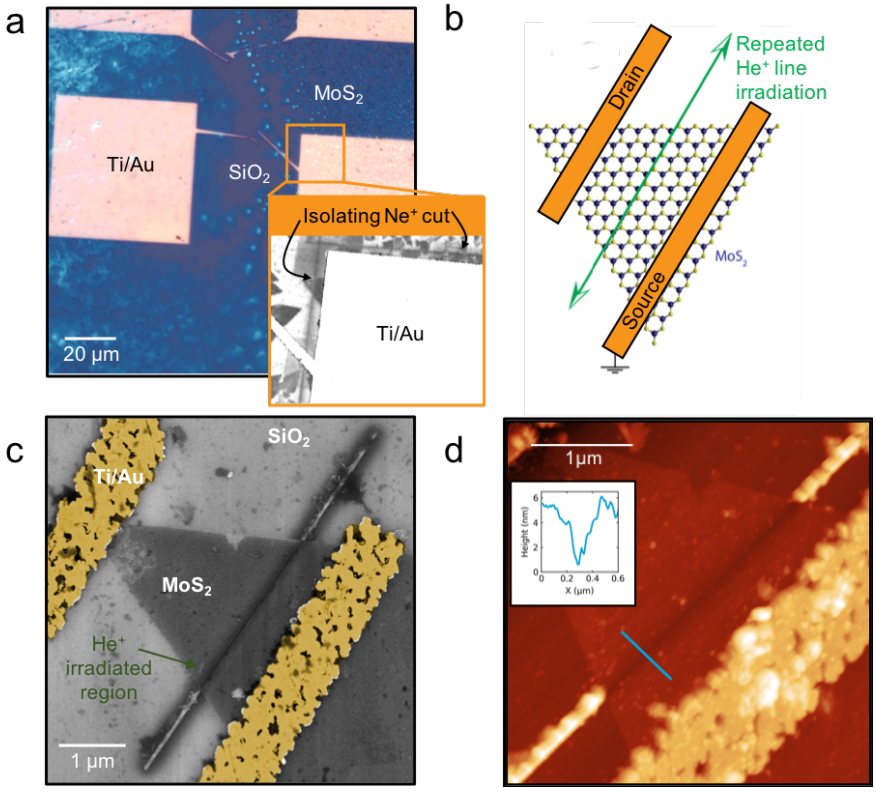

Figure 6.1 | (a) Optical micrograph of MoS_2 flakes and surrounding film on SiO_2 substrate. The Ti/Au contact pads are visible with the electrodes extending to a single crystal monolayer MoS_2 flake. The highlighted region shows an SEM micrograph where the isolating Ne^+ irradiation region can be seen. (b) Schematic diagram of device and beam irradiation strategy. (c) SEM micrograph of irradiated device with false colour electrodes. The helium ion line irradiated region is indicated. (d) AFM image of same region. A line scan over the irradiated region shows an indent of ~5 nm.

entire experiment (as indicated in the schematic in Figure 6.1b). This would allow charge on the flake to dissipate rather than build up during the irradiation, which may affect the adsorption of hydrocarbon contamination prior to polymerisation by the beam. Locally, the substrate region outside the MoS_2 would be more positively charged than the flake region as the beam makes its multiple passes. This would cause hydrocarbon molecules to be attracted away from the flake and towards the substrate resulting in the observed BID pattern. Exploiting localised fields in this way may be a good method of preventing beam-induced contamination of samples in the HIM.

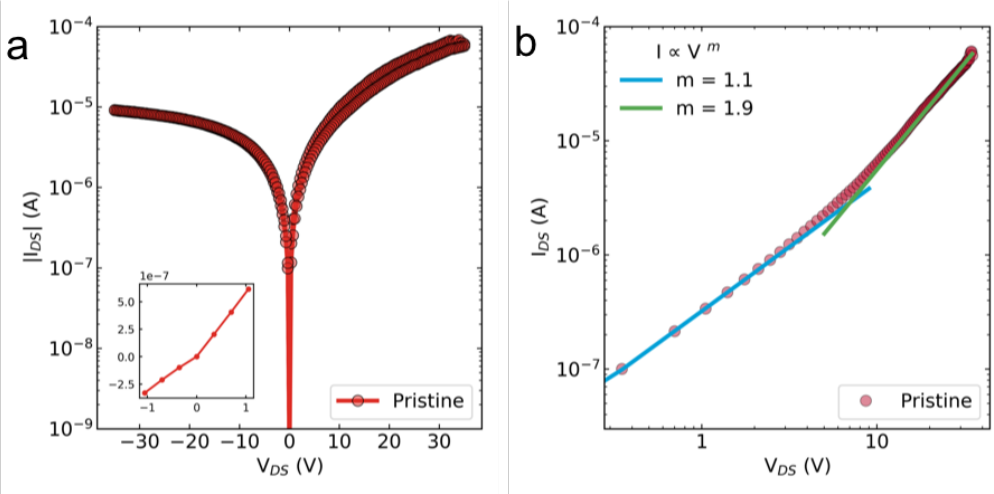

Figure 6.2 | *Electrical performance of the pristine device* (a) Current-voltage characteristic of the pristine device on a semilog scale. (b) Positive I-V trace showing two different conduction regimes. A linear ohmic regime ($I \propto V$, blue line) and the space charge limited current (SCLC) regime ($I \propto V^2$, green line). The symbols are experimental data points while the solid lines represent the fitting.

The electrical characteristics of the device prior to helium ion irradiation are shown in Figure 6.2. Figure 6.2a shows the output curve of the device on a semilog scale and is typical for a monolayer MoS_2 device. The slight asymmetry in the positive and negative polarities of the curve may be caused by a Schottky barrier at the contacts leading to a difference in charge injection at the electrodes.[3] The inset shows the low field portion of the same curve on a linear scale, which appears linear around 0 V. The positive bias region is plotted on a log-log plot in Figure 6.2b showing two different conduction regimes. In the first region at low bias, fitted with the blue line, we see the I-V curve follows an approximately linear dependence, $I \sim V$, which indicates that the conduction is ohmic. We can use the positive polarity region, which is not limited by the rectifying behaviour to investigate the transport further.

In the second region at higher bias, fitted with the green line, the charge transport follows a power law $I \sim V^2$ indicating the initiation of the trap-free space charge limited conduction (SCLC) regime.[4,5] The SCLC occurs when the injected carrier density at high bias exceeds the intrinsic carrier density of the material at that temperature.

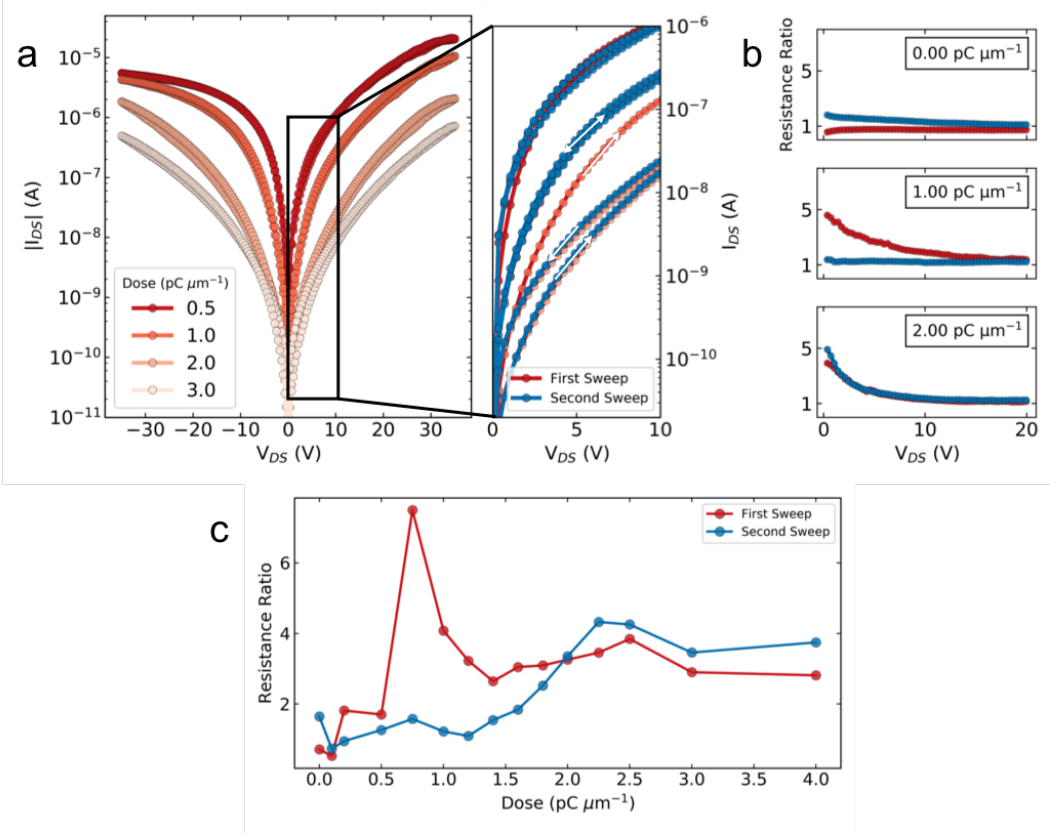

Figure 6.3 | *Electrical performance of He^+ irradiated device* (a) Semi-log plot of I-V sweeps for 4 selected doses. As the dose is increased, the device becomes more resistive, while the I-Vs become more symmetric. Inset: Plot showing the two I-V sweeps taken at three doses shown in the main figure (3.0 pC μm^{-1} excluded for clarity). No hysteresis is seen in either sweep at 0.5 pC μm^{-1}. Hysteresis is present the in first sweep only at 1.0 pC μm^{-1}. Hysteresis is observed, however, in both sweeps at 2 pC μm^{-1} (b) Ratio of the forward and backward trace of both sweeps as a function of drain source voltage. A ratio of 1 indicates no hysteresis while the further the divergence from 1 the larger the hysteresis. (c) Resistance ratio of forward and reverse trace extracted from linear fits near 0 V plotted as a function of dose. Below 0.5 pC μm^{-1} both sweeps show negligible hysteresis. The first sweep ratio increases to a maximum at 0.75 pC μm^{-1} while the second sweep remains around 1. As the dose is increased past 1.5 pC μm^{-1} hysteresis increases for the second sweep, crossing over the first sweep at 2.0 pC/μm and reaching a maximum at 2.25 pC μm^{-1}. All dose values are accumulated ion dose.

In the absence of charge trap states, current flow is described by the Mott-Gurney equation:

$$J = \frac{9}{8}\frac{\mu\varepsilon}{d^3}V^2 \qquad \textbf{6 - 1}$$

where J is current density, μ is the mobility, ε is the dielectric constant and d is the distance between the electrodes. These two conduction regimes fit the data well with fitted scaling exponents of 1.1 and 1.9 for the ohmic and SCLC regions respectively. Visschere et. al.[6] reformulated the Mott-Gurney equation for a two-dimensional in-plane layout, which replaces the $\frac{1}{d^3}$ term by a quadratic dependence on length and is given by:

$$K = \frac{2}{\pi}\frac{\mu\varepsilon}{d^2}V^2 \qquad \textbf{6 - 2}$$

where K is the surface current density in units of A m^{-1}. From this equation and the fitting in Figure 6.2b we can solve for the charge carrier mobility which is μ = 25 cm^{-2} V^{-1} s^{-1}. This is not as high as other reports of back-gated monolayer MoS_2 devices (64 cm^{-2} V^{-1} s^{-1})[7], however it is higher than typically seen for devices in this work, and most likely an overestimation. We can use the ohmic region of the curve to estimate the carrier concentration (n_{2D}) from the equation for conductivity (σ):

$$\sigma = \mu e n_{2D} \qquad \textbf{6 - 3}$$

where e is the elemental charge. The conductivity in the ohmic region is $2.1 \times 10^{-7}\ \Omega^{-1}$ which yields $n_{2D} = 5.3 \times 10^{10}\ cm^{-2}$.

The electrical characteristics of the irradiated device are shown in Figure 6.3a. As the He^+ dose accumulates from 0.5 pC μm^{-1} to 3.0 pC μm^{-1} the output current drops as the resistance of the device is increasing. Additionally, as the dose increases, the rectifying nature of the I-V vanishes, resulting in the positive and negative polarity sweeps becoming symmetric. This would indicate the conduction is now primarily controlled by the irradiated region, which acts as a resistive element in series with the rest of the device. The inset of this figure shows a magnified plot of the low positive bias region. Here both the first (in red) and second (in blue) I-V sweeps taken after each irradiation are plotted. At a dose of 0.5 pC μm^{-1} the two I-V sweeps are well overlaid with one another, with

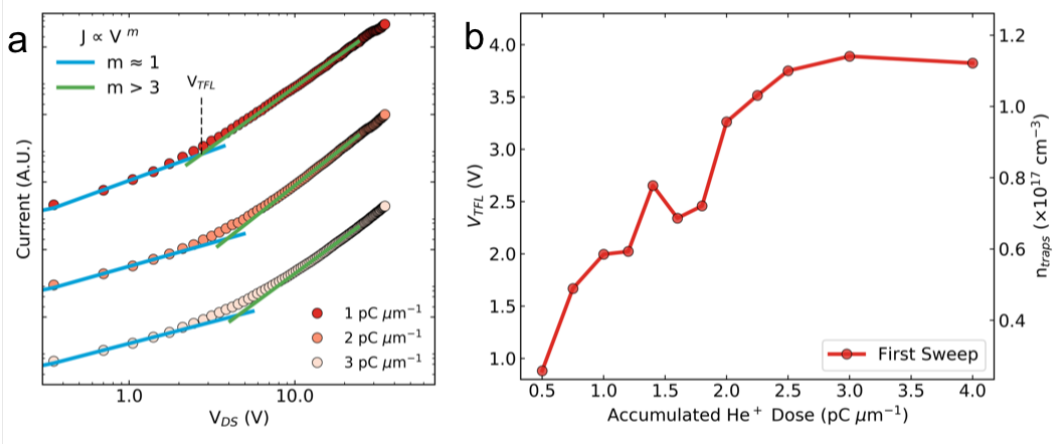

Figure 6.4 | (a) Positive I-V trace of the first sweeps of the irradiated device at three different doses on a double log scale. The curves transition from an ohmic regime (blue fitted curves) to a trap-filled limit (TFL) regime (green fitted curve). The transition voltage between the two regimes is denoted V_{TFL}. The y-axis is rescaled for clarity. (b) V_{TFL} and the corresponding trap density as a function of accumulated ion dose as extracted from the first sweep.

negligible hysteresis. At a dose of 1 pC μm^{-1} the first sweep shows hysteresis, while the second does not. Finally, at a dose of 2 pC μm^{-1} both the first and second sweeps show hysteresis.

We can analyse the size of the hysteresis by taking the ratio of the forward and backward trace for each I-V sweep. A ratio of 1 would indicate that the traces are overlaid on one another while the further the divergence from one, the larger the loop. This ratio is shown for the unirradiated device and at two irradiation doses in Figure 6.3b. The loop is small for both sweeps before the device is irradiated. The loop grows large for the first sweep only at 1 pC μm^{-1} and the loop is large for both sweeps at 2 pC μm^{-1}. A single value for the hysteresis size is produced by making linear fits to the data near 0 V and taking the ratio of the slopes for the forward and backward trace. This ratio value is plotted for both sweeps for each accumulated dose value in Figure 6.3c. Below 0.5 pC μm^{-1} both sweeps show negligible hysteresis.

The first sweep ratio increases to a maximum at 0.75 pC μm^{-1} while the second sweep ratio remains around 1. As the dose is increased past 1.5 pC μm^{-1} hysteresis increases for the second sweep, crossing over the first sweep at 2.0 pC μm^{-1} and reaching a

maximum at 2.25 pC μm^{-1}. The ratio for both sweeps declines slightly as the dose is increased to 4 pC μm^{-1}.

We can analyse the I-V characteristics using the SCLC model to investigate the presence of charge trap states in the device, as has been done for organic thin-film semiconductors[8–10], graphene oxide[11,12] and MoS_2[4]. For a trap-free solid, or when trap states do not dominate the transport, conduction is governed by equation 6 - 1. At high bias the I-V curve follows a power law with exponent 2. In the presence of trap states that are exponentially distributed in energy, the I-V follows a power law with exponent >2. This model fits well to the I-V characteristics of the irradiated device. Figure 6.4a shows a double-log plot of the forward trace of the first I-V trace of the device for three different irradiation doses, 1, 2 and 3 pC μm^{-1}. At all three doses the device exhibits ohmic conduction at low bias, fitted with blue lines, and then transitions to a power law with exponent greater than 3. In this regime, when injected carriers fill all the available trap states, we see a rapid rise in the current. The transition voltage to this trap-filled limit (TFL) is denoted as V_{TFL}. As the density of traps (n_{traps}) increases, the voltage required to reach the TFL increases. The two quantities are linearly related by[8]:

$$V_{TFL} = \frac{en_{traps}d^2}{2\varepsilon} \qquad \textbf{6 - 4}$$

Thus, by fitting to the two bias regimes for all dose values we can extract the V_{TFL} and the associated trap density. This model assumes that charge traps, whether arising in the bulk MoS_2 crystal or at the SiO_2 interface, are distributed along the entire length of the channel. In this case we know the irradiated region is controlling the conductivity of the entire device and that this region spans only a few tens of nanometres. From Figure 6.1c we can see that the dark contrast line is approximately 30 nm wide. Therefore, if we assume the majority of the charge traps arise within a 30 nm region, rather than the whole 3 μm channel, this would result in a 2 order of magnitude rescaling of the trap density. V_{TFL} and n_{traps} are plotted vs. accumulated ion dose in Figure 6.4b. We can see that the trap density extracted from the first sweeps rises as the dose increases from 0.5 pC μm^{-1} to about 2.5 pC μm^{-1} at which point it saturates around a value of 1.1×10^{17} cm^{-3}. We note that this value of the trap density compares well to the trap density of $\sim 1.7 \times 10^{17}$ cm^{-3} extracted by this method by Ghatak et. al.[4]

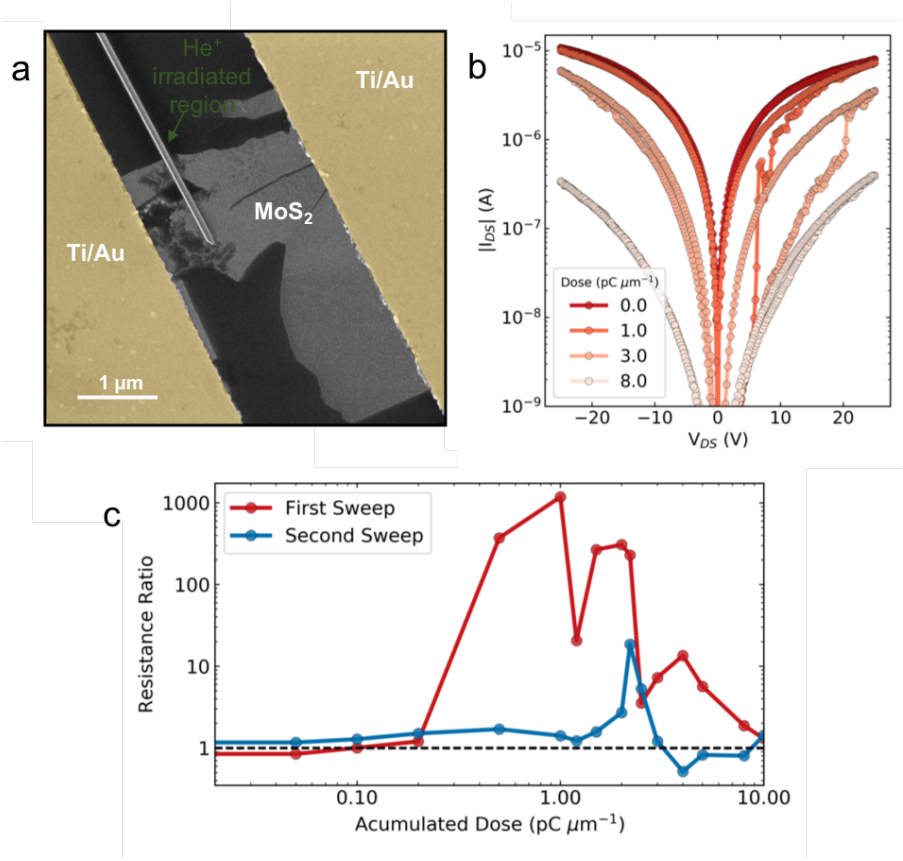

Figure 6.5 | *Transport characteristics of an irradiated 4-layer MoS_2 device.* (a) HIM image of 4-layer device after all line irradiations of the channels. Degradation of the MoS_2 flake can be seen after multiple high bias sweeps were performed. The electrodes are false coloured in gold. (b) I-V sweeps of the device before irradiation and at three irradiation doses. As the dose increases the device becomes more resistive and the I-V become more symmetric. Large hysteresis can be seen in the positive polarity sweeps at 1.0 pC μm^{-1} and 3.0 pC μm^{-1}. (c) Resistance ratio of forward and reverse traces extracted from linear fits near 0 V, plotted as a function of dose. The ratio of the first sweep increases dramatically at a dose of 0.5 pC μm^{-1}, while the second sweep remains around 1. As the dose is increased past 1.5 pC μm^{-1} the ratio of the second sweep increases to a maximum at 2.2 pC μm^{-1}.

To investigate this phenomenon further, the experiment was repeated on a second device. A mechanically exfoliated 4-layer MoS_2 device was fabricated and is shown in the HIM image in Figure 6.5a. This image was taken after all the line irradiations of the channel were completed. The contacts are false coloured in gold. The damage region from the He^+ irradiation can be seen due to its bright contrast and is indicated on the image. The same irradiation and electrical testing procedure was performed. The centre of the channel was

line irradiated by the HIM to deliver a dose of He^+ to the centre of the channel. After each irradiation event two I-V sweeps were performed in-situ, in the HIM chamber. Figure 6.5b shows the first I-V curves of the pristine device and after an accumulating dose of 1.0 pC μm^{-1}, 3.0 pC μm^{-1}, and 8.0 pC μm^{-1}.

As with the monolayer device, prior to irradiation the device shows an asymmetry in the positive and negative polarity sweeps, indicating the presence of a Schottky barrier. As the irradiation accumulates the resistance of the device increases and this asymmetry vanishes. Large hysteresis loops can be seen in the positive I-V sweeps for the intermediate doses. We can track the size of the hysteresis with ion dose in the same manner as was done in Figure 6.3c and this is shown in Figure 6.5c. These two graphs show qualitatively similar features. For the lower ion doses (<0.2 pC μm^{-1}) the hysteresis is negligible for both sweeps. At 0.5 pC μm^{-1} very large hysteresis emerges in the first sweep only, however it has mostly dissipated for the second sweep at that dose, which remains close to 1. The second sweep shows no hysteresis, while the first remains large, until a dose of 1.5 pC μm^{-1}, where it starts to increase.

The HIM has been shown to introduce defects, preferentially sulfur vacancies, into the crystal structure of MoS_2.[2,13] Defects introduced by electron beam irradiation in the active MoS_2 layer and at the dielectric interface have been shown to act as charge trapping sites in MoS_2.[14] Transport mediated by these localised states has been explained by variable range hopping (VRH)[15] or temperature activated behaviour[16]. Trap dominated SCLC has been observed in short channel MoS_2 FETs.[4] Recent theoretical work has shown that S vacancies can act as both p-type and n-type dopants, where higher concentrations of single V_s or clusters of V_s yield n-type characteristics.[17] Charge traps can affect the carrier mobility as the trap states act as localised states that the electrons in the MoS_2 sheet must fill before reaching band-like transport.

As the channel of the device is irradiated by He ions, defects accumulate. These defects cause a reduction in the mobility likely arising from Coulomb scattering.[14] This results in an almost 2 order of magnitude reduction in output current when irradiated by 2.0 pC μm^{-1} compared to the pristine device. The resulting symmetry of the output curve indicates that this irradiated region dominates the transport characteristics of the device rather than the Schottky barrier at the contacts.

The hysteresis in the output curve arises as the density of charge traps increases. Electrons injected during the forward trace of first sweep fill these trap states, which remain filled for the backward trace and the subsequent sweep. Thus, the hysteresis is 'transient', only appearing in the first sweep. As the dose is increased, the density of defects also increases as can be tracked by fitting with the trap filled limited SCLC model. As the dose is increased further (> 2.0 pC μm^{-1}) the density of trap states no longer increases with ion dose. The repeated irradiation of the same region may now result in a high enough concentration of single vacancies or the formation of a cluster of vacancies which begin acting as charge donors rather than acceptors. At this point the hysteresis in the output curve is no longer transient but is present in both sweeps. A higher density of charge traps may result in a shorter detrapping time constant, resulting in unfilled trap states present at the beginning of the second sweeps leading to the observed hysteresis.

6.3 Conclusion

In summary, the evolution of the conductivity of MoS_2 devices repeatedly irradiated with a finely focused helium ion beam was investigated. An accumulating dose of helium ions was delivered to the centre of the channel of the device. The emergence of a 'transient' hysteresis was observed which became permanent above a dose of 2.0 pC μm^{-1}. The irradiation damage can be linked to the introduction of trap states by fitting the I-V data to the trap-filled limit of the SCLC conduction mechanism.

6.4 References

1. O'Brien, M. *et al.* Transition Metal Dichalcogenide Growth via Close Proximity Precursor Supply. *Sci. Rep.* 4, 7374 (2014).
2. Fox, D. S. *et al.* Nanopatterning and Electrical Tuning of MoS_2 Layers with a Subnanometer Helium Ion Beam. *Nano Lett.* 15, 5307–13 (2015).
3. Ghatak, S., Pal, A. N. & Ghosh, A. Nature of electronic states in atomically thin MoS_2 field-effect transistors. *ACS Nano* 5, 7707–7712 (2011).
4. Ghatak, S. & Ghosh, A. Observation of trap-assisted space charge limited conductivity in short channel MoS_2 transistor. *Appl. Phys. Lett.* 103, (2013).
5. Gunasekaran, V. *et al.* Electrical transport properties of two-dimensional MoS_2 nanosheets synthesized by novel method. *Mater. Sci. Semicond. Process.* 66, 81–86 (2017).
6. De Visschere, P., Woestenborghs, W. & Neyts, K. Space-charge limited surface currents between two semi-infinite planar electrodes embedded in a uniform dielectric medium. *Org. Electron. Physics, Mater. Appl.* 16, 212–220 (2015).
7. Li, S.-L., Tsukagoshi, K., Orgiu, E. & Samorì, P. Charge transport and mobility engineering in two-dimensional transition metal chalcogenide semiconductors. *Chem. Soc. Rev.* 45, 118–151 (2016).
8. Shi, D. *et al.* Low trap-state density and long carrier diffusion in organolead trihalide perovskite single crystals. *Science (80-.).* 347, 519–522 (2015).
9. de Boer, R. W. I., Gershenson, M. E., Morpurgo, A. F. & Podzorov, V. Organic single-crystal field-effect transistors. *Phys. Status olidi* 201, 1302–1331 (2004).
10. Kumar, V., Jain, S. C., Kapoor, A. K., Poortmans, J. & Mertens, R. Trap density in conducting organic semiconductors determined from temperature dependence of J−V characteristics. *J. Appl. Phys.* 94, 1283–1285 (2003).
11. Joung, D., Chunder, A., Zhai, L. & Khondaker, S. I. Space charge limited conduction with exponential trap distribution in reduced graphene oxide sheets. *Appl. Phys. Lett.* 97, (2010).
12. Sarkar, A. S. & Pal, S. K. Exponentially distributed trap-controlled space charge limited conduction in graphene oxide films. *J. Phys. D. Appl. Phys.* 48, (2015).
13. Kretschmer, S. *et al.* Supported Two-Dimensional Materials under Ion Irradiation:

the Substrate Governs Defect Production. *ACS Appl. Mater. Interfaces* acsami.8b08471 (2018). doi:10.1021/acsami.8b08471

14. Durand, C., Zhang, X. & Fowlkes, J. Defect-mediated transport and electronic irradiation effect in individual domains of CVD-grown monolayer MoS 2. *J. Vac. Sci. Technol. B* 110, (2015).
15. Qiu, H. *et al.* Hopping transport through defect-induced localized states in molybdenum disulphide. *Nat. Commun.* 4, 1–6 (2013).
16. Radisavljevic, B. & Kis, A. Mobility engineering and a metal-insulator transition in monolayer MoS 2. *Nat. Mater.* 12, 815–820 (2013).
17. Yang, J., Kawai, H., Wong, C. P. Y. & Goh, K. E. J. Electrical Doping Effect of Vacancies on Monolayer MoS_2. *J. Phys. Chem. C* (2019). doi:10.1021/acs.jpcc.8b10496

Chapter 7

Conclusions

In this thesis, a focussed helium ion beam was used to precisely modify the structure of MoS_2 to control its electrical properties. By introducing a population of defects to the centre of the channel of a MoS_2 device memristive switching and synaptic-like behaviour was enabled. Specifically, these devices can be classed as 'memtransistors' in which the switching behaviour could be independently controlled by a third gate electrode, something which is not possible for conventional two-terminal memristor devices. The effect of the beam irradiation on the MoS_2 crystal lattice was investigated using high resolution TEM, with both top-down and cross sectional images of the irradiated region produced. Raman and photoluminescent spectroscopic mapping was used to link the switching of resistance states to the migration sulfur vacancies under applied electric field. The performance of these devices was extensively characterised and retention time of >12 h and endurance of hundreds of cycles was exhibited. The neuromorphic application of these devices, specifically pulsed potentiation and depression and hetero-synaptic plasticity, was demonstrated. This work demonstrated a novel top-down method for fabricating MoS_2 memristors which overcomes the scaling and fabrication compatibility issues faced by as-grown CVD grain boundary memristors.

In order to induce memristive switching in MoS_2, a helium ion dose of 1.6 pC μm^{-1} was required to be delivered to a confined region in the centre of the device channel. The memristive effect was sensitive to the dose delivered, and did not occur for much larger or smaller doses. This is in keeping with previously published results, which showed large changes to the conductivity and transport regime of MoS_2, depending on the helium ion dose, when irradiating the entire channel.[1] Thus, a deeper study of the ion dose sensitivity of this effect was warranted.

A further investigation into the effect of site specific irradiation on the electrical behaviour of MoS_2 was carried out. By conducting electrical measurements of MoS_2

devices in-situ in the HIM chamber, a repeated irradiation study could be performed and the evolution of electrical behaviour tracked. The irradiated device exhibited trap-filled-limit space charge limited conduction and this model could be used to track the charge trap density as a function of ion dose. As the helium ion dose is increased we see that a repeatable hysteresis emerges in the output curve of the device indicating that above a threshold additional defects begin donating charge to the channel and act as mobile charged species. To fully investigated this hypothesis, the capability of gating the device and modifying the carrier concentration is needed. To separate the effects of defects altering both the free carrier density and the mobility by acting as scattering centres. Low temperature measurements would allow you to extract the trap distribution in energy, as well as further study localisation effects by the defects.

7.1 Future Work

The fabrication methodology developed in this work could be expanded to a number of other materials. For example, other 2D TMDCs such as WSe_2 which exhibits p-type doping could compliment the n-type MoS_2 and could be used to form integrated logic and memory circuit architectures. To further investigate the switching mechanism low-temperature transport studies could be employed. The transport behaviour and the contact Schottky barrier heights in the different resistance states could be extracted. This would provide a path for further optimising the device performance. Use of modelling for the ion beam sample interaction would give a better understanding of the population of generated defects, while modelling of the field-driven motion of defects would give insight into the switching mechanism.

7.2 References

1. Fox, D. S. *et al.* Nanopatterning and Electrical Tuning of MoS_2 Layers with a Subnanometer Helium Ion Beam. *Nano letters* **15**, 5307–13 (2015).